



UNIVERSITÄT
OSNABRÜCK

UNIVERSITE
JOSEPH FOURIER
SCIENCES. TECHNOLOGIE. MEDECINE



**Various energy scales in rare earth compounds:
Multiplets, band energy gaps and crystal fields
in RE nickel antimonides.**

Thesis submitted for
obtaining the degree

Doktor der Naturwissenschaften der Universität Osnabrück /
Docteur de l'Université Joseph Fourier, Discipline: Physique

by
Ingo Karla

Defence of the thesis: 5th October 1999 in Grenoble

Jury: Prof. Dr. O. Schirmer
H.Do. Dr. M. Neumann
Prof. Dr. M. Wöhlecke
Prof. Dr. G. Chouteau
Dr. J. Pierre
Dr. P. Haen

The thesis was prepared in the Fachbereich Physik, Universität Osnabrück
and in the Laboratoire de Magnétisme Louis Néel, C.N.R.S. Grenoble, associé
à l'Université Joseph Fourier, Grenoble 1.

Acknowledgements

First of all I would like to thank in particular my supervisors J. Pierre and M. Neumann for that they led me to this interesting new field of physics, the discussions and stimulations during the various stages of this research project.

I would also like to thank J. Szade for growing the GdCu and GdCu₂ samples as well as L. Chioncel for the DOS and band structure calculations.

Further, the assistance from H. Schürmann, B. Ouladdiaf and A. P. Murani is gratefully acknowledged during the synchrotron, elastic neutron diffraction and inelastic neutron scattering experiments respectively.

Furthermore, I am thankful for fruitful discussions with J. Braun, J. Szade, A. Ślebarski, A. Postnikov, K. Kaczmarek, R. V. Skolozdra, J. Toboła, and many others to numerous to mention them. Additionally, I would like thank the jury of my thesis, namely - in addition to my supervisors - O. Schirmer, M. Wöhlecke, G. Chouteau and P. Haen. Finally, I would like to thank all the other people in Osnabrück and Grenoble, who have contributed in some way to the success of this work.

Last but certainly not least, I am grateful for a study grant from the german academic exchange service (DAAD) and from the french government as well as for the financial support through the projects BMBF 05 605 MPB 2 and BMBF 05 SB8MBP 8.

Contents

1	Introduction	7
2	Rare earth compounds	11
2.1	Introduction	11
2.2	Rare-earth theory	14
2.3	Crystal structures	17
2.4	X-ray and neutron diffraction	20
3	Magnetic properties	25
3.1	Introduction	25
3.2	Theory	25
3.3	Experimental	26
3.4	Results	28
3.4.1	Magnetisation and susceptibility	28
3.4.2	Elastic neutron diffraction	33
3.5	Discussion	39
3.6	Conclusion	41
4	Transport properties	43
4.1	Introduction	43
4.2	Theory	44
4.2.1	Metals	44

4.2.2	Semiconductors	45
4.2.3	Magnetoresistance	47
4.3	Experimental	49
4.4	Resistivity in metals	50
4.5	Resistivity in magnetic semiconductors	53
4.5.1	Results	53
4.5.2	Discussion	55
4.6	Giant magnetoresistance	61
4.7	Conclusion	66
5	Crystalline Electric Field	69
5.1	Introduction	69
5.2	Theory	70
5.3	Experimental	73
5.4	Results	75
5.4.1	Heavy rare earth compounds	75
5.4.2	Light rare earth compounds	80
5.5	Discussion	81
5.5.1	Heavy rare earth compounds	81
5.5.2	Light rare earth compounds	85
5.6	Conclusion	91
6	Photoemission	93
6.1	Introduction	93
6.2	Theory	94
6.2.1	Photoemission	94
6.2.2	Resonances	98
6.3	Experimental	100
6.4	Surface preparation	101

6.5	Valence band	103
6.6	Resonances	111
6.6.1	Gd resonance results	111
6.6.2	Gd resonance discussion	114
6.6.3	Tb resonance results	116
6.6.4	Tb resonance discussion	118
6.7	Conclusion	124
7	Conclusion and perspectives	127
	Bibliography	129
	Introduction and conclusion in french	150

Chapter 1

Introduction

Rare earths and their compounds are of high technical interest and many new fields for applications emerge, due to their wide range of unique physical and chemical properties. By taking advantage of the characteristics from all contributing elements and the interactions between them, a rare earth compound can often be designed which possesses exactly the desired properties specially adapted for the intended application, or as a better substitute for existing materials.

This special behaviour arises mainly from the partly filled 4f shell of the rare earth element, which is embedded in the core of the atom with strongly localised moments, while simultaneously their energy states are situated in the (extended) valence band; close to the Fermi level for the light rare earths and some eV below for the heavy rare earth elements. While the ground state multiplet of the 4f subshell may generally be described completely by quantum mechanics and the Russell-Saunders coupling, the situation is very complex for excited configurations due to the highly correlated character of the unbalanced 4f electrons, causing that much of the theoretical description of optical spectra is not yet fully understood, in particular when many body processes are involved. Thus, much work remains to be done to analyse the behaviour of the rare earth atom in interplay with the other elements of the system.

The present thesis is concerned with the characterisation of some rare earth compounds in order to understand further the effects ruling the physical behaviour in these highly correlated systems and the interplay of various energy scales. A special focus is put on the RNiSb series (R = different rare earth elements) as they combine both the properties induced by the rare earth element with a narrow band electronic structure in these hexagonal

or semi-Heusler compounds. This then leads to strongly varying properties especially between the compounds with a light and a heavy rare earth element, ranging e.g. from paramagnets, over ferromagnets to antiferromagnetic structures. The compounds with light rare earth elements are metallic while heavy rare earth compounds are of particular interest as they are magnetic semiconductors where a giant magnetoresistance is discovered.

In order to perform these studies, the group of compounds was investigated from different points of view by employing a wide range of characterisation methods, namely several different magnetic-, transport-, neutron-, as well as photoemission techniques. As will be shown in the body of the thesis, these techniques are complementary in the sense that each of them reveals information on energy levels within a specific energy range, and the results from one technique are often required to analyse the data obtained by another method.

For instance, the magnetic moments of the 4f shell scatter the conduction electrons, thus affecting the electrical resistivity and the magnetoresistance. These transport mechanisms depend on the electronic states around the Fermi level, as well as most physical properties linked to the electronic structure; i.e. the spin distribution of the unpaired electrons explains once again the magnetic moments. The crystalline electric field (CEF) is determined by the bondings in the lattice; it rules many of the observed macroscopic properties (ground state magnetisation, magnetoresistance) which are governed by the population, structure and symmetry of the CEF-levels.

An important aspect of the present work involves the use of theoretical models, which form an essential means of interpreting the experimental data. For each technique employed, the spectra were either simulated or the experimental data were compared and deconvoluted with the values obtained on the theoretical side. The theoretical description allowed then to calculate macroscopic properties, which were also directly measured with another experimental technique. For example, the nature of the resistivity and magnetoresistance mechanisms could be identified by modelling different conduction processes, supported by calculations of the electronic structure. The latter calculations were also necessary to analyse the photoemission and resonance spectra. Simulations of the elastic neutron diffraction and inelastic neutron scattering spectra enabled to determine the magnetic structure and the crystalline electric field scheme, which then in turn allowed to calculate the magnetic resistivity and the susceptibility on this basis.

The general structure of the thesis is as follows: After this general introduction, the opening chapter (2) presents the studied group of rare earth

compounds and their crystal structures as determined by X-ray diffraction. Thereafter, the various magnetic properties are investigated with the help of magnetisation, susceptibility and elastic neutron diffraction measurements (chapter 3). The next chapter (4) is devoted to the electrical transport properties as well as their modification under a magnetic field, followed by the analysis of the CEF determined by inelastic neutron scattering (chapter 5). The electronic structure is then investigated in the following large experimental chapter (6), focused on the states in valence band which is responsible for many physical effects analysed by photoelectron spectroscopy techniques and by resonance experiments. The final chapter (7) contains a summary of the conclusions and possible directions for further work. At the beginning of each chapter, the theoretical background is shortly presented; sometimes necessary results are already given there to which is then referred back later during the analysis.

Chapter 2

Rare earth compounds

2.1 Introduction

The group of rare earths (RE or R) comprises 17 metallic elements, scandium, yttrium, lanthanum and the elements of the extended sixth row of the periodic table, cerium to lutetium; the latter alone are referred to as lanthanides [1]. After the discovery of the first rare earth element, yttrium, in 1794 by Lt. C. A. Arrhenius in a rare swedish ore, the other elements were all found in the following 110 years. However, these elements generally occur all together in nature because of their similar chemical properties which proved them to be very difficult to isolate and to obtain RE elements in the pure form. Therefore, a lot of research had been devoted to solid solutions between different RE elements, before, after the invention of ion exchange resins in the 1950's, the elements became commercially available at a reasonable purity.

The great interest in rare earths and their compounds is motivated by the large amount of unique properties, which are already technically employed and open the scope for further future applications, some of these are stated below. Materials out of this group of RE compounds are applied as excellent strong permanent magnetic materials (e.g. NdFeB, RCo_5 [2]), magnetostrictive devices (e.g. RFe_2 [3]), magneto-optics (e.g. RFeCo) and are used in metal hydride (Ni-MH) batteries [4]. Many intermetallic rare earth compounds can absorb large amounts of hydrogen which has among others invoked a large interest in search for compact, light and safe hydrogen storage tanks applied in electric vehicles and automobiles in combination with fuel cells. Rare earth compounds have gained a large impact on the the field of chemical sensors due to their high sensing characteristics [5] being

applied for example to control emission from power plants in order to reduce air pollution. The richness of possible excited rare earths states make these materials a good source for laser materials and fluorescent screens - such as television screens and intense sources of light [6]. From the theoretical point of view, the analysis of rare earth compounds offers a unique possibility to study theoretical models in which spin and orbital moments occur as a parameter, as within the rare earth series the physical properties vary strongly while influencing little the chemical surrounding. Thus, it is often possible to design a material which possesses almost any property one desires, which then leads to new or optimized applications or which could be used to find substitutes for scarce materials. For these reasons, rare earth compounds are of high technical interest having provoked an intensive, still ongoing, research for understanding the properties and mechanisms in these complex compounds, in order to open a perspective for optimized and new materials for future applications and devices.

This has promoted a considerably large amount of research in this field [7], since the properties of the rare earth elements are quite unique in the periodic table. In contrast to the other metals, the internal core like 4f shell is successively filled in this group, provoking strong localised magnetic moments, different coupling mechanisms and strong correlation effects as will be outlined in the following section 2.2.

RE compounds were studied extensively; those formed between RE and 3d transition metals are of particular interest, because one can benefit simultaneously from the high magnetic moment per atom and the strong single-ion magnetocrystalline anisotropy of the RE partner and as well as from the high magnetic coupling strength of the moments of the 3d transition metal partner. A large amount of research has been done on this group of compounds, reviewed for example in [8, 9, 10, 11, 12]; i.e. RM and RM_x compounds, like for example GdCu and GdCu₂, e.g. [13, 14, 15, 16, 17, 18], which were studied extensively in the 1970's and early 1980's, characterizing almost completely their bulk properties.

In the following years, a lot of research has been shifted to ternary rare earth compounds, which can show more specialised properties which may be exploited for possible applications and for studying the physical processes involved. Compounds between some rare earths, transition metals and metalloids were particularly studied, for fundamental purposes (1:2:2 compounds like supraconducting CeCu₂Si₂) [19] as well as for applications (Nd₂Fe₁₄B) [20]. Especially interesting became the group of Heusler alloys X_2YZ the prototype of which is Cu₂MnAl [21]. These compounds are well known for

transition 3d metals and also exist with rare earths, for instance RCu_2In , RPd_2Sn [22, 23, 24]. Although still showing band magnetism, their magnetic moments are more localised due to the larger distances between magnetic atoms than in the corresponding pure metals, allowing a closer investigation of the magnetic properties. For example, it led to the striking observation, that when the three "non-magnetic" metals are combined, e.g. Cu, Al and Mn, the formed Heusler compound is in turn ferromagnetic. All these pure Heusler phases are metallic with a strong density of states at the Fermi level.

Contrarily, in semi Heusler compounds, XYZ, a vacant site in the crystal structure leads to larger distances between neighbouring X atoms ($d_{X-X} \approx 4.2\text{\AA}$) instead of ($d_{X-X} \approx 3.0\text{\AA}$) in Heusler phases (X_2YZ), resulting in a weaker overlap between the X-transition metal wave functions, giving rise to narrower bands and the appearance of gaps in the density of states (DOS) [25]. This remarkable feature gives rise to a large variety of electronic and magnetic properties [26, 27], which seems to be strongly dependent on the number of valence electrons (EC) [28]. When the number is equal to 18 (e.g. TiNiSn , TiCoSb , ZrNiSn), these phases are often narrow gap semiconductors, while the compounds with more (e.g. EC=19: CoVSb , NiTiSb) or less (e.g. EC=17: FeTiSb , CoTiSn) valence electrons are metallic. The semi Heusler structure became famous after the discovery of so-called 'half metallic character' in MnNiSb and MnPtSb [29, 30, 31, 32, 33, 34].

RNiSb compounds are of particular interest, as they combine both the effects arising from the narrow band structure with the special properties of the rare earth atom. Apart from a first report of the existence of the crystallographic structure in 1983 [35], these compounds became investigated very recently during the last five years. First studies were devoted to the Ce and Yb compounds in search for a Kondo-like or intermediate-valence behaviour; CeNiSb was proposed to be a ferromagnetic Kondo lattice [36, 37, 38]; Yb-NiSb orders antiferromagnetically below 0.8 K [39, 40]. The paramagnetic susceptibilities of other compounds were then investigated by Hartjes and Jeitschko [41], Skolozdra et al. [42] reported antiferromagnetic ordering from Gd to Dy compounds. Very recently, the series of RNiSb compounds was studied in detail by the means of several different characterisation methods [26, 43, 44, 45, 46] the results of which are also found in the present work. Furthermore, many similar isoelectronic compounds have been investigated recently and have shown interesting magnetic and physical properties like for example the RPdSb series [47, 48, 49, 50, 51], RRhSb [52, 53] and RPtSb [54].

2.2 Rare-earth theory

The theory of rare earths and their compounds comprises a large field, extensively presented in many review articles, e.g [7, 11, 55]. Therefore, this section summarizes only some basic information, which is directly linked to the interpretation and analysis of the results in present work.

The group of rare earths is characterized by the successive filling of the internal 4f shell from 0 (La) to 14 (Lu) electrons, which is physically shielded by the 5d-6s conduction band electrons. They all comprise, in their neutral ground state configuration, the closed shell electronic structure of the noble gas xenon $1s^1 2s^2 3s^2 3p^6 3d^{10} 4s^2 4p^6 4d^{10} 5s^2 5p^6$ and two or three external electrons ($6s^2$ or $5d 6s^2$) in addition to the group of $4f^N$ electrons as given in table 2.1.

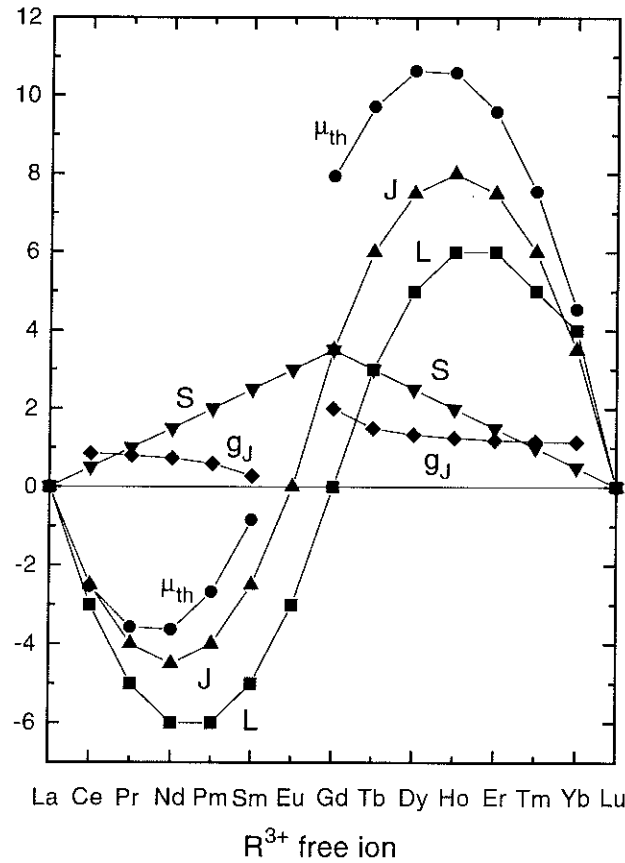


Figure 2.1: Theoretical construction of the L, S, L, g_J and $\mu_{th} = g_J \sqrt{J(J+1)}$ values for the free lanthanide trivalent ions.

The magnetic properties of the rare earths are determined by their ground state configuration, since the first excited multiplet is sufficiently separated in energy. In the crystalline state, the electric field removes then the $(2J+1)$ fold degeneracy of the ground state multiplet (see section 5.2), but the crystal field splitting is generally much smaller than the spin orbit coupling energies. Within the ground state configuration of one rare earth atom, the magnetically important 4f electrons couple together according to the Russell-Saunders coupling and Hund's rules giving angular (L), spin (S) and total momenta (J) as drawn in figure 2.1. Considering the small spatial extent and the highly localised character of the 4f wave functions which have very little overlap with neighbouring atoms, there is essentially no direct exchange as being present in 3d transition metals. Consequently, the magnetic interaction mechanisms has to proceed by an indirect exchange; the coupling takes place via the polarisation of the conduction electrons, which is generally referred to as the Ruderman Kittel Kasuya Yosida (RKKY) theory [56, 57, 58].

Due to the interplay between crystal field, magnetoelastic, direct and indirect exchange interactions, the magnetic structures of rare earth metals and their compounds are particularly complicated. Their angular, spin and total moments vary in a wide range, shown in figure 2.1, giving rise to a rich variety of many different magnetic and physical properties. As they are little influenced by the chemical surrounding, the analysis of rare earth compounds also offers a unique possibility to study theoretical models in which spin and orbital moments occur as a parameter making this class of compounds an ideal model system for theoreticians.

Rare earth compounds are highly correlated systems with unbalanced 4f electrons, where the electron spins and magnetic moments, in particular those of the 4f ones, are strongly coupled and are causing large interaction effects. Thus, optical spectra, e.g. photoemission ones, are rather complex with a large number of lines, and complicated multiplet structures are formed. In these highly correlated materials, it is no longer possible to reduce the problem to an one body approximation and many body effects should be considered, which makes the analysis of these complex spectra more interesting and challenging. Strong resonance effects occur in the rare earths and their compounds, especially when involving the 4d and 4f electronic shell, as the radial extent of those wave functions is comparable (see figure 2.2), leading to strong overlap and coupling between the 4d and 4f states. More details will be given later in chapter 6.2.2.

The stability of an atomic arrangement at the microscopic scale depends on many factors, such as geometric, electronic and energetic restrictions as

Element		electron configuration	ground state multiplet	g_J	μ_{max} [μ_B]	μ_{eff} [μ_B]
Lanthanum	La	$4f^0 (5d 6s)^3$	1S_0		0	0
Cerium	Ce	$4f^1 (5d 6s)^3$	$^2F_{5/2}$	6/7	2.14	2.54
Praseodymium	Pr	$4f^2 (5d 6s)^3$	3H_4	4/5	3.20	3.58
Neodymium	Nd	$4f^3 (5d 6s)^3$	$^4I_{9/2}$	8/11	3.27	3.62
Promethium	Pm	$4f^4 (5d 6s)^3$	5I_4	3/5	2.40	2.68
Samarium	Sm	$4f^5 (5d 6s)^3$	$^6H_{5/2}$	2/7	0.71	0.85
Europium	Eu	$4f^7 (5d 6s)^2$	7F_0		0	0
Gadolinium	Gd	$4f^7 (5d 6s)^3$	$^8S_{7/2}$	2	7.00	7.94
Terbium	Tb	$4f^8 (5d 6s)^3$	7F_6	3/2	9.00	9.72
Dysprosium	Dy	$4f^9 (5d 6s)^3$	$^6H_{15/2}$	4/3	10.00	10.65
Holmium	Ho	$4f^{10} (5d 6s)^3$	5I_8	5/4	10.00	10.61
Erbium	Er	$4f^{11} (5d 6s)^3$	$^4I_{15/2}$	6/5	9.00	9.58
Thulium	Th	$4f^{12} (5d 6s)^3$	3H_6	7/6	7.00	7.56
Ytterbium	Yb	$4f^{14} (5d 6s)^2$	$^2F_{7/2}$	8/7	4.00	4.53
Lutetium	Lu	$4f^{14} (5d 6s)^3$	1S_0		0	0

Table 2.1: Principal properties of rare earths ground state multiplets. g_J is the Landé factor (eq. 3.2), μ_{eff} gives the free ion (paramagnetic) magnetisation (eq. 3.5) and μ_{max} describes the maximal magnetisation in the ordered phase (e.g. ferromagnetic). La and Lu are non magnetic due to their empty and completely filled 4f shell.

well as on the type of chemical bonding, resulting in the formation of a large variety of different crystal structures within the group of rare earth compounds. As a general rule, close packed crystal structures are often favoured when forming a compound between a rare earth and a transition metal. The crystal structures relevant for the present work are presented in the next paragraph. Due to the sensitivity of the stabilising factors, small variations in the parameters are often sufficient to invoke a martensitic type phase transformation of the crystal structure. It occurs quite frequently within a rare earth series of a particular compound, often in the middle of the series, at Gd, related to the turning point of some properties. Many of CsCl type rare earth intermetallic compounds RM (M = nonmagnetic metal) undergo a cubic - tetragonal structural phase transition in dependence of temperature or pressure, which has been considered to arise from the band Jahn-Teller effect, by which d bands in the 5d6s bands of rare earth are split

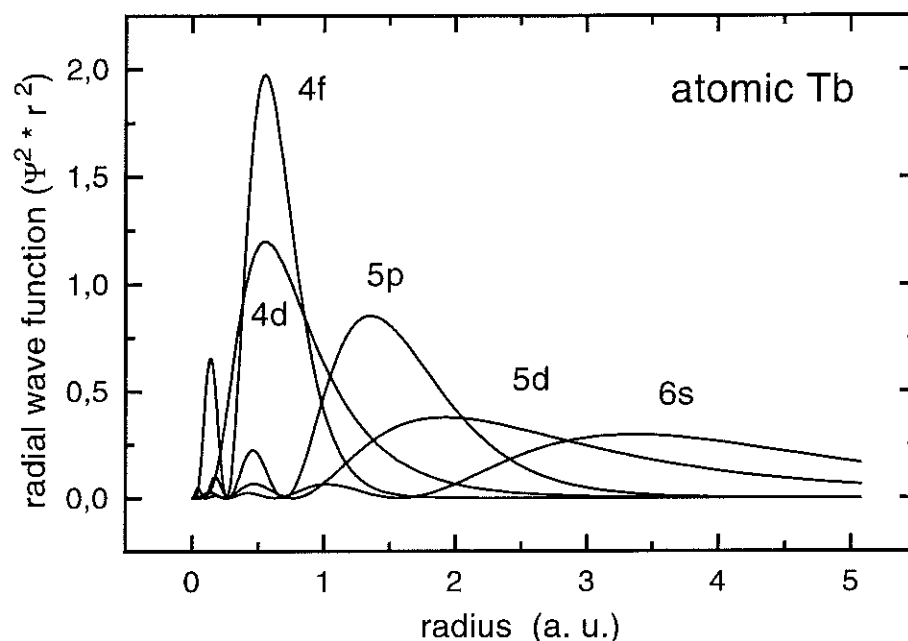


Figure 2.2: Radial distribution (in atomic units, a. u.) of the different electronic shells in atomic Tb [59]. The wave functions were calculated with a relativistic self consistent field program using the code from Liberman [60].

so as to gain in band energy [61]. In particular, within the RCu series a transition occurs from the orthorhombic FeB crystal structure ($R = \text{Ce}, \dots, \text{Gd}$) to the cubic CsCl type one ($R = \text{Gd}, \dots, \text{Lu}$). At room temperature, GdCu is stable in both crystal structures, with a very low activation energy for the transition between these two phases [63], [64]. For this reason, any slight disturbance is sufficient to provoke a transformation on a microscopic scale preventing any long range order to remain stable at the surface.

2.3 Crystal structures

The series of RNiSb compounds ($R = \text{Y}, \text{La}, \text{Ce}, \text{Pr}, \text{Nd}, \text{Gd}, \text{Tb}, \text{Dy}, \text{Ho}, \text{Er}, \text{Yb}, \text{Lu}$) was prepared at the Laboratoire de Magnétisme Louis Néel by induction melting of the pure elements in a cold copper crucible under an argon atmosphere (figure 2.4), melting first the two metals and afterwards adding the antimony. About 2% of extra amount of antimony was added in order to compensate for the losses by evaporation caused by the high vapour

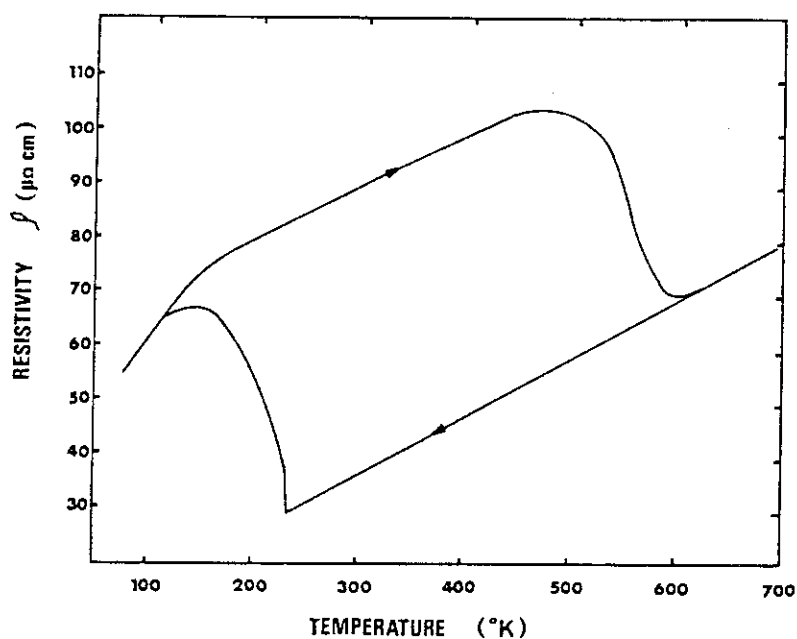


Figure 2.3: Electrical resistivity versus temperature for GdCu [62]. The arrows on the resistivity curve denote the measuring direction. The FeB phase (top curve) and the CsCl phase (bottom curve) are both stable at room temperature.

pressure of Sb [65]. The samples were weighted at each stage of the melting processes assuming the small loss of substance to be caused by antimony evaporation. Afterwards, the as-cast compounds were annealed at 700 °C under vacuum for at least 4 days. X-ray powder diffraction was then used to verify and analyse the crystal structures as will be described in paragraph 2.4.

Due to the strong evaporation of Sb, all attempts failed to grow a RNiSb single crystal by the Czochralski method, as the latter technique requires to maintain the hot phase for a long time while slowly pulling the tungsten needle with the crystalline seed. As a second method, the Bridgman technique [66] was tried without success, because antimony strongly attacked the employed tantalum crucible. The affinity of the RE element to oxygen prevented the use of standard alumina (Al_2O_3) and the choice of elements for the crucibles was further limited as Ni is quite close to many metals, which might easily lead to an alloy of the crucible element with the sample.

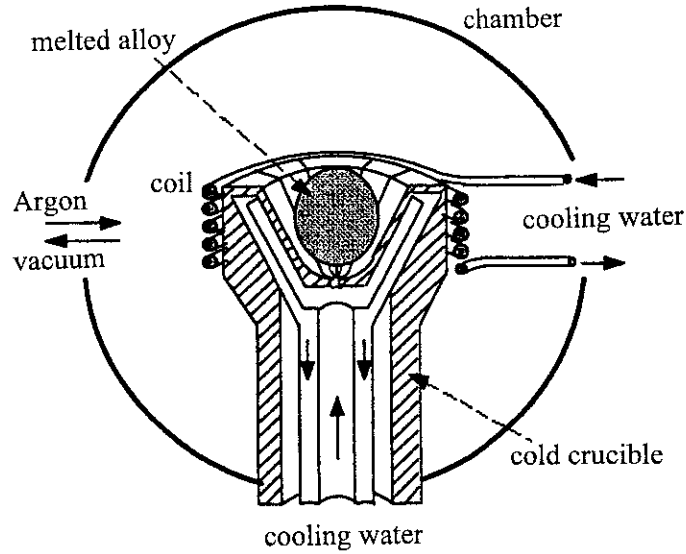


Figure 2.4: Sketch of the cold crucible at the Laboratoire de Magnétisme Louis Néel in Grenoble [27]

The RNiSb compounds formed with a light rare earth element crystallize in the hexagonal ZrBeSi structure (SG: $P6_3/mmc$, No. 194) with an ordered c -axis, which is a superstructure of the disordered AlB_2 cell, whereas the ones with a heavy rare earth element crystallize in the face-centered cubic MgAgAs structure (SG: $F\bar{4}3m$, No. 216) (figure 2.5). GdNiSb occurs in two allotropic forms. These cubic ternary compounds belong to the family of semi-Heusler phases with formula XYZ , where X and Y are a transition or rare earth metal and Z is one sp element, most frequently Sn or Sb . This face-centred lattice structure is deduced from the true Heusler phases X_2YZ by removing one out of two X atoms, leaving a vacant site. This vacant site leads to less overlap between the wave functions, thus to narrower bands, and promotes the formation of gaps in the density-of-states spectrum. These narrow gaps are actually observed in the cubic RNiSb compounds (see figures 4.9, 6.10 and 6.11) and are responsible for many physical effects discussed later. In another way, the structure may be described by starting with a cubic RSb phase (NaCl -type) by inserting one Ni atom in one over two of the tetrahedral voids [67]. The compounds are stabilised through covalent bondings after transferring s electrons from the R and Ni metals to the Z element, favouring the sp^3 hybridisation around Sb [25]. Except for CeNiSb , where configuration interactions may be significant, the RE configuration is

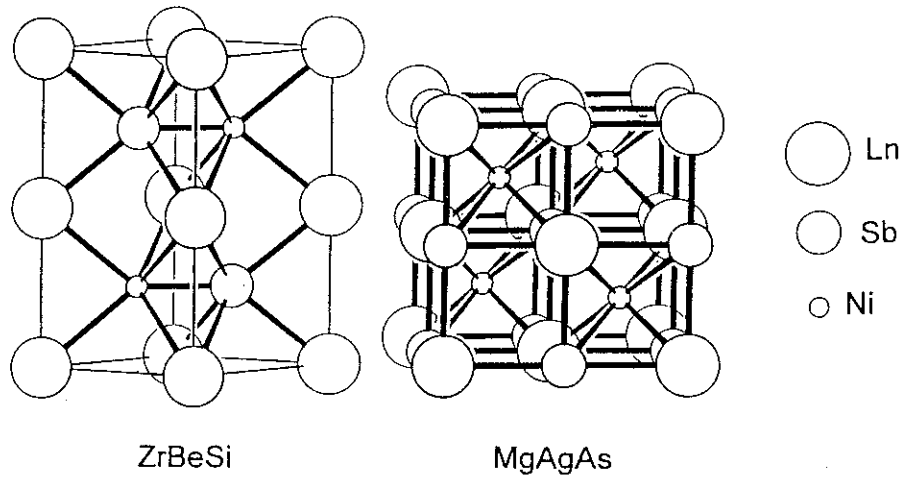


Figure 2.5: Crystal structures of the $RNiSb$ compounds. The ones with a light rare earth element crystallize in the hexagonal $ZrBeSi$ structure (SG: $P6_3/mmc$), which is a superstructure of the AlB_2 cell. The heavy rare earth compounds form the face-centered centered cubic $MgAgAs$ structure (SG: $F43m$). The figure is taken from [41]

trivalent, in agreement with the magnetic properties, and it leads to a total number of 18 valence electrons, which is the most stable configuration in these compounds [25].

The (semi-) single crystals $GdCu$ and $GdCu_2$, which are comparatively easy to grow (in comparison to the other employed compounds of the present work), were obtained in Katowice by a Czochralski method. At room temperature, $GdCu$ is stable in the cubic $CsCl$ (SG: $Pm\bar{3}m$, no. 211, $a=3.502\text{\AA}$) and in the orthorhombic FeB phase (SG: $Pnma$, no. 62) of which the high temperature phase ($CsCl$) should dominate in the bulk since the sample has been cooled down from the melt. $GdCu_2$ crystallises in an orthorhombic structure (SG: $Imma$, no. 74) with the lattice parameters $a = 4.320(5)\text{\AA}$, $b = 6.858(5)\text{\AA}$ and $c = 7.330(5)\text{\AA}$ [68].

2.4 X-ray and neutron diffraction

Powder diffraction is a well established technique to analyse crystalline solid materials, reviewed e.g. in [69, 70, 71]. It allows to characterize the ex-

act structural arrangement and the microstructure (lattice microstrain and domain size) of any crystalline material. The diffraction pattern is like a fingerprint in the sense that no two compounds give rise to exactly identical diagrams, thus being an effective method of phase identification. Furthermore, this technique is quite straightforward and does not require single crystals, which are often not available or difficult to grow.

All diffraction experiments are based on Bragg's law, which writes in the angle dispersive (or constant wavelength) mode as

$$\lambda_0 = 2d_q \sin \theta_q \quad (2.1)$$

where λ_0 describes the wavelength of the incident monochromatic X-ray or neutron beam, θ_q the diffraction angle and d_q is the spacing of the crystal planes specified by the Miller indices $q = (hkl)$. In the case of neutrons, the wave-particle duality equation of de Broglie $\lambda = \frac{h}{mv}$ is employed to relate the neutron velocity to their wavelength.

The intensity of a specific diffraction line $q = (hkl)$ is given by the expression:

$$I_q = \left(\frac{I_0 \lambda^3 l_s}{8\pi r} \right) K_R K_G \frac{j_q}{V_c^2} L_p |F_{hkl}|^2 \quad (2.2)$$

where I_0 describes the intensity of the incident beam; λ is the wavelength of the radiation source; l_s specifies the height of the detector slit; r gives the sample to detector distance, K_R and K_G are constants for a given sample and set of experimental conditions; j_q describes the multiplicity for the reflection q and V_c measures the volume of the unit cell. The factor L_p combines the Lorentz and polarisation factors for the diffractometer geometry; in the case of a non polarized monochromatic beam it is equal to: $L_p = (1 + \cos^2 2\theta_q)/(\sin^2 \theta_q \cos \theta_q)$; for neutrons it reduces to the Lorentz factor $L_p = 1/(\sin 2\theta \sin \theta)$

F_{hkl} is the structure factor for the reflection (hkl) which relates to the intensity of the atomic arrangement in the unit cell according to

$$F_{hkl} = \sum_{j=1}^{\text{unit-cell}} f_j e^{\left(-B_j \frac{\sin^2 \theta_{hkl}}{\lambda^2}\right)} e^{(2\pi i \vec{q} \cdot \vec{x}_j)} \quad (2.3)$$

where x_j are the fractional coordinates of the atom j in the cell and B_j gives the Debye-Waller displacement factor for an atom (in Å). For X-rays, f_j is the atomic scattering factor for the atom j . In the neutron case, f_j is the coherent scattering length which depends on the isotope but does not vary with the scattering angle.

The neutron is composed of one up and two down quarks with charges of $\frac{2}{3}$ and $-\frac{1}{3}$. Although the total charge of the neutrons is zero, the internal structure leads to an electric charge distribution, which in turn causes a magnetic moment, a spin and an electric polarizability of the neutron. Thus, a scattered neutron interacts with the nucleus as well as with the magnetic distribution of the electronic cloud and the cross sections for the neutron-nuclear and neutron-electron interaction are of the same order of magnitude. Therefore, neutron diffraction is a powerful technique to analyse the magnetic structure of magnetic crystals and to determine directly the distribution, direction and magnitude of the magnetic moments. The diffraction theory for neutrons is similar to X-ray diffraction, except for the vector character of the magnetisation. In the expression of the intensity I_q (equation 2.2) an additional term $\langle q^2 \rangle$ expresses the angle between the scattering vector \vec{k} and the moment $\vec{\mu}$. Inelastic neutron diffraction will be treated in chapter 5.2 devoted to the crystalline electric field.

The experimental powder diffraction pattern can then be analysed by peak search, and whole pattern fitting in order to determine the crystal structure. Provided that some information about the structure is approximately known, the Rietveld refinement technique is a very powerful procedure to analyse in detail the structure of the sample. The Rietveld algorithm fits the observed diffraction pattern using as variables the structural parameters of the sample material (cell constants, atomic and displacement parameters) and the instrumental characteristics (resolution curve of the diffractometer).

X-ray powder diffraction measurements were undertaken using Cu K_α radiation ($\lambda = 1.54178 \text{ \AA}$) on all RNiSb samples followed by a simulation and refinement procedure, as shown for example for DyNiSb in figure 2.6. The structural purity without any parasite phases has been confirmed and the crystallographic data were determined, summarized in table 2.2 together with the data deduced from neutron diffraction experiments in section 3.4.2. Only (odd,odd,odd) or (even,even,even) reflections are present, in line with the cubic MgAgAs structure formed by interpenetrating fcc lattices. The lattice parameters vary smoothly with the atomic number showing the well known Lanthanide contraction within this element series caused by the increasing proton charge and influenced by various screening effects. Due to the thermal expansion between helium and room temperature, the measured values are smaller for the neutron than for the X-ray diffraction, and the parameters found agree with earlier data [41]. The presence the ZrBeSi-type phase in the light rare earth compounds is confirmed by the presence of the (011) and (013) superstructure reflections caused by the doubling of the c parameter (figure 3.7) thus ruling out the disordered AlB₂ phase which was

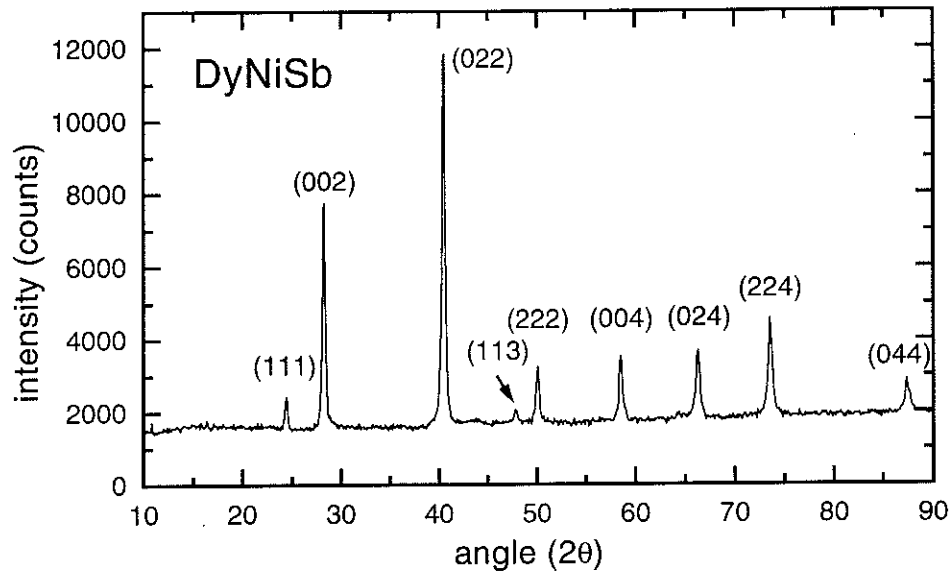


Figure 2.6: X-ray powder diffraction pattern of DyNiSb

first assumed [35].

As the Y atom has a similar size as Tb, Dy or Ho together with a corresponding outer electron configuration, Y compounds possess often very similar physical properties as the corresponding Tb-, Dy-, Ho-, compounds, and it can be anticipated that these compounds have a similar electronic band structure.

The diffraction patterns are principally similar between the X-ray and the neutron diffraction measurements, taken in the paramagnetic temperature range; below the magnetic ordering temperature, additional magnetic peaks grow in the neutron diffraction pattern allowing to obtain further information about the magnetic structure. Since the neutron intensities are more accurate than those obtained by X-rays, the diffraction spectra will be discussed in detail in the neutron diffraction chapter 3.4.2.

Compound	lattice parameter X-rays (300 K)		lattice parameter neutrons (10 K)		structure type	space group
	a (Å)	c (Å)	a (Å)	c (Å)		
YNiSb	6.247(2)				MgAgAs	$F\bar{4}3m$
LaNiSb	4.42(1)	8.39(2)			ZrBeSi	$P6_3/mmc$
CeNiSb	4.395(1)	8.258(4)	4.376(3)	8.192(3)	ZrBeSi	$P6_3/mmc$
PrNiSb	4.34(8)	8.11(8)			ZrBeSi	$P6_3/mmc$
NdNiSb	4.380(5)	7.98(2)	4.364(2)	7.951(3)	ZrBeSi	$P6_3/mmc$
GdNiSb	4.3(8)	7(1)			ZrBeSi	$P6_3/mmc$
GdNiSb	6.263(2)				MgAgAs	$F\bar{4}3m$
TbNiSb	6.332(1)		6.280(3)		MgAgAs	$F\bar{4}3m$
DyNiSb	6.305(1)		6.280(4)		MgAgAs	$F\bar{4}3m$
HoNiSb	6.285(1)		6.246(3)		MgAgAs	$F\bar{4}3m$
ErNiSb	6.263(2)				MgAgAs	$F\bar{4}3m$
YbNiSb	6.2263(8)				MgAgAs	$F\bar{4}3m$
LuNiSb	6.2065(5)				MgAgAs	$F\bar{4}3m$

Table 2.2: Lattice constants of the hexagonal and cubic RNiSb compounds as deduced from X-ray powder diffraction and elastic neutron diffraction. The numbers in parentheses indicate the standard deviations in the place values of the last listed positions.

Chapter 3

Magnetic properties

3.1 Introduction

The magnetic properties have always been in the focus of research of rare earths and their compounds, motivated by the unique properties arising from the strong magnetic moments of the internal 4f shell. Further, they influence several other physical properties through the various coupling mechanisms. A large amount of reviews has been devoted to the theoretical and experimental aspects of magnetism in RE compounds, [10, 72, 73, 74] and the magnetic properties of many related ternary rare earth compounds were investigated with the means of magnetisation, susceptibility measurements [39, 75, 76] as well as with neutron diffraction [54, 77, 78].

As the theoretical aspects of magnetism are well established [74, 79, 80] the following section recalls only shortly those aspects and equations to which is referred while analysing and interpreting the experimental data. Some further information can be found in the chapters about rare earth compounds 2.2 and neutron diffraction/scattering sections 2.4 and 5.2.

3.2 Theory

In the paramagnetic state, the magnetic moment μ of an atom or free ion is given by

$$\vec{\mu} = -g_J \mu_B \vec{J} \quad (3.1)$$

where $\vec{J} = \vec{S} + \vec{L}$ is the total angular momentum, $\mu_B = \frac{e\hbar}{2m}$ the Bohr magneton and the gyromagnetic factor g_J is specified for a free atom by the Landé

equation

$$g_J = 1 + \frac{J(J+1) + S(S+1) - L(L+1)}{2J(J+1)} . \quad (3.2)$$

In a magnetic field (or more exactly magnetic induction) $B = \mu_0 H$, a free atom with a total angular momentum J has $2J + 1$ equally spaced energy levels, leading to a magnetisation $M(B, T)$, dependent on the magnetic field B and the temperature T

$$M(B, T) = g_J \mu_B J B_J(x) \quad , \quad x = \frac{g_J \mu_B J B}{k_B T} \quad (3.3)$$

where B_J is the Brillouin function [80]. In the limit of $x \ll 1$, B_J can be developed and equation 3.3 rewrites for the susceptibility $\chi = \frac{M}{B}$ as

$$\chi = \frac{C}{T} \quad (3.4)$$

with the molar Curie constant $C = \frac{N \mu_B^2 \mu_{eff}^2}{3k_B}$ where

$$\mu_{eff} = g_J \sqrt{J(J+1)} \mu_B \quad (3.5)$$

is the paramagnetic free ion moment; the maximal moment in the ordered (e.g. ferromagnetic or antiferromagnetic) phase is given by $\mu_{max} = g_J J \mu_B$.

In a dense array of magnetic atoms, an applied external magnetic field B_a causes a finite magnetisation M which in turn provokes a finite molecular (or exchange) field $B_M \approx \lambda M$. Thus, $B = \mu_0(H + M)$ and the relation for the magnetisation is given by $M = \chi_p(B_a + \lambda M)$ where χ_p is the paramagnetic susceptibility, which finally leads to the Curie-Weiss law

$$\chi = \frac{C}{T - \theta_p} \quad (3.6)$$

where $\theta_p = \lambda C$ is the paramagnetic Curie-Weiss temperature, which in the molecular field approximation is identical with the ferromagnetic Curie temperature T_C .

3.3 Experimental

The magnetization of these ternary compounds was measured in magnetic fields up to 8 Tesla in the temperature range between 1.5 and 300 K by an

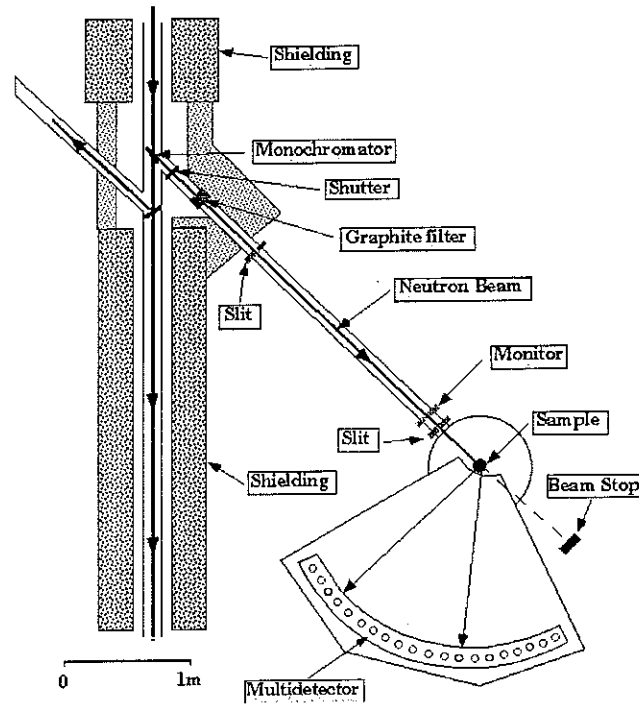


Figure 3.1: Sketch of the D1B two axis diffractometer at the Institut Laue Langevin. The figure is reproduced from [82].

extraction method [81]. The corresponding susceptibility was then extracted from the slope of each isotherm.

Elastic neutron diffraction measurements were performed at the Institut Laue Langewin (ILL) in Grenoble at the D1B two-axis powder diffractometer using thermal neutrons with a wavelength of $\lambda = 2.522 \text{ \AA}$ (figure 3.1). The diffracted neutrons were then collected by an $^3\text{He}/\text{Xe}$ position-sensitive detector composed of a system of multi-electrodes with 400 cells which span an angular range of 80° . In order to minimize oxidation, the samples were crushed directly before the measurement and then held in a cryostat for temperatures down to 1.2 K in a cylindrical vanadium container of 4 mm to 6 mm diameter and 3 mm in the case of DyNiSb in order to reduce absorption of the neutrons by the Dy nuclei. The powder diffraction data were analyzed by the Rietveld refinement technique using the program Fullprof [83].

3.4 Results

3.4.1 Magnetisation and susceptibility

The magnetization was measured for all these RNiSb ternary compounds ($R=Y, La, Ce, Pr, Nd, Gd, Tb, Dy, Ho, Er, Yb, Lu$) by an extraction method in magnetic fields up to 8 Tesla in the temperature range between 1.5 and 300 K. For example the magnetisation curves are shown for the ferromagnetic NdNiSb in figure 3.2 and for the antiferromagnetic TbNiSb in figure 3.3. All RNiSb compounds with a partly filled 4f shell show a Curie-Weiss behaviour (equation 3.6) at high enough temperatures, as proved by more or less straight lines in the inverse susceptibility graphs, given in the figures 3.4 and 3.5 and discussed in the following. Some magnetic properties derived from these magnetisation and susceptibility experiments are summarized in table 3.1 at the end of this paragraph, together with the values obtained by elastic neutron diffraction data.

The inverse susceptibility of CeNiSb shows a deviation from the Curie-Weiss law below 30 K due to crystal field effects. At 3 K the susceptibility diverges indicating an onset of the ferromagnetic magnetization with a rather weak spontaneous magnetization of $0.3\mu_B$ and a large superposed susceptibility. The latter may result either from a strong anisotropy which leads to a high saturation field, or from a second antiferromagnetic or modulated component. The latter hypothesis is confirmed by elastic neutron scattering experiments presented in the following paragraph 3.4.2.

In PrNiSb the inverse susceptibility shows a Curie-Weiss behaviour above 40 K; while extrapolated toward very low temperatures, the value of $1/\chi$ does not drop to zero, but tends to a constant value as visualised in the inset of figure 3.4. Since Pr has an even number of electrons ($J_{Pr} = 4$), it is a non-Kramers ion, non-degenerated levels can exist in absence of a magnetic field and PrNiSb has most probably a non-magnetic ground state. Thus, PrNiSb does probably not order magnetically.

The inverse susceptibility of NdNiSb is linear above 50 K, showing an ideal Curie-Weiss behaviour in the paramagnetic temperature range. Arrott - Belov plots display the onset of a spontaneous magnetization near 23 K which reaches a value of $0.8\mu_B$ at 1.5 K. As typical for a ferromagnetic material, the low field susceptibility curve has a sharp peak around the Curie temperature with its maximum at 26 K close to the Curie point T_C obtained from resistivity measurements. As for CeNiSb, the magnetization curves show a large superposed susceptibility.

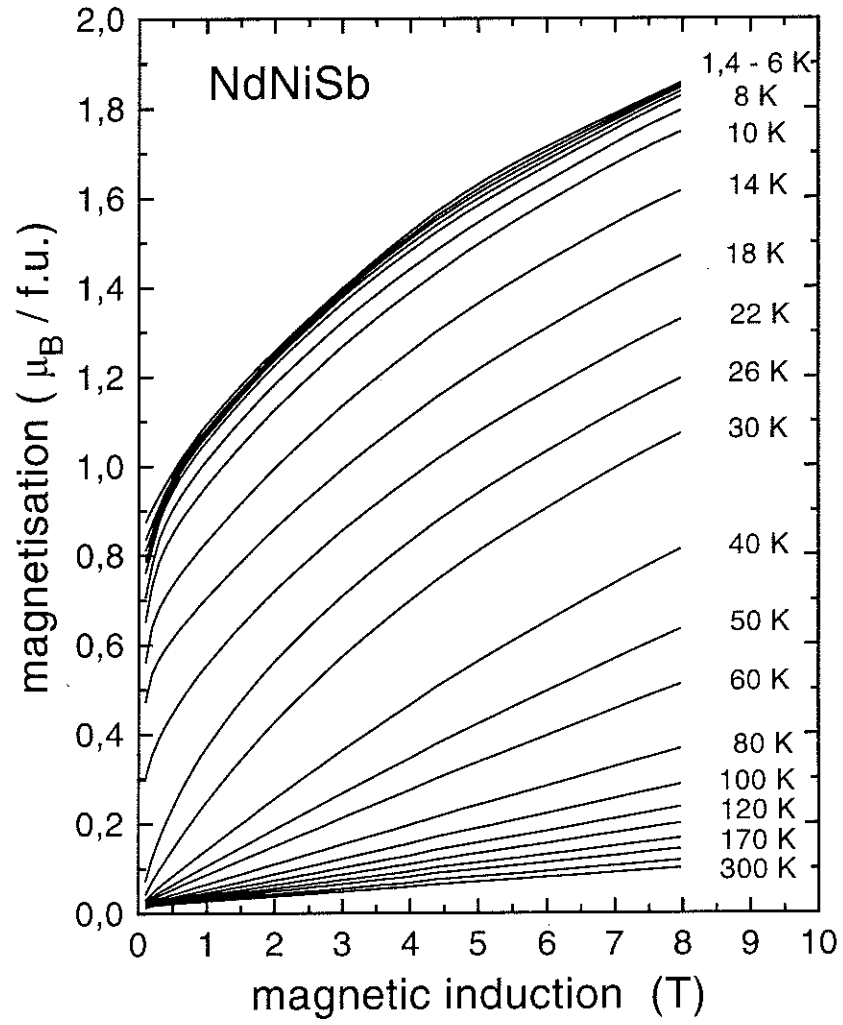


Figure 3.2: Magnetisation per formula unit for a NdNiSb polycrystal at different temperatures

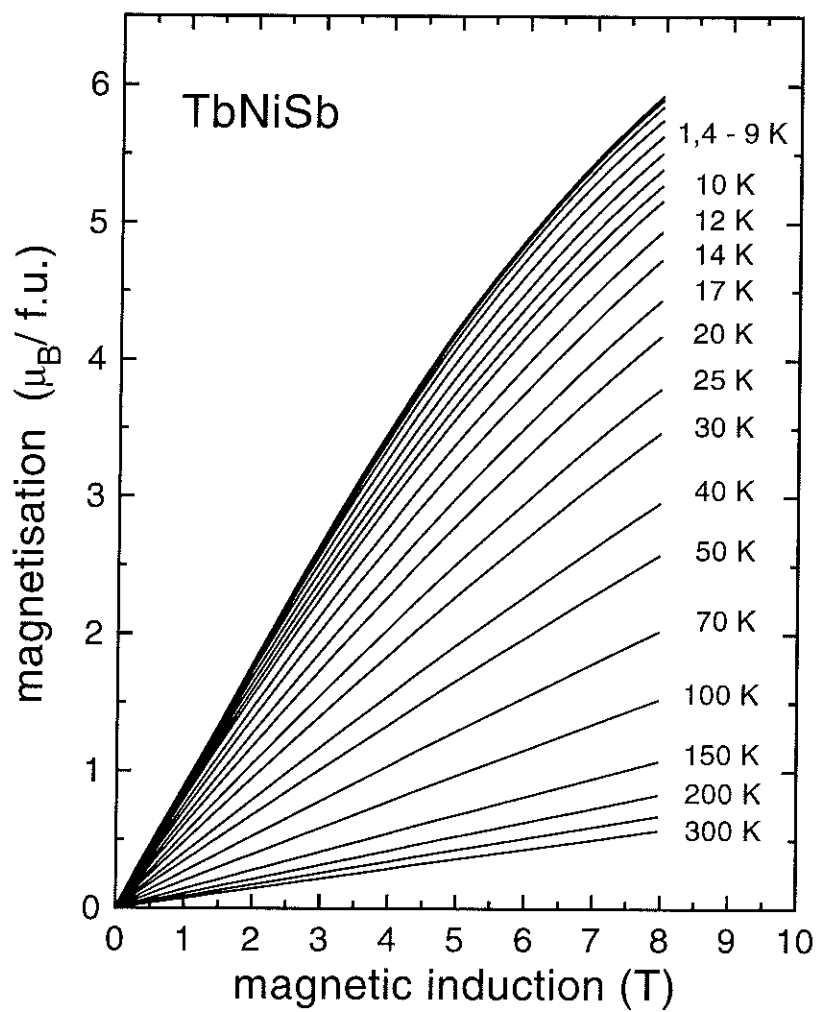


Figure 3.3: Magnetisation per formula unit for TbNiSb at different temperatures

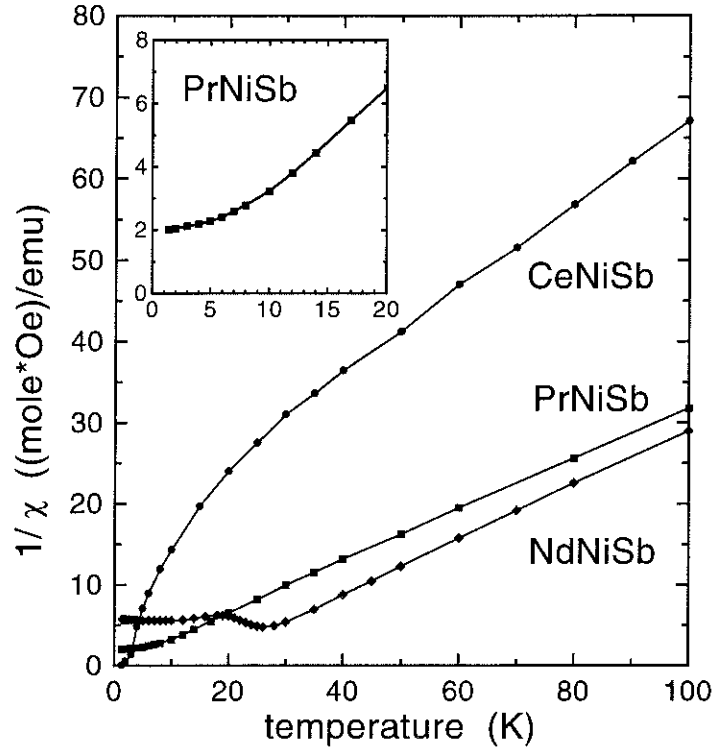


Figure 3.4: Temperature dependence of the inverse magnetic susceptibility of CeNiSb, PrNiSb and NdNiSb

The inverse susceptibility curves of TbNiSb, DyNiSb, HoNiSb and ErNiSb show Curie-Weiss behaviour down to at least 10 K as given in figure 3.5. For TbNiSb, the slope changes near 5.5 K, indicating the onset of the antiferromagnetic ordering in complete agreement with the values found by resistivity measurements. Similarly, the susceptibility curve of DyNiSb has a small maximum at 3.5 K, indicating again that the Néel temperature can be situated in that region. No clear ordering point could be defined for HoNiSb and ErNiSb on the basis of the present magnetisation measurements as the T_N value lies at the end of the investigated temperature range. However, neutron diffraction data indicate a Néel temperature around 2.5 K for HoNiSb and even lower for ErNiSb.

The values of μ_{eff} derived from susceptibility experiments, are less accurate, but extracted from fitting the whole temperature range and are thus not affected by the saturation problem. They lead to experimental effective moments μ_{eff} which are found to be slightly larger than the theoretical value

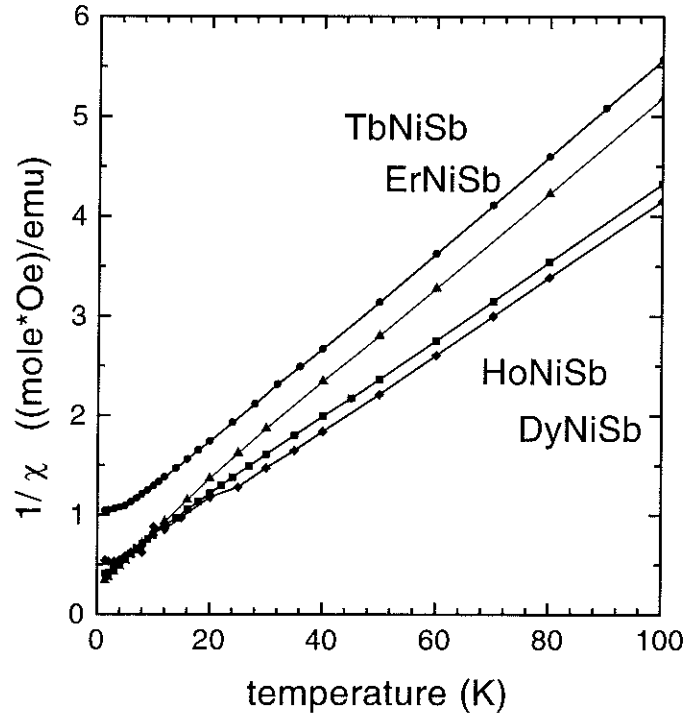


Figure 3.5: Temperature dependence of the inverse magnetic susceptibility of TbNiSb (circle), DyNiSb (diamond), HoNiSb (square) and ErNiSb (triangle)

$\mu_{eff} = g_j \sqrt{J(J+1)}$ for a free R^{3+} ion, probably caused by the influence from Ni which gives an additional Pauli-like susceptibility.

Caused by the vanishing moments of the empty or filled 4f subshell, the magnetic properties differ substantially for the paramagnets YNiSb, LaNiSb and LuNiSb. LaNiSb is a Pauli-paramagnet with a small Pauli susceptibility of about $2.4 \times 10^{-9} m^3/mole$ roughly constant with the temperature. This order of magnitude is typical for a Pauli paramagnet, close to that found in TiNiSb [25] and agrees with the value of $1.8 \times 10^{-9} m^3/mol$ measured previously [41]. Similarly, YNiSb is also a paramagnet with a small susceptibility increasing from $2 \times 10^{-9} m^3/mol$ at low temperatures to $11 \times 10^{-9} m^3/mol$ at 300 K - which is still not understood - whereas LuNiSb exhibits a value of around $1.3 \times 10^{-8} m^3/mol$ for its constant paramagnetism.

Magnetic Properties of RNiSb

Compound	T_C, T_N (K)	Θ_p (K)	μ_{exp} (μ_B)	μ_{th} (μ_B)	Propagat. vector	M(1.5K) (μ_B)	type of magnetism ^a
YNiSb							CP
LaNiSb							PP
CeNiSb	3.5	-27	2.9	2.54	(0, 0, 0) +(0, 0, $\frac{1}{4}$)	? ^b	CW, F+Mod
PrNiSb	-	-0.7	3.8	3.58	-	-	CW
NdNiSb	23	13	3.7	3.6	(0, 0, 0)	2.37 (9) (0001)	CW, F
TbNiSb	5.5	-17	9.7	9.7	($\frac{1}{2}, \frac{1}{2}, \frac{1}{2}$)	5.62 (6) (110) ^b	CW, AF
DyNiSb	3.5	-9.8	10.9	10.64	($\frac{1}{2}, \frac{1}{2}, \frac{1}{2}$)	6.13 (27) (100) ^b	CW, AF
HoNiSb	2.5	-10.8	10.7	10.61	($\frac{1}{2}, \frac{1}{2}, \frac{1}{2}$)	4.52 (8) (110) ^b	CW, AF
ErNiSb	≈ 2	-6.8	9.6	9.58	($\frac{1}{2}, \frac{1}{2}, \frac{1}{2}$)	(100) ^b	CW, AF
LuNiSb							CP

^a CP = Constant paramagnet, PP = Pauli-paramagnet,^a CW = Curie-Weiss paramagnet, AF = Antiferromagnetic component,^a F = Ferromagnetic component, Mod = Modulated magnetic moment,^b See discussion in the text

Table 3.1: Magnetic properties of RNiSb

3.4.2 Elastic neutron diffraction

A more detailed analysis of the magnetic structures was performed by the means of elastic neutron diffraction in combination with a Rietveld refinement method on five of these RNiSb compounds, on CeNiSb, NdNiSb, TbNiSb, DyNiSb and HoNiSb, which will be discussed sample by sample in the following. The results of the refinements at the lowest temperature are given in table 3.1

CeNiSb The neutron diffraction pattern confirm the occurrence of the ZrBeSi-type crystallographic structure, with lattice parameters already given and discussed in table 2.2 on page 24. As CeNiSb is far more reactive than all

other examined compounds, crushing the sample is sufficient to oxidize the powder slightly, even if the sample is prepared directly before the experiment, regardless whether it is crushed at air or under alcohol. Thus, the diffraction patterns of both samples contain, in addition to the CeNiSb reflections, spurious peaks corresponding to CeO and also to a small amount of CeSb. Because of the weak intensity expected for the magnetic peaks, at least six hours were spent to collect the intensities above and below the ordering temperature, leading nevertheless to diffraction patterns which look identical at first glance. However, very slight modifications related to the magnetic order are observed in the difference plot between two patterns taken at 1.3 and 15 K (figure 3.6), in which the maximum change in intensity is less than one hundredth of the most intense nuclear reflection; the measurements on both samples gave the same qualitative results.

The first peaks, corresponding to the (002) and (004) nuclear reflections, are slightly shifted towards larger angles at the lower temperature (1.3 K), while contrarily the peaks originating from the (110) and (112) ones are shifted towards lower angles, as visible in the difference plot (1.3–15 K) given in figure 3.6. This observation can be explained by magnetostrictive effects, where the lattice parameter a becomes larger and the parameter c smaller below the magnetic ordering point. The direct analysis of the lattice parameters at each temperature with the Rietveld refinement is not accurate enough to give a reliable value of the magnetostriction, possibly because the hexagonal symmetry may not be exactly preserved in the ordered state.

Several reflections of magnetic origin can be identified in the difference plot (1.3–15 K), one of them corresponds to a faint enhancement of the (010) nuclear reflection being related to a ferromagnetic component. Indeed, the magnetisation measurements have revealed a ferromagnetic component reaching a value of about $0.3 \mu_B$ at 1.5 K. Since no magnetic signal seems to appear on the (002) nuclear reflection, the ferromagnetic component should be aligned along the c axis of the cell. However, due to the statistical error bars and the possible change in the nuclear structure factors, it is not possible to get a reliable estimate of the ferromagnetic component.

Other reflections appear for angles corresponding to a non-commensurate or long wavelength modulated magnetic structure. Particularly, an intense low angle reflection appears at $2\theta = 4.6^\circ$ representing the satellite of the origin and the satellite peaks embedding the (002) and (012) reflections corresponding to a propagation vector $\vec{Q} = (0, 0, 0, \frac{1}{4})$. Hence, these reflections show that the zero-field magnetic structure of CeNiSb is not purely ferromagnetic, as assumed before on the basis of magnetization data [37], but pos-

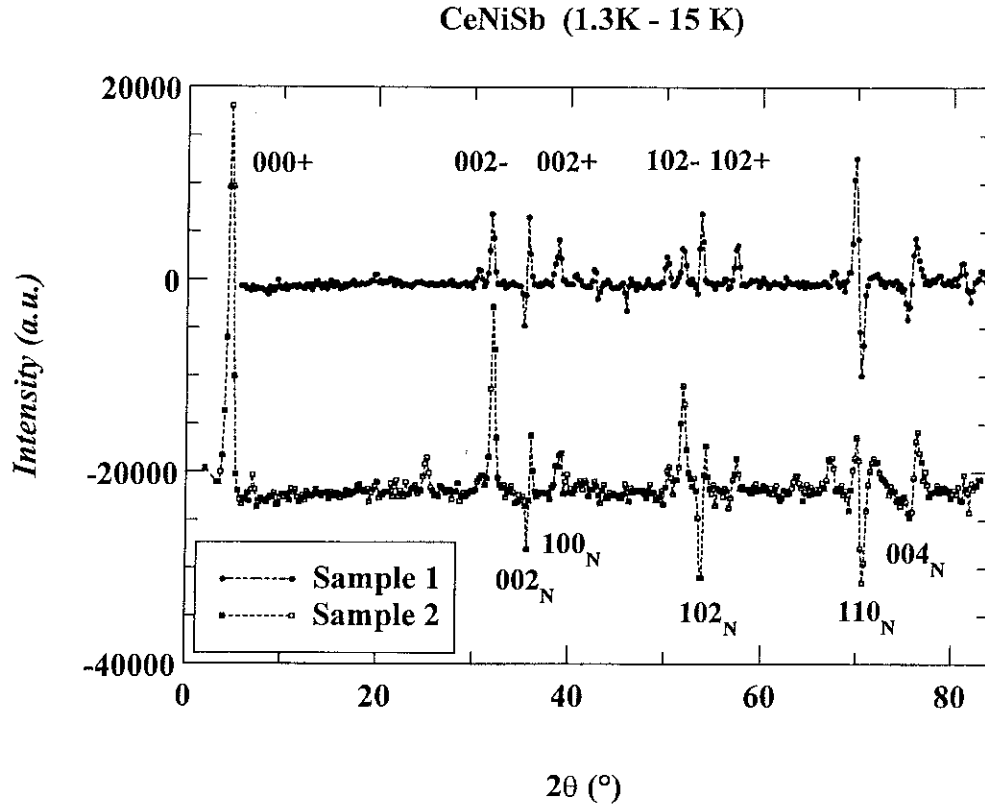


Figure 3.6: Difference neutron diffraction patterns (1.3 - 15 K) for two CeNiSb samples, showing magnetic reflections, including the (100) one (possibly of ferromagnetic origin), and the thermal shift of the nuclear reflections. (The intensity scale has been shifted for the second sample for clarification.)

sesses an additional modulated moment. Similarly, an amplitude-modulated structure has previously been observed in the isomorphous compound Nd-PdSb [76] below T_N , but with a different propagation vector. Moreover, the peculiar properties of CePdSb [48] may be related to the appearance of a modulated component above 10 K.

NdNiSb In addition to NdNiSb, this sample contains small amounts of the cubic Nd_2O_3 phase, responsible for at least three weak lines, which were not taken into account in the refinement process, as they do not interfere much with the reflections of the main phase. In agreement with X-ray powder diffraction data (chapter 2.4), the neutron diffraction patterns, taken in the paramagnetic range (above 26 K), confirm the hexagonal ZrBeSi-type

crystal structure of NdNiSb which is an ordered superstructure of the AlB₂-type phase. For instance, the presence of the (011) and (013) superstructure reflections confirm the doubling of the c parameter, compared to the disordered AlB₂ phase (nuclear R_n factor = 7.4%). Here, the atomic positions are located at [84]: Nd in (2a) (0,0,0), Ni in (2c) ($\frac{1}{3}, \frac{2}{3}, \frac{1}{4}$) and Sb in (2d) ($\frac{1}{3}, \frac{2}{3}, \frac{3}{4}$). A slightly different structure involving the P6₃/mc space group has been observed in the hexagonal phase of HoPdSb [85], where, at variance to the P6₃/mmc space group, the atomic positions have a free z parameter. A refinement of this structure leads then to a significant improvement of the R_n factor (5.9%), provoking only a slight shift of the Nd atomic position to (0,0, 0.021 ± 0.0014).

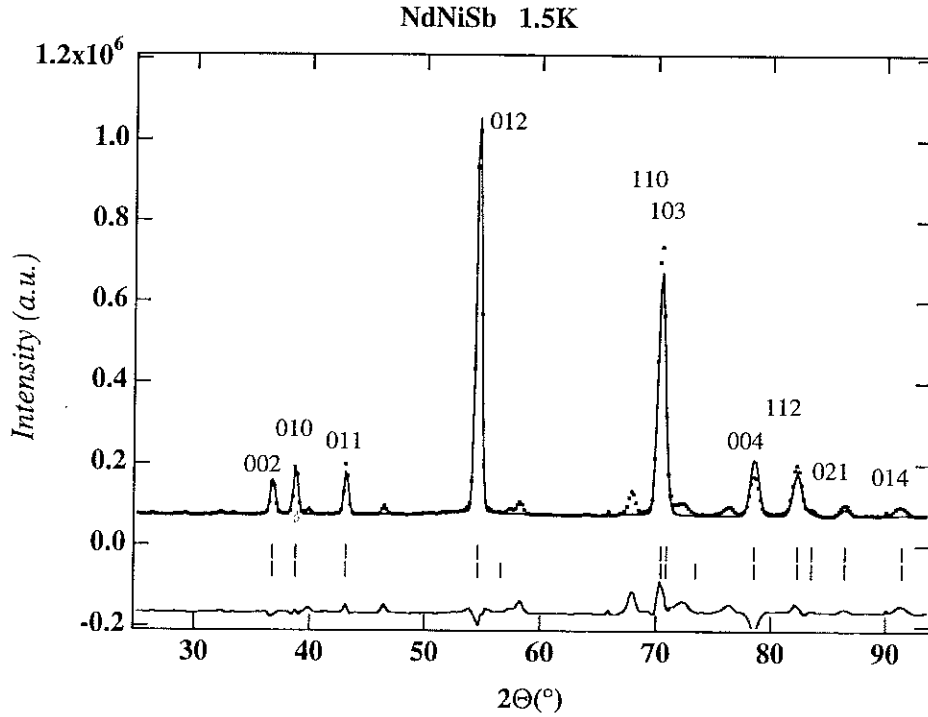


Figure 3.7: Elastic neutron diffraction pattern of NdNiSb at 1.5 K together with the Rietveld refinement of the nuclear and ferromagnetic reflections. The (002) reflection is entirely nuclear, the (010) one almost entirely magnetic.

Below the Curie temperature ($T_C=23$ K), additional magnetic intensities appear for angles corresponding to the nuclear reflections (figure 3.7), giving a propagation vector $\vec{Q} = (0,0,0)$; for instance, the intensity of the (010)

reflection is nearly entirely of magnetic origin. Conversely, since no extra intensity appears for the (002) or (004) reflections, the magnetic moments are therefore oriented parallel to the c crystal axis. The Rietveld refinement of the magnetic structure reveals that the moments are located on the two Nd atoms in the cell and are oriented parallel to each other, creating so a ferromagnetic structure with a magnetic moment $\mu = 2.37 \pm 0.09 \mu_B$.

TbNiSb, DyNiSb, HoNiSb In addition to the main cubic RNiSb phase, weak reflections are sometimes observed corresponding to NiSb (S.G. $P6_3/mmc$) and probably to some allotropic form of rare earth oxides; as the attribution of these lines is not certain, they were not taken into account in the refinement process. The refinement of the nuclear structure of all three compounds leads to a good agreement factor ($R_n = 5\% - 7\%$) with the cubic semi-Heusler structure (MgAgAs-type, SG: $F\bar{4}3m$), without any adjustable occupancy parameter locating the atomic positions at $R = (0, 0, 0)$, $Sb = (\frac{1}{2}, \frac{1}{2}, \frac{1}{2})$ and $Ni = (\frac{1}{4}, \frac{1}{4}, \frac{1}{4})$. No appreciable distortion of the cell was detected from the difference patterns taken below and above the Néel temperature.

In addition to the nuclear peaks, the low temperature patterns of all these three compounds exhibit magnetic lines which can be indexed using a propagation vector $\vec{Q} = (\frac{1}{2}, \frac{1}{2}, \frac{1}{2})$ belonging to a simple antiferromagnetic ordering with the magnetic moments situated on the RE atoms.

The presence of an additional short range magnetic order is indicated by the observed significant broadening at the basis of magnetic lines, e.g. the $(\frac{1}{2}, \frac{1}{2}, \frac{1}{2})$ one, which can be decomposed into a gaussian line with a width close to the one of the nuclear reflections, and into a lorentzian line containing about 10% of the peak intensity at 1.5 K. The latter lorentzian contribution possesses a much larger width of $WHM = 0.84^\circ$ corresponding in direct space to about 27 times the lattice parameter. The intensity and the width of the lorentzian line increase with temperature, the WHM reaches its maximum of 3.6° at 8 K (just above the Néel temperature). The deduced correlation length is about 6 times the lattice parameter at T_N and subsequently decreasing at higher temperatures. This effect can be attributed to short range order in the paramagnetic state which is still present at $3 T_N$; in the antiferromagnetic range, it may also correspond to some stacking faults.

Figure 3.8 shows the data for TbNiSb at 1.5 K, together with a Rietveld refinement fit of the nuclear reflections (assuming a gaussian shape) and the magnetic reflections (using a pseudo-Voigt lineshape). From the refinement, the magnetic moments are oriented perpendicular to the propagation vector

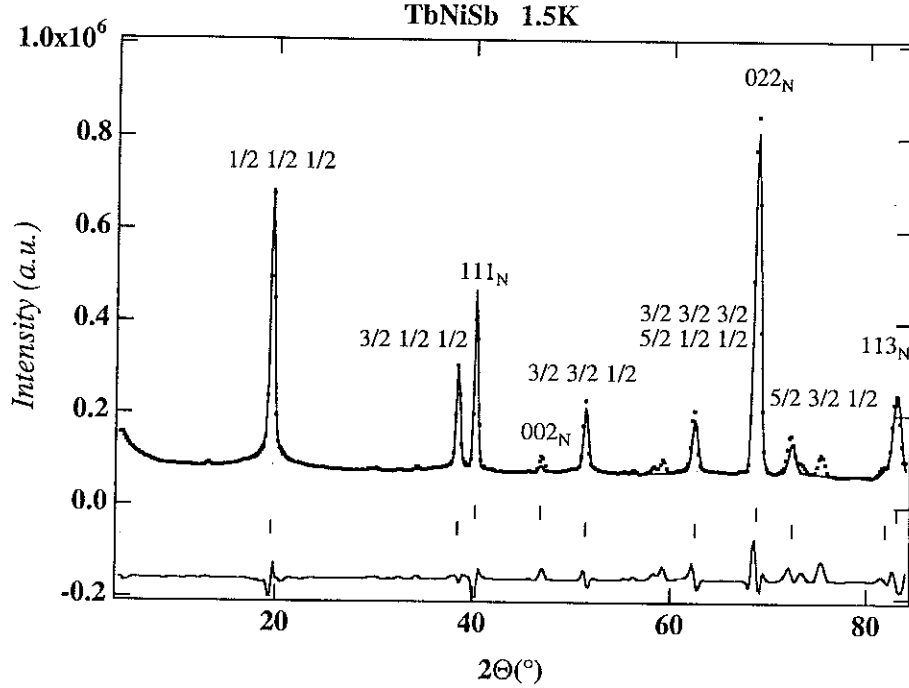


Figure 3.8: Elastic neutron diffraction pattern of TbNiSb at 1.5 K together with the Rietveld refinement of the nuclear and antiferromagnetic reflections.

\vec{Q} for TbNiSb and HoNiSb (the magnetic R_m factors are 5% for Tb and 5.5% for Ho respectively). Most probably the moments are directed along a binary (1,-1,0) axis, provided the structure is a simple collinear one. The ratios of intensities between different magnetic reflections for TbNiSb do not change between 1.5 and 4.5 K, only the magnitude of the moment decreases. The same structure has been observed in the cubic phases of HoPdSb and DyPdSb [85]. Contrarily, in DyNiSb, the magnetic moments are not orthogonal to \vec{Q} , they may be directed - assuming a collinear structure - either along a (1,0,0) quaternary axis, or at a corresponding angle relative to \vec{Q} direction as will be discussed later (the R_m factor is only 17% due to the necessary absorption corrections). The results of the refinements at the lowest temperature are given in table 3.1.

3.5 Discussion

CeNiSb has a complex magnetic structure built from a weak ferromagnetic component and a modulated one. Magnetisation and susceptibility measurements show a weak ferromagnetic magnetization at 1.5 K together with a large superposed susceptibility which is, according to the results of neutron diffraction, mainly due to the evolution of the modulated magnetic component. CeNiSb exhibits, in analogy with the binary CeSb compound, a magnetostrictive behaviour which occurs below the ordering point [86], probably related to Kondo-like properties [36, 37, 43]. The Kondo effect has an important influence in CeNiSb, as found by resistivity measurements (chapter 4.4) and proved by inelastic neutron scattering (chapter 5.5).

NdNiSb is a simple ferromagnet with moments along the c axis reaching $2.37 \mu_B$ at 1.5 K, a value smaller than the one for the free ion ($3.27 \mu_B$). Magnetization measurements on polycrystalline samples have shown only a weak spontaneous magnetization of about $0.8 \mu_B$ at 1.5 K, which rises quite rapidly up to $1.8 \mu_B$ under 8 Tesla. Hence, the lack of saturation in low fields must then be ascribed to the polycrystalline samples and to a quite large uniaxial magnetocrystalline anisotropy.

From the results of transport measurements (chapter 4.4), both Ce and Nd compounds are probably semimetals with a weak density of states at the Fermi level, possessing thus a small wavevector k_F at the Fermi level which may in this case favour the observed ferromagnetic (or modulated) order. Ruderman-Kittel interactions in these metallic samples give rise to much higher interactions than superexchange processes which occur in heavy rare earth semiconducting compounds.

PrNiSb in turn remains paramagnetic over the whole temperature range, due to the non magnetic ground state, provoked by its special crystalline electric field level configuration as will be analysed later (figure 5.7 in chapter 5.4).

The cubic RNiSb compounds containing a heavy rare earth element, Tb, Dy, Ho or Er, order antiferromagnetically at low temperatures with the same propagation vector $\vec{Q} = (\frac{1}{2}, \frac{1}{2}, \frac{1}{2})$. These compounds are semiconductors where superexchange interactions should be dominant. Thus, interactions are likely of short range type, dominated by nearest neighbour interactions. Negative interactions will then favour the observed commensurate antiferromagnetic ordering.

According to the magnetic intensities, the angle between moments and the propagation vector is different in Tb and Ho on the one hand, and Dy and Er on the other hand. If the structures are simply colinear antiferromagnetic ones -that is if there are no multiaxial structures-, the most probable high symmetry directions for the moments are (110) for Tb and Ho, (100) for Dy and Er respectively. In a similar way, the easy axis direction changes for example between TbZn and HoZn compounds on the one hand, DyZn and ErZn on the other hand [87]. These directions are ruled by the crystalline electric field (CEF), which tends to align the moments at low temperature along one of the high symmetry axes of the cubic structure, depending on the signs of the fourth and sixth order CEF parameters. In fact, these magnetisation results are in complete agreement with the directions calculated on the basis of the CEF, which in turn explains the origin for this magnetic behavior as will be discussed in detail in connection with inelastic neutron scattering (chapter 5.5).

However, although a colinear structure is probable in these heavy RNiSb compounds, non-colinear magnetic structures sometimes occur in cubic compounds [88]; they cannot be evidenced or ruled out by a simple powder diffraction experiment or by magnetisation measurements on polycrystals. The absence of any visible magnetostriction prevents to distinguish the real symmetry of the magnetically ordered phase.

It is worth comparing these results with magnetic structures obtained on RSb binary pnictides [86] from which the heavy RNiSb compounds may be deduced by inserting one Ni atom in one over two of the tetrahedral voids [67]. One remarkable aspect is that, for both heavy rare earth series, the compounds are semiconductors and the magnetic structures have the same propagation vector. This indicates that the Ni atoms play thus the role of rather neutral insertion atoms in this structure, especially since they do not carry a magnetic moment, which is entirely located on the rare earth atom. Moreover, the Ni influences the relative weight between the fourth and sixth order CEF terms provoking a rotation of the magnetic moments as analysed later (chapter 5.5). While in RNiSb the 6th order CEF term dominates, the fourth order one plays the dominant role in RSb, resulting in a threefold axis for HoSb, and a fourfold one for TbSb and DySb with a large tetragonal magnetostriction occurring in DySb [88, 86].

For all compounds, the same value of the Néel temperature is found by magnetisation, neutron and resistivity measurements. But the magnitudes of the ordered magnetic moments obtained by elastic neutron scattering at 1.3–1.5 K are in all cases smaller than the free ion values (at 0 K) (see ta-

ble 3.1. This may arise mainly from the fact that ordering points are quite low and that the measurements in the ordered range were performed only down to 1.3 or 1.5 K, which is not enough to reach the saturation magnetization - except for NdNiSb. Nevertheless, it may again indicate that CEF effects play an important role in these compounds. Moreover, the Ce moments are further reduced by the Kondo effect and the modulation of the magnetic structure.

3.6 Conclusion

The compounds in the RNiSb series exhibit a large variety of different magnetic properties, ranging from pure ferromagnets (NdNiSb), ferromagnets with an additional modulated magnetic moment (CeNiSb), over antiferromagnets (Tb-, Dy-, Ho-, ErNiSb) with different magnetisation directions, to compounds with a non magnetic groundstate (PrNiSb) which remain thus paramagnetic in the whole temperature range. The compounds at the beginning and end of this series (Y-, La-, LuNiSb) are Pauli- or constant paramagnets due to their empty or filled 4f shell. The magnetic moments were found to be located entirely on the rare earth atoms, making the Ni atoms a rather neutral insert into the crystallographic structure, not affecting most of the magnetic properties. In the scope of this analysis, magnetisation, susceptibility and neutron diffraction measurements give complementary information for characterizing the magnetic behaviour and are helping to identify the magnetic coupling mechanisms. In CeNiSb and NdNiSb, the coupling should take place via comparatively large indirect RKKY interactions involving conduction electrons. The small wavevector k_F at the Fermi level in these probably semimetallic compounds favours then the observed ferromagnetic or modulated magnetic order. As opposed to this, the semiconducting character favours in the heavy rare earth compounds superexchange interactions, which are likely to be of short range, dominated by the nearest neighbour interactions. Negative interactions will then favour the observed commensurate antiferromagnetic ordering.

The special magnetic behaviour within this compound series originates from the unbalanced electrons in the partly filled 4f subshell, described in section 2.2 and measured directly with photoemission techniques (chapter 6). These localized magnetic 4f moments, embedded in the crystal structure, give then rise to a large variety of properties and physical effects of the rare earth compound, strongly controlled by the crystalline electric field levels (chapter 5). The latter are responsible for deviations from the simple laws,

control the direction of the moments, may provoke a reduction of the free ion value and can cause - in special configurations - the annihilation of the ground state magnetic moment.

Chapter 4

Transport properties

4.1 Introduction

The study of the resistivity allows to obtain much information about the electronic structure close to the Fermi level, i.e. the shape of the density of states and the occurrence of energy gaps giving rise to semiconducting behaviour [89, 90]. Resistivity measurements allow to study variations of the magnetic and crystallographic structures, i.e. ordering points and phase transformations since the scattering of the charge carriers changes in these regions. The magnetic scattering is directly related to the spin disorder, the magnetic entropy; its derivative resembles the magnetic contribution to the specific heat. The effects of heavy fermions, the Kondo behaviour, the Schottky anomalies as well as the population of crystal field levels may directly be observed on the shape of the resistivity curve. As in anisotropic materials, e.g. non-cubic monocystals, the electronic scattering depends on the direction of the external electric and magnetic field, resistivity and magnetoresistance measurements allow to study the anisotropy effects and preferential directions. Since the scattering of conduction electrons may be separated in several different processes, an identification of these allows to understand much about the exact structure, energy levels and states of the investigated compounds. However, despite of the variety of information available, the analysis of the resistivity is not always easy and straightforward due to the complexity and since often many processes are involved simultaneously.

Due to the richness of information available, transport properties were often studied in rare earth compounds, reviewed e.g. in [91]. Of particular interest is the behaviour of narrow gap semiconductors as they are in the

region of a metal-insulator transition. A number of magnetic semiconductors has been discovered in ternary 3d compounds having the semi Heusler structure [25]. A large magnetoresistance often appears in narrow gap semiconductors having an internal magnetic shell. It has for example been found in some rare earth ionic compounds [92, 93, 94, 95, 96, 97, 98] as well as in Mn perovskites [99, 100]. In 3d metal semi-Heusler compounds, the magnetic moment disappears when the semiconducting phase is reached and in general only a rather weak negative magnetoresistance is observed. On the other hand, rare earth magnetic semiconductors like RNiSb ($R = \text{Tb, Dy, Ho}$) remain paramagnetic down to low temperatures. In contrast to the 3d magnetism, the magnetic moment of the 4f shell is localized and some of these compounds may show a giant negative magnetoresistance.

4.2 Theory

4.2.1 Metals

The electrical current density $\vec{j} = \vec{\sigma} \vec{E}$ is described in the most general case by the product of the electric field \vec{E} with the conductivity tensor $\vec{\sigma}(B, T) = 1/\vec{\rho}(B, T)$. In cubic compounds, the tensor is reduced to a simple scalar value ρ describing the isotropic resistivity.

In the absence of external magnetic fields, the total resistivity $\rho_{tot}(T)$ of magnetic metals is expressed in dependence of the measuring temperature T by the extended Matthiessen's rule

$$\rho_{tot}(T) = \rho_0 + \rho_{ph}(T) + \rho_m(B, T) \quad (4.1)$$

provided that mean free path between two scattering events is large in comparison to the interatomic distance.

ρ_0 is the temperature independent residual resistivity due to impurities and crystal lattice defects. At 0 Kelvin all other terms vanish for an ordered magnetic lattice and ρ_0 may directly be determined by extrapolating the experimental resistivity curve.

$\rho_{ph}(T)$ describes the scattering of the conduction electrons with the lattice phonons, which is at higher temperatures usually the main part of the total resistivity. Starting from the Bloch theory, Grüneisen has derived the phonon contribution $\rho_{ph}(T)$ to the electrical resistivity for a metal [101, 102]

$$\rho_{ph}(T) = A \left(\frac{T}{\theta_D} \right)^n \int_0^{\theta_D/T} \frac{x^n dx}{(e^x - 1)(1 - e^{-x})} \quad (4.2)$$

where A is a constant characteristic of the metal, θ_D the Debye temperature and the exponent n is 5 in the Grüneisen theory for simple metals. In transition metal compounds, n is generally found between 3 and 4 due to the shape of the Fermi surface.

In the presence of an internal magnetic shell or an applied external magnetic field B , Matthiesen's rule is extended by the term $\rho_m(B, T)$, which describes the scattering of the conduction electrons by the magnetic moments. It is directly related to the spin disorder, the magnetic entropy; its derivative resembles the magnetic contribution to the specific heat. A more detailed analysis of $\rho_m(B, T)$ is given later in section 4.2.3. Generally, $\rho_m(B, T)$ increases with temperature up to the magnetic ordering point T_C , T_N and remains constant or is slowly increasing at higher temperatures in the paramagnetic temperature range. Thus, this behaviour is represented by a clear drop of the resistivity below the ordering temperature, allowing the exact determination of the magnetic ordering point. This extended Matthiesen's rule is exact as long as the different scattering processes are independent and when the relaxation time is isotropic. These assumptions are a good approximation in our systems since the mean free path is large in comparison to the interatomic distance.

4.2.2 Semiconductors

Intrinsic conduction In ideal semiconductors the conductivity is considered proportional to the number of thermally activated charge carriers, lifted from their localized states across the gap towards the conduction band. Hence, this intrinsic conduction $\sigma_{in} = 1/\rho_{in}$ can be described by

$$\rho_{in} = \rho_0 T^{-\frac{3}{2}} e^{\frac{E_g}{2k_B T}} \quad (4.3)$$

where E_g is the energy width of the band gap around the Fermi level assuming a constant mobility of the charge carriers (figure 4.1).

Mixed conduction However, in a real semiconductor, there is often an additional extrinsic conduction present, caused by impurities and defects, which form additional impurity levels or bands within the gap (figure 4.2). This extrinsic conduction is proportional to the number of ionised donor and acceptor states. Assuming that - as far as conduction processes are concerned - the electrons in different bands do not interact with each other, it is possible to express this mixed conduction σ_{mix} by the sum of the intrinsic

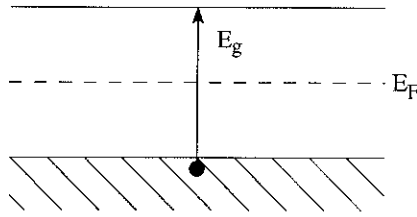


Figure 4.1: Intrinsic energy gap

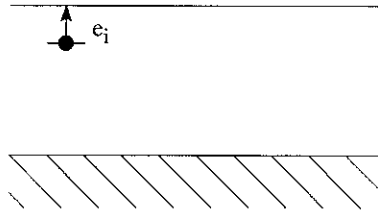


Figure 4.2: Impurity states within the gap

and extrinsic conduction [103].

$$\sigma_{mix} = \sum_i \sigma_i = \sigma_{in} + \sigma_{ex} + \dots \quad (4.4)$$

Hopping conduction When the distance between localized states near the Fermi level, i.e. the impurity levels, is slightly larger than the (impurity) Bohr radius so that their wave functions overlap, the charge carriers can 'hop' from one localized state to another by a quantum-mechanical tunnelling process leading to hopping conduction [104, 105]. At low temperatures, the variable-range hopping (VRH) is expected to dominate and can be expressed in three dimensions by

$$\sigma_{VRH} = A e^{\left[-\left(\frac{T_0}{T}\right)^{1/4}\right]} \quad (4.5)$$

where T_0 is the Mott characteristic temperature; the prefactor A depends on the interactions between the electrons (figure 4.3).

Localization of charge carriers A localization of the one-electron wave function may occur in certain random fields, if the random component is large enough, as it was first shown by Anderson [106] (Anderson localization). Some wave functions are likely to become trapped in the deeper potential wells below a critical energy, the mobility edge E_m [107] (figure 4.4),

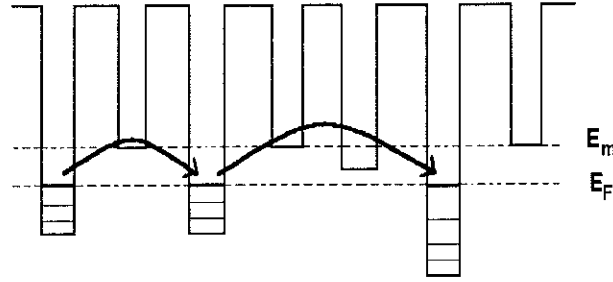


Figure 4.3: Hopping conduction, variable range hopping (VRH)

and their states become localized. Due to random scattering, some charge carriers may migrate under the influence of a magnetic field on a closed path, so that they no longer contribute to the conductivity, leading to a positive magnetoresistance. Since the Anderson localization is related to the impurities and random defects, the contribution to the resistivity can be described by a Mott law as in the case of for an extrinsic semiconductor.

4.2.3 Magnetoresistance

The magnetoresistance (MR) is the change in resistivity $\rho(B)|_T$ under a magnetic field (B), usually normalized by the resistivity in the absence of an external magnetic field:

$$MR = \frac{\rho(B) - \rho(B = 0T)}{\rho(B = 0T)} \quad (4.6)$$

If a huge variation is observed, like in heavy rare earth RNiSb compounds, this magnetoresistance is usually called 'giant magnetoresistance' (GMR). More generally, the magnetoresistance is described by the variations of the diagonal elements in the resistivity tensor $\vec{\rho}_{xx}(B, T)$ in the basic conduction equation 4.1. Many different processes may contribute to the MR effect, which either increase (positive MR) or reduce (negative MR) the resistivity. As opposed to the resistivity, the MR can be anisotropic in cubic materials. Moreover, in the case of an anisotropy, we can distinguish longitudinal MR ($\vec{I} \parallel \vec{B}$) and transversal MR ($\vec{I} \perp \vec{B}$). In the following, the longitudinal MR is studied in order to minimize the cyclotron contribution, which is larger for the transverse configuration.

Cyclotron effect Under the influence of a magnetic field, the charge carriers are exposed to the Lorentz-Force, $\vec{F} = q\vec{v} \times \vec{B}$. which causes a

precession of the electrons with the Larmor frequency $\omega_c = \frac{qB}{m^*}$ around the direction of the applied electric field. As this increases the total length of the path, more collisions take place and thereby increase the resistivity, hence a positive magnetoresistance. This cyclotron effect becomes in general more pronounced when the magnetic field is applied perpendicular to (transversal MR) than along (longitudinal MR) the direction of the electric current.

Magnetic disorder scattering The scattering of the conduction electrons by the magnetic moments is directly related to the spin disorder, the magnetic entropy. Thus, as under the influence of a magnetic field the magnetic order increases for a paramagnet, this leads to a reduced magnetic resistivity, to negative magnetoresistance. De Gennes and Friedel [108] have shown that the magnetic resistivity ρ_m is mainly related to the spin correlation function $\langle S_i S_j \rangle$ by

$$\rho(B, T) = \rho_\infty [S(S+1) - \langle S_i S_j \rangle_{(B, T)}] \quad (4.7)$$

where S is the total spin.

For a paramagnetic compound, the magnetoresistance may be related in weak magnetic fields to the square of the magnetisation M

$$\frac{\Delta\rho}{\rho} \approx -C \left(\frac{M}{M_0} \right)^2 = -A M^2 \quad (4.8)$$

where M_0 is the magnetization of the local (4f) moment at 0 K, and the coefficient C characterizes the intensity of the MR.

Supposing that the Fermi surface is little disturbed by the magnetic order, ρ_m decreases in the ordered temperature range of a magnetic compound like the square of its spontaneous magnetization $M^2(T)$ and remains constant above the ordering temperature T_C since the correlations between the spins S_i, S_j vanish in the paramagnetic temperature range according to the molecular field approximation.

In the case of rare earth compounds, the magnetic resistivity does not stay constant but tends towards $\rho_\infty \approx (g_j - 1)^2 J(J+1)$ increasing with temperature since the crystal field lifts the degeneracy of the 4f levels (see chapter 5.2). The resistivity in the paramagnetic temperature range depends on the number of occupied crystal field levels and on the diffusion probability from one state to another. Generally, the applied field has a weak direct effect on the conduction electrons in rare earth compounds. It acts through the polarisation of the 4f shell and the 4f-5d coupling.

Reduction of the band gap; Mobility edge A further magnetoresistance mechanism is directly related to the band splitting around the Fermi level. As the valence electrons are polarized by the aligned magnetic moments of the rare earth 4f-shell, the density of states is split into two subbands, with the spins parallel and antiparallel to the 4f moments. These bands move into different directions under the influence of an external magnetic field causing, in the case of a magnetic semiconductor, a shift of the Fermi energy towards the mobility edge and thus the reduction of the localisation energy $E_{M\uparrow} - E_F$, for instance of spin up carriers (figure 4.4). For this reason, more charge carriers will be mobile, thereby reducing the resistivity (negative magnetoresistance). This may have a large effect, depending on the importance of the states around the mobility edge for the conduction process. In the case where the mobility edge would cross the Fermi level, a transition to a metallic state is expected (Anderson transition).

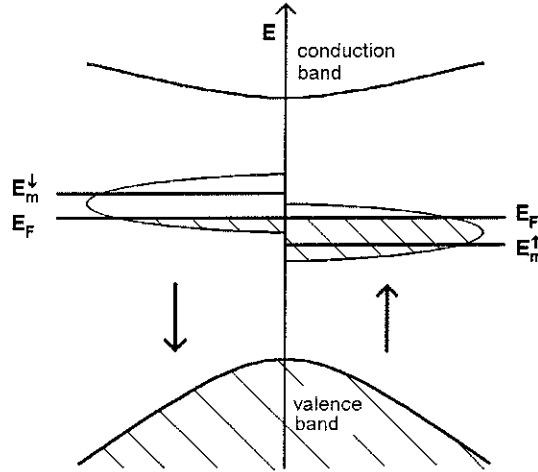


Figure 4.4: Energy scheme of the polarized semiconductor

4.3 Experimental

The resistivity and magnetoresistance measurements were performed at the Laboratoire de Magnétisme Louis Néel, CNRS, in Grenoble with the magnetoresistance apparatus described in [109]. The experimental principle is based on the well known Ohm's law for the resistance $R = \frac{U}{I}$ or for the resistivity $\rho = \frac{U}{I} \frac{A}{l}$ where U is the tension, I the current, l the distance between the measuring points and A the area through which the current passes.

The samples used were first cut by spark erosion into long bars, then measured in the temperature range from 1.5 to 300 K using alternating current with a frequency of 80 Hz and a lock-in amplifier. In the case of the magnetoresistance, a uniform external magnetic field up to 8 Tesla was applied along the direction of the current through the sample.

4.4 Resistivity in metals

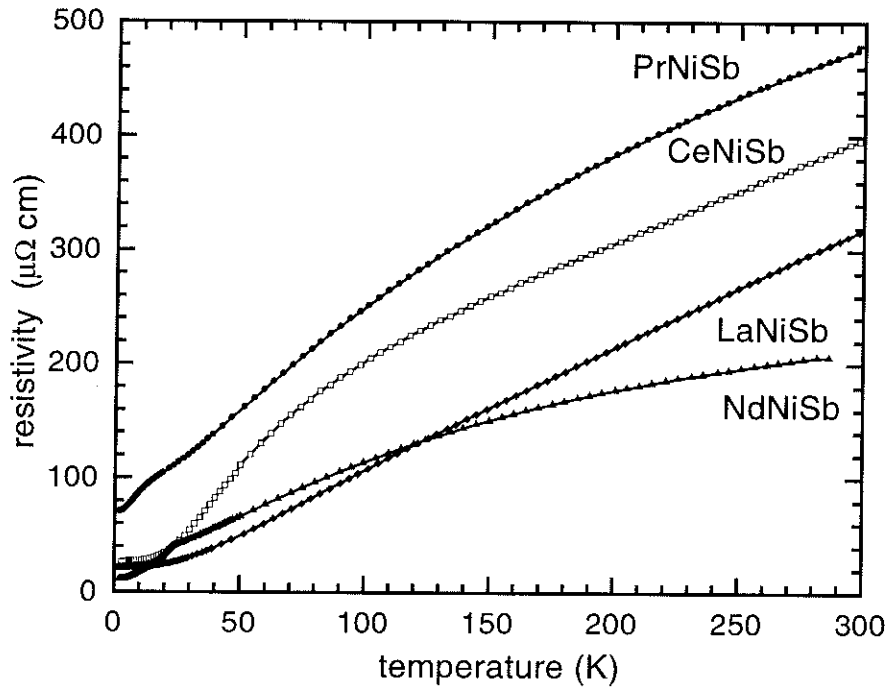


Figure 4.5: Electrical resistivity of La-, Ce-, Pr- and NdNiSb in the temperature range between 1.5 to 300 K

Within the RNiSb ($R=\text{La}, \dots, \text{Lu}$) series, the transport properties vary strongly between compounds containing light and heavy rare earth elements, which may firstly be related to the change in the crystallographic structure.

The compounds containing a light rare earth element (La, Ce, Pr, Nd) are metallic (figure 4.5), their resistivity increases with temperature reaching at 300 K a value of $315 \mu\text{Ohm cm}$ for LaNiSb, $400 \mu\text{Ohm cm}$ for CeNiSb, $480 \mu\text{Ohm cm}$ for PrNiSb and $220 \mu\text{Ohm cm}$ for NdNiSb. The residual resistivity for the investigated samples remains at $22 \mu\text{Ohm cm}$ for LaNiSb,

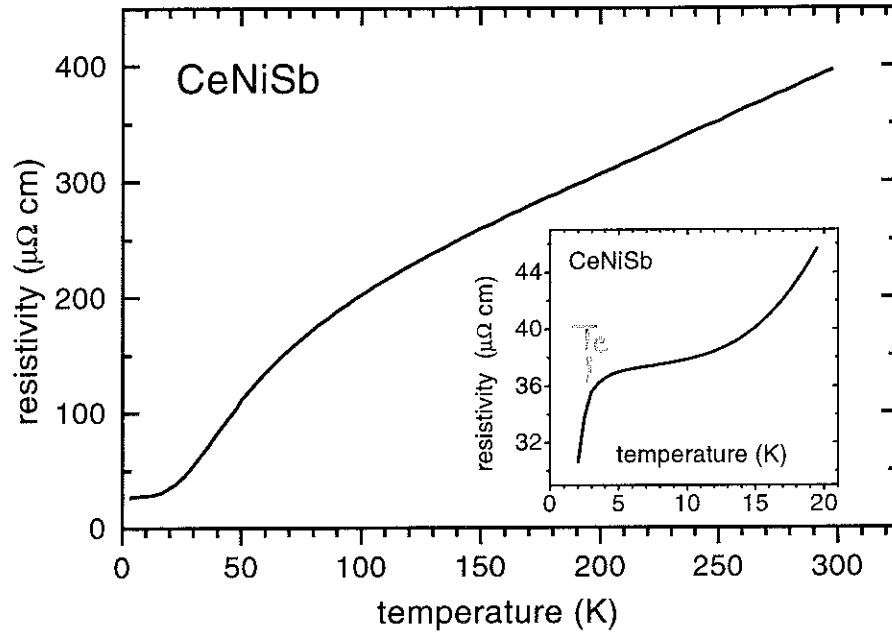


Figure 4.6: Electrical resistivity of CeNiSb in the temperature range from 1.5 to 300 K with an inset at lower temperatures. The magnetic ordering point at 3.5 K is clearly visible as well as the plateau between 5 and 12 K, attributed to the influence of the Kondo effect, which will be proven later by inelastic neutron scattering.

70 $\mu\text{Ohm cm}$ for PrNiSb and 10 $\mu\text{Ohm cm}$ for NdNiSb respectively. For CeNiSb the resistivity has at 2 K a value of 30 $\mu\text{Ohm cm}$ with a quickly falling tendency in the magnetically ordered phase. These values of the residual resistivity indicate a good quality of the samples since the residual resistivity is mainly a measure of the disorder attributed to impurities and lattice defects. Conversely, the rather high value at room temperature probably indicates a rather low density of states at the Fermi level, also supported by X-ray photoelectron spectroscopy measurements discussed in chapter 6.5.

Since La has an unoccupied 4f shell without 4f magnetic moments, no spin disorder scattering contributes to the resistivity in the paramagnetic LaNiSb. Therefore, the resistivity curve represents - apart from ρ_0 - the phonon contribution. The experimental measurements are in very good agreement with calculated curves using the Grüneisen approach (equation 4.2), giving a Debye temperature θ_D of roughly 207 K with $n = 3$ for LaNiSb. As phonons should be comparable between compounds with a different rare earth element but with a similar crystal structure, one may subtract the resistivity

of LaNiSb from the resistivity curves of those compounds with a light rare earth element in order to obtain the pure magnetic scattering contribution for that magnetic compound. However, the validity of this subtraction is questionable, as for instance the resistivity curves of LaNiSb and NdNiSb cross near 120 K.

The resistivity of NdNiSb steadily increases from 2 to 300 K, the sudden change of the slope near 23 K is related to the magnetic ordering point, and a negative curvature at higher temperatures is likely to be attributed to the population of excited crystal field levels.

As found in chapter 3.5 and 5.4, PrNiSb does not order magnetically down to 2 K, the resistivity curve does not show any sharp anomaly, it only reveals changes in curvature near 10 and 40 K, which again can be attributed to excited crystal field levels.

The resistivity of CeNiSb increases from $30 \mu\Omega\text{cm}$ at 2 K to $400 \mu\Omega\text{cm}$ at 300 K. The rapid drop below about 3.5 K is due to a reduction of the spin disorder scattering when the magnetic ordering appears. Then a plateau is reached between 5 and 12 K, often observed in Kondo-compounds, suggesting that some Kondo like behaviour is present in CeNiSb. Another proof that this feature is attributed to a strong influence of the Kondo effect will be given later with the help of the crystal electric field determined by inelastic neutron scattering (chapter 5.5). Above this region, the resistivity rises constantly with increasing temperature caused by crystal field effects and phonon contributions. It should be noted that our resistivity values are much smaller than those found in CeNiSb_{0.9} by Menon et al. [37, 38]. Furthermore, earlier measurements by Skolozdra et al. [42] show a different temperature dependence.

The reason for this different shape is not very clear to us, it might be caused by a preferential orientation and strong anisotropy in these samples. As known from uniaxial compounds like CeSi₂ [110] and CeRuSi₂, the anisotropy can strongly affect the behaviour of the resistivity of Kondo systems. However, some constant features appear between these data; a large drop at the ordering point, which varies, according to different authors, between 3.5 and 7 K and a large increase in resistivity between 20 and 50 K. The discrepancies in the magnitude may come from different stoichiometries of the samples. For example, Menon et al. have performed their measurements on CeNiSb_{0.9} and they have noted that their measurements were sample dependent [37, 38]. Furthermore, the possible presence of cracks and bubbles induced during growth is caused by the high vapour pressure of Sb. These geometrical defects may lead to a much higher value of the resistivity, without

affecting the results obtained by susceptibility or specific heat measurements.

Summarizing, these light rare earth compounds have a metallic behaviour and show important crystal field effects; the latter are investigated in detail by inelastic neutron scattering presented in chapter 5.

4.5 Resistivity in magnetic semiconductors

4.5.1 Results

In contrast to the light rare earth RNiSb compounds, those containing a heavy rare earth element are semiconductors having a small energy gap at the Fermi level.

Different samples were grown and their electrical transport properties were found to be very sensitive to the exact crystal stoichiometry, which is quite normal for ternary compounds with a vacancy in their crystal structure. This feature enabled to study the different conduction mechanisms occurring in these compounds, as these different mechanisms depend predominantly on the number and density of donor and acceptor levels in the particular sample. Since the magnetic, photoemission and diffraction measurements are not so sensitive to tiny variations in the number of defects in the crystal structure, no difference between different samples of the same compound could be detected in those measurements which are presented in the chapters 2.4, 3 and 6. Figure 4.7 shows the resistivity curves for some Tb-, Dy-, Ho- and LuNiSb samples. The resistivity ranges up to $8800 \mu Ohm cm$ for LuNiSb, $11000 \mu Ohm cm$ for DyNiSb, $65000 \mu Ohm cm$ for TbNiSb, and $200000 \mu Ohm cm$ for HoNiSb. In the range between 150 and 300 K, the resistivity drops with increasing temperature for all these compounds as expected for a semiconductor. Here, only in the HoNiSb and LuNiSb sample, the resistivity falls continuously with temperature over the whole temperature range indicating a high quality of the sample. In these TbNiSb and DyNiSb samples, the resistivity first increases with temperature, reaches a maximum at 150 K for TbNiSb and at 70 K for DyNiSb and falls again at higher temperatures as expected for a semiconductor. The resistivity for another - the most intrinsic - TbNiSb sample is shown in figure 4.8 in a linear scale, where the resistivity drops exponentially from a maximum of $700000 \mu Ohm cm$ over the whole temperature range, indicating a high quality of that sample. Note that at 3 and 5.5 K the resistivity law changes clearly resulting from a change in the direction of the magnetic moments and then from the appearance of

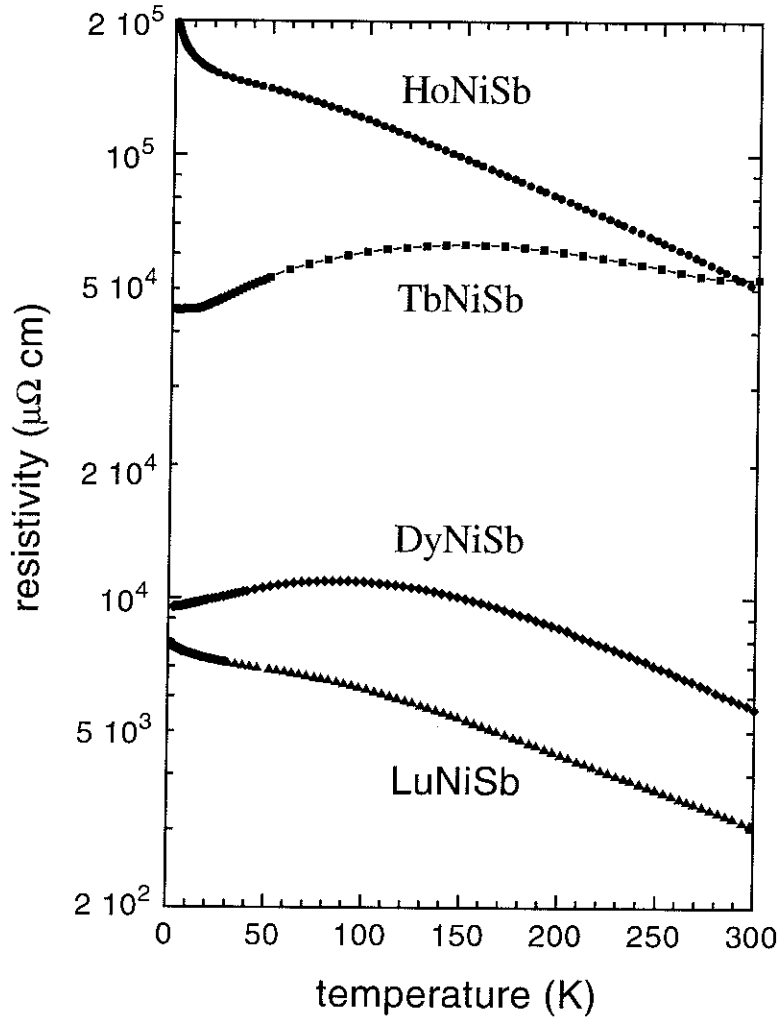


Figure 4.7: Electrical resistivity of some Tb-, Dy-, Ho- and LuNiSb samples in the temperature range between 1.5 to 300 K

a long range order at the Néel temperature, as will be determined by the crystal field analysis (chapter 5.5). The magnetic ordering points, extracted from our resistivity measurements, are in good agreement with magnetization and neutron scattering data, also for the other investigated compounds, as tabulated in table 3.1 on page 33.

YNiSb shows a resistivity rising with temperature, but the value of the resistivity is with $2000 \mu\Omega cm$ quite large for a metal; we suppose that it may be a semimetal. Dhar et al. [39] have reported a kind of semiconducting

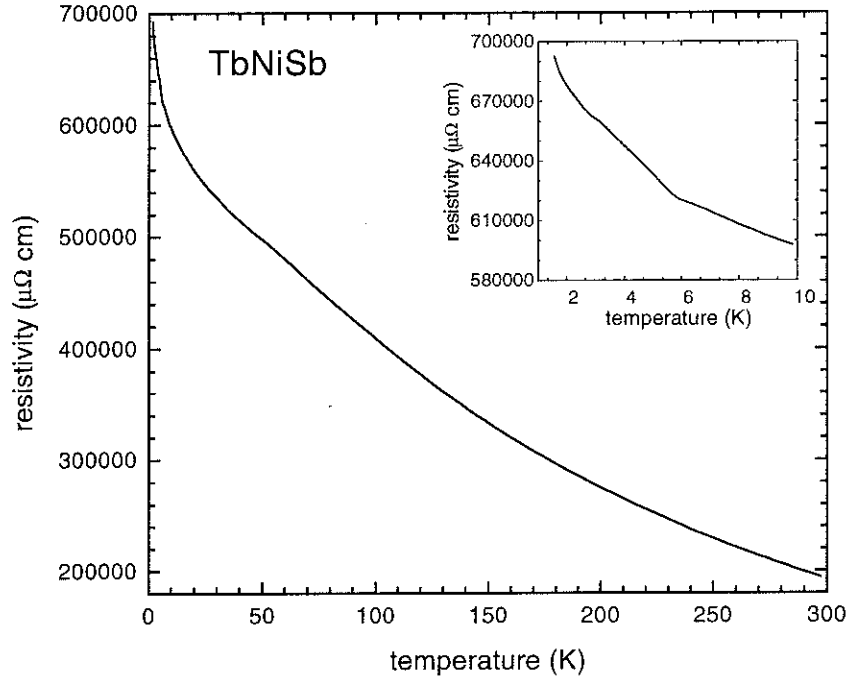


Figure 4.8: Electrical resistivity of TbNiSb, shown is here a sample with a very low extrinsic conduction. At low temperatures, the resistivity changes its slope due to variations in the magnetic scattering, explained on the basis of the crystal electric field, outlined in section 5.5

behaviour for LuNiSb although the absolute value of the resistivity with a maximum of $1900 \mu Ohm cm$ at 2 K is not large. Our measurements confirm a semiconducting behaviour with a resistivity reaching $8800 \mu Ohm cm$ at 2 K. At variance, a semi-metallic behaviour has been found for YbNiSb [39] with a resistivity of $R_{max} = 3600 \mu Ohm cm$ at 300 K.

4.5.2 Discussion

For an ideal semiconductor, the resistivity is at higher temperatures clearly dominated by the exponential term in equation (4.3): $\rho = \rho_0 * \exp(E_{gap} / (2k_B T))$. Plotting $\ln(\rho)$ over $1/T$ one can obtain from the resistivity curves the width of an energy gap at the Fermi level, being equal to 18 meV for TbNiSb, 24 meV for DyNiSb and 61 meV for HoNiSb. The fits were performed at higher temperatures between 250 and 300 K, in order to minimize the influence by hopping or impurity conduction which may dominate at low

temperatures; the values of the energy gap were found to be nearly constant between different samples of the same compound. Hence, although some other processes can rule the low temperature regime, at higher temperatures the thermal activation of charge carriers clearly dominates the conduction process, giving directly the magnitude of an energy gap around the Fermi level.

Assuming an ideal, impurity and defect free crystal structure, the electronic density of states was calculated for these samples, shown in figure 4.9 as described in chapter 6.3. They reveal a band gap at the Fermi level of 0.141, 0.185, 0.220 and 0.196 eV for TbNiSb, DyNiSb, HoNiSb and LuNiSb respectively, corresponding to activation energies of 1400 to 2200 K. These values are much larger than the experimentally determined ones and the resistivity, calculated with such bands gaps, would be much larger since only a small number of carriers could be thermally lifted to the conduction band according to the Boltzmann distribution. The experimental energy gap is indeed the energy difference between donor/acceptor levels (impurity states) situated within the true gap of an ideal semiconductor and the conduction or valence band respectively.

At low temperatures, impurity levels close to the Fermi-level play the crucial role. Depending on the number and density of these states, they either form an impurity band or quantum mechanical tunnelling ('hopping') between the localized states leads to the conduction process.

In the first case, like in TbNiSb and DyNiSb in figure 4.7, the initial growth of the resistivity at low temperatures looks like the one for a doped semiconductor in its extrinsic or impurity range, where the wrong stoichiometry, crystal defects, occupation of wrong sites lead to some amount of ionized donor or acceptor levels. The most frequent defects may be antiphase boundaries between domains corresponding to an inversion of the rare earth and Sb, as well as the wrong location of Ni on a vacant site. This is quite normal for ternary compounds with a vacant site, resulting in a metallic like contribution to the resistivity. This extrinsic, impurity conduction may dominate in the low temperature region where the intrinsic conduction is small, while at higher temperatures the number of thermally excited carriers increases exponentially, causing that the semiconductor like behaviour dominates the conduction process, although the intrinsic regime is probably not reached. Assuming that, as far as the conduction processes are concerned, the electrons of different bands do not interact with each other, the conductivity σ_{tot}

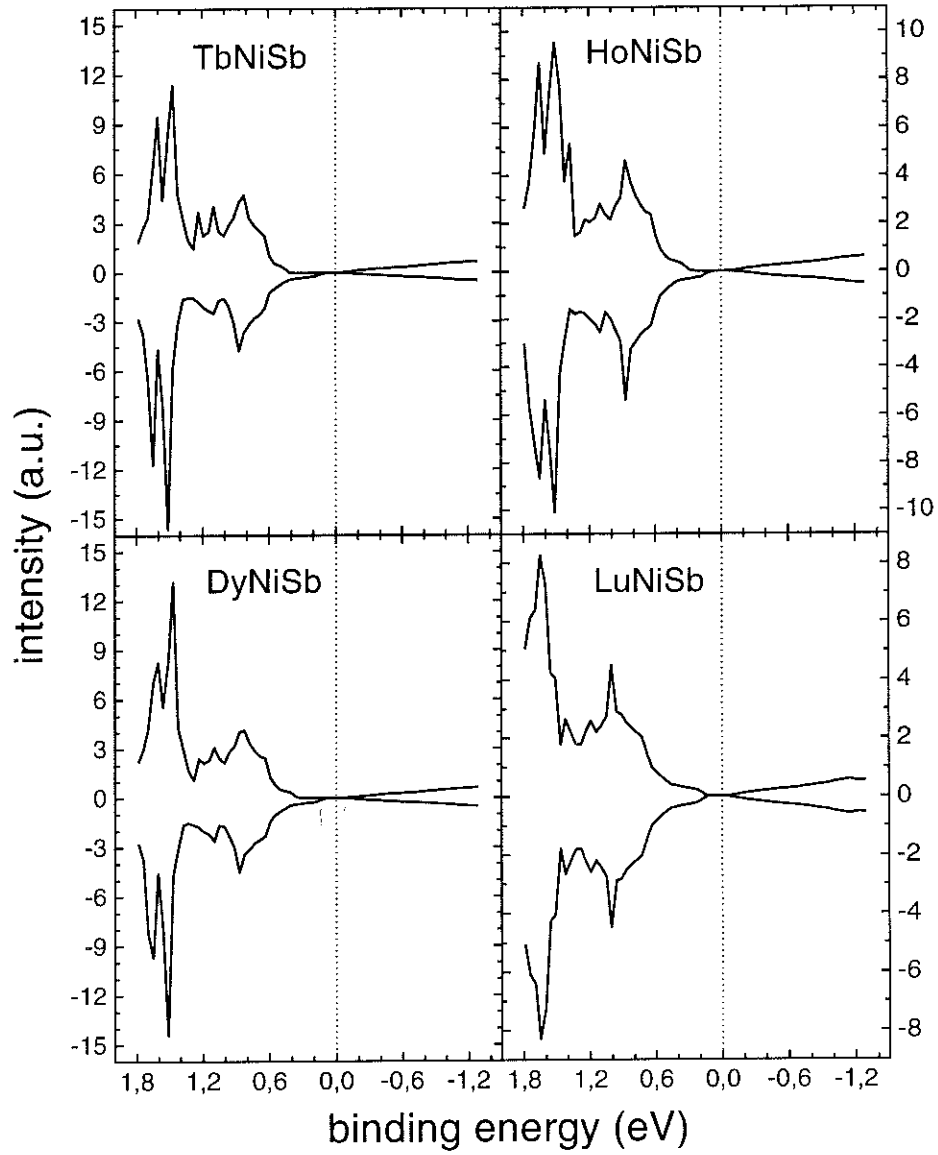


Figure 4.9: Calculated total electronic density of states of TbNiSb, DyNiSb, HoNiSb and LuNiSb for both spin directions (top and bottom curves) [111]. All these semiconductors reveal a narrow energy gap at the Fermi level as specified in the text.

is additive and may be analyzed by using an approach of mixed conduction

$$\sigma_{tot} = \sigma_{act} + \sigma_{imp} = a T^{\frac{3}{2}} e^{-\frac{d}{T}} + \frac{b}{(T+c)^2} . \quad (4.9)$$

Here, the first term characterizes the activation part, extracted from equation 4.3, where some charge carriers from impurity levels are thermally activated into a conduction band. The second term in equation 4.9 represents approximately the metallic conductivity at low temperatures. This metallic resistivity can be caused by a sufficiently high number of defects and impurities which then leads to the formation of an impurity band, to which the Fermi edge is pinned. A similar result would occur when - through the polarization of the 4f moments - former localized 'spin up' and 'spin down' levels are decoupled in such a way that the Fermi edge for the 'spin up' side approaches or increases above the mobility edge.

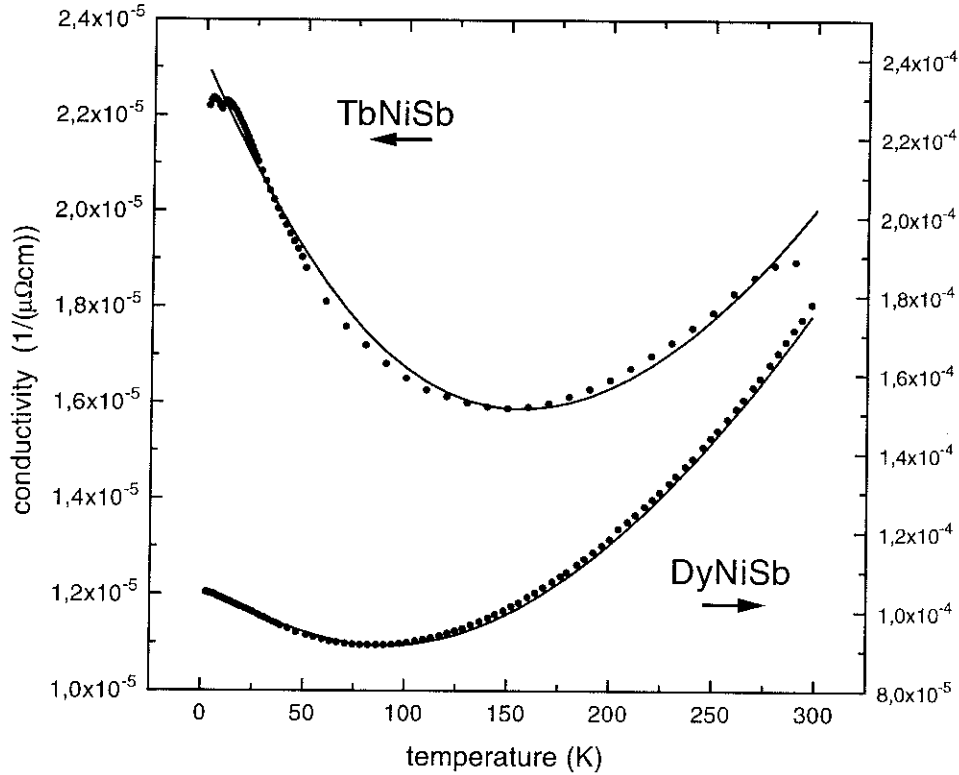


Figure 4.10: Fitting of the conductivity $\sigma = \frac{1}{\rho}$ of TbNiSb and DyNiSb over the whole temperature range according to equation 4.9, assuming a model of combined activated and impurity band conduction. See the text for details.

The good agreement of the fits, shown in figure 4.10, indicates that this approach characterizes well the processes in these semiconducting samples, containing a high number of donor/acceptor states and impurity levels within the gap. The number and density of these states is highly sample dependent and can be described by the fitting parameters b and c , in particular by the prefactor b . The prefactor a of the activation term also varies with the number of impurity states present, since from these levels the charge carriers are thermally activated into the conduction band. However, while the extrinsic term largely depends on the particular sample being investigated, the parameter d , describing the energy gap between impurity levels and the valence/conduction band, remains basically unaffected by the number of impurities present in different samples of the same compound. This indicates that physical properties other than the electrical conductivity may not be so sensitive to the exact density of impurity states, especially since only a small fraction of the total number of electrons contributes to the conduction process in these highly resistive compounds. Further, it shows that the same kind of defects exists in various compounds. However, tiny variations in the number of defects have an enormous effect on the electrical resistivity, since the involved states are situated exactly in that regime, which is close to the transition between weakly localized states and the beginning of conduction in an impurity band

A quite different situation occurs in the second case, which is found in those samples with a low number of donor/acceptor centres, where the Fermi level lies below the mobility edge, i.e. HoNiSb in figure 4.7 and TbNiSb in figure 4.8. The mean distance of their impurity states, situated within the energy gap, is sufficiently larger than the Bohr-radius so that the formation of a band cannot take place and the states remain localized. However, their wave functions still overlap and the charge carriers can jump in a quantum mechanical tunnelling process from one localized state to another, leading to the so called hopping conduction (figure 4.3). This is particularly important at low temperatures, while at higher temperatures the activated conduction hides this weak hopping effect. So, the conduction σ_{tot} in these samples may be described by an approach

$$\sigma_{tot} = \sigma_{act} e^{-\frac{E_a}{2k_B T}} + \sigma_l \left(e^{-\frac{T_0}{T}} \right)^{\frac{1}{4}} + \sigma_0 \quad (4.10)$$

where the first two terms describe the activated conduction and the hopping conduction in the variable hopping range (VRH) respectively. σ_0 is the residual conductivity, meaning that our samples are always on the conducting side of the metal-insulator diagram. Using this approach, the conductivity curves

have been fitted over the whole temperature range as shown in figure 4.11. The good agreement of the experimental data with the theoretical model

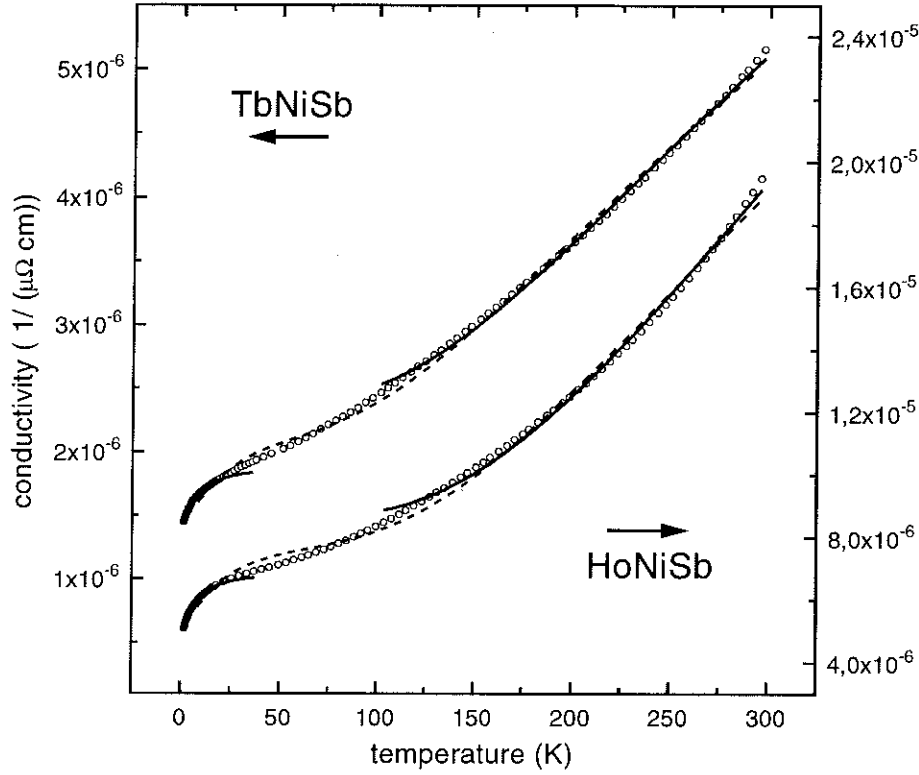


Figure 4.11: Conductivity $\sigma = 1/\rho$ of TbNiSb and HoNiSb. The experimental curves (open circles) are fitted according to equation 4.10 in the whole temperature range (dashed line) as well as at high and low temperatures (solid lines) for higher accuracy.

suggests that this approach is applicable to the present situation.

In the fits, all prefactors σ_{act} , σ_l as well as σ_0 were found to be larger for HoNiSb than for TbNiSb, scaling as the total conductivity. However, despite the quite different conductivities, the characteristic Mott temperature T_0 is found to be almost the same for both samples, 29 K for TbNiSb and 25 K for HoNiSb, leading to the conclusion that the hopping mechanism is of the same sort in both samples and probably also in the other heavy rare earth compounds, provided a very low number of impurities and defects.

Preliminary thermopower experiments have been performed at room temperature for 5 compounds; all show a negative Seebeck coefficient S , ranging

from -15 to $-48 \frac{\mu V}{K}$. The sign and magnitude are typical for electron-doped semiconductors.

Summarizing, the donor/acceptor states below the Fermi level rule the conduction processes which were identified and successfully deconvoluted by a theoretical model. It explains the experimentally determined width of the band gap, and the resistivity curves can successfully be simulated using this approach in samples containing a high as well as a low density of donor/acceptor states within the intrinsic band gap.

4.6 Giant magnetoresistance

The light rare earth RNiSb compounds reveal only a medium magnetoresistance reaching a maximum of $\frac{\Delta R}{R} = -13\%$ at 2 K under 5 Tesla for CeNiSb, $\frac{\Delta R}{R} = -18\%$ at 22 K under 4 Tesla for NdNiSb, attributed to spin disorder scattering, and a small positive magnetoresistance with a maximum of $+7\%$ at 2 K and 5 Tesla for PrNiSb. They show almost no magnetoresistance at high temperatures. In contrast, LaNiSb reveals a large positive magnetoresistance of $\frac{\Delta R}{R} = +20\%$ under 6.4 Tesla. This large value may be related to a semi-metallic state, the prototype of which is bismuth [112].

On the other side, the semiconducting compounds with the heavy rare earth metals reveal a larger negative magnetoresistance at low temperatures usually called 'giant magnetoresistance' (figures 4.12 and 4.13). At 2 K and under 5 Tesla it reaches values of up to $\frac{\Delta R}{R} = -31\%$ for TbNiSb, -32% for DyNiSb, and -27% for HoNiSb under 4 Tesla; under 8 Tesla, the magnetoresistance of TbNiSb reaches -50% . Conversely, the magnetoresistance of LuNiSb, which has a closed 4f shell, is weak and positive with $+1.5\%$ under 8 Tesla.

Two main origins may give rise to high negative magnetoresistance effects in semiconductors: The reduction in spin disorder scattering due to the alignment of moments under a field, and the reduction of the gap (or the localisation energy) arising from the splitting of the up- and down-spin subbands.

While applying an external magnetic field, the polarization of the 4f shell causes through the $JS_{4f} * s$ coupling with the valence electrons a polarization of the electrons around the Fermi-level. The energy bands for spin up and spin down move in different directions and thereby decrease the width of the energy gap at the Fermi-level, leading to a decreased electrical resistivity

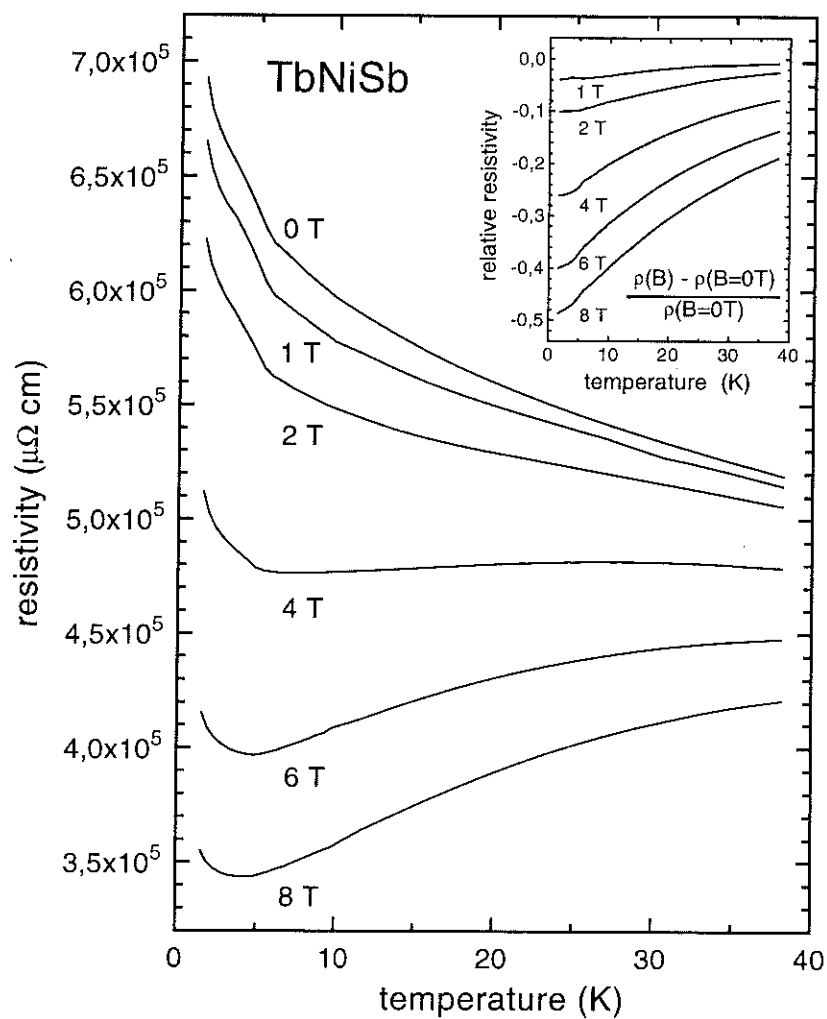


Figure 4.12: Magnetoresistance of TbNiSb

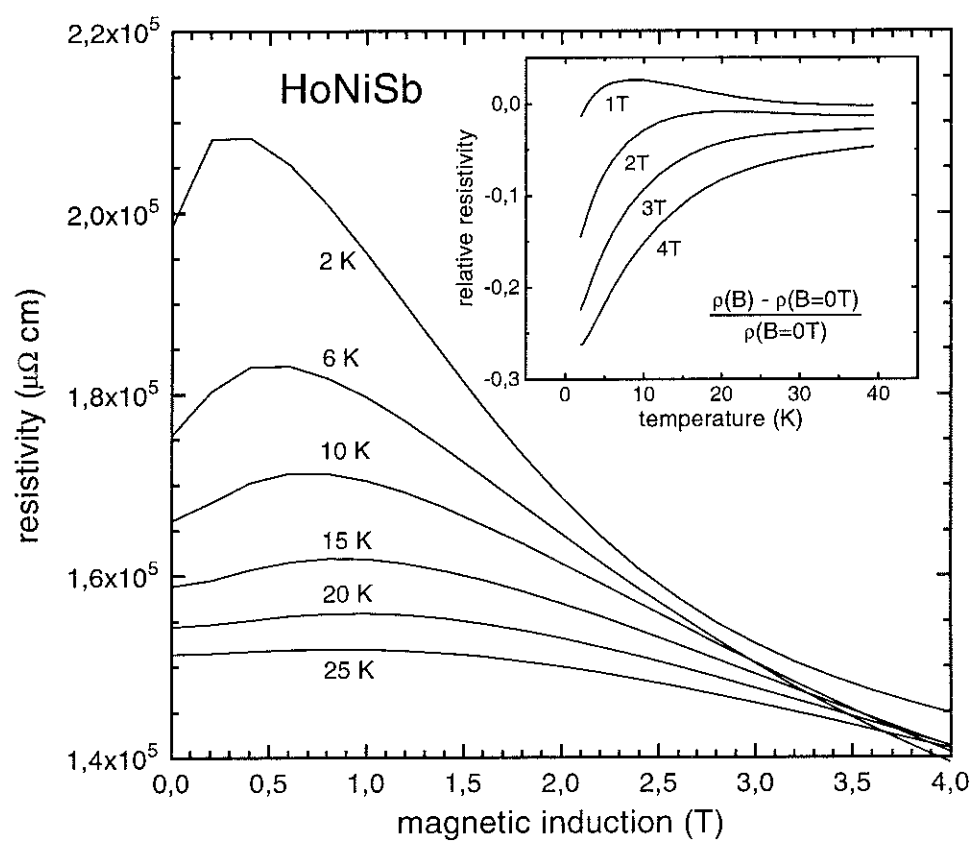


Figure 4.13: Magnetoresistance of HoNiSb

due to a higher number of thermally activated charge carriers. The variation of their mobility may also play a role. However, due to the large width of the gap of around 1400 to 2200 K the magnetic field has a negligible direct effect on the intrinsic gap of the semiconductor, or even on the activation energy of donor and acceptor centres. This is proved by the weak positive magnetoresistance in LuNiSb where no magnetic 4f shell is present, showing that the contribution to the narrowing of the gap is negligible. Hence, the negative magnetoresistance in these magnetic RE compounds arises predominantly from the reduction of spin disorder scattering, where the disorder scattering potential is reduced, thereby increasing the carrier mobility and the mean free path. This situation can be compared with some rare earth semiconducting oxides [93, 94] where the impurity bands within the large intrinsic energy gap shift under the influence of an external magnetic field in such a way that these bands are crossing, reducing the effective energy gap provoking thus a large negative magnetoresistance.

The magnetoresistance has been found to be more intense in those samples with a low density of charge carriers showing a more intrinsic behaviour, while those samples with a higher number of impurity levels reveal a less pronounced MR-effect. This has been explained recently [113] by the computation of the relaxation rate for a low density gas where $k_F a \ll 1$ (a is the lattice constant). The relaxation rate is related to the variation of the correlation length ξ and to the suppression of the magnetic fluctuations by an applied magnetic field. Then, it can be shown that the MR-coefficient $C \sim \frac{1}{k_F^2 a^2}$ for $k_F \xi \gg 1$ [113] (see also equation 4.8) is highly dependent on the carrier density. Hence, lower densities of carriers (small k_F) contributing to the conduction process can greatly enhance the MR without involving an insulator-metal transition in agreement with our measurements. The factor A is about $2 \cdot 10^{-2} \mu_B^{-2}$ in the purest samples, the normalized coefficient C is about 1, much lower than in Mn perovskites or pyrochlores (about 10). Our compounds are in the magnetic impurity regime [114] having localized and disordered magnetic moments without hybridization with current carriers.

According to De Gennes and Friedel [108] the spin disorder contribution (equation 4.7) is linked to the correlation function between spins, or more simply to the square of the magnetization. While neglecting crystal field effects, the magnetization $M(B, T)$ is given in the paramagnetic range by:

$$M(B, T) = M_0 B_J \left[\frac{M_0 B}{k_B (T - \theta_p)} \right] \quad (4.11)$$

where B_J is the Brillouin function, B the magnetic field and θ_p the paramagnetic Curie-Weiss temperature. The experimental curves $\rho(B)$ at a constant

temperature can be fitted to the theoretical formulae 4.7 and 4.11, showing that this model of spin disorder scattering characterizes well the magnetoresistance processes in these compounds. For example, the fit of DyNiSb, shown in figure 4.14, gives a moment of $8.3 \mu_B$ for Dy, slightly lower than the value obtained by susceptibility measurements and the theoretical one for a free Dy ion. This slight reduction may be justified by crystal field effects below 40 K. The value of $\theta_p = -15 K$ obtained from this fit is close to that deduced from susceptibility. At low temperatures, the resistivity of HoNiSb

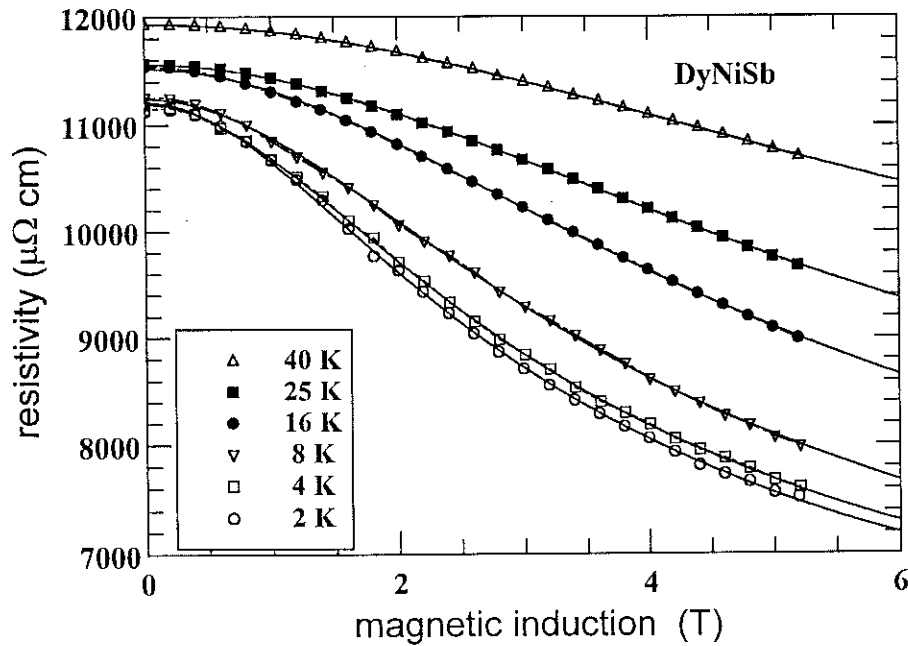


Figure 4.14: Magnetoresistance of DyNiSb, experimental curves (dots), and theoretical fit according to equation 4.7 and 4.11 (full curves)

first increases slightly when a magnetic field is applied, reaching a maximum of $\frac{\Delta R}{R} = +10\%$ at 0.5 T before the resistivity decreases again in a stronger magnetic field giving a large negative magnetoresistance of -27% at 4 T. Besides the negative contribution of the magnetoresistance, many origins can explain the initial positive magnetoresistance. This initial increase may be explained by several processes: Firstly, it may be related to a metamagnetic process below T_N , but this explanation does not hold in the paramagnetic range. Secondly, it may be due to a cyclotron effect where electrons precess around in the magnetic field thereby increasing the resistivity; but this contribution should dominate at high magnetic fields. Further, a localisation of

charge carriers may take place where, due to random scattering, electrons migrate on a closed path in the applied magnetic field, remain weakly localized and increase the resistivity. This may be significant in this case as this HoNiSb sample is more intrinsic than some of the investigated compounds. Another possible explanation might lie in the band structure: It is possible that a shift of some impurity energy levels may occur when a small external magnetic field is applied, modifying then the number of carriers as well as their mobility. This explanation has been invoked to explain the initial positive magnetoresistance of EuSe [97]. In addition, the anisotropy of the magnetoresistance due to the electric quadrupole moment of the rare earth may also play a role.

4.7 Conclusion

The investigation of the electrical transport properties allowed to gain detailed insight into the electronic structure and the states in the region around the Fermi level and allowed, in connection with the extensive use of theoretical models, to identify the complex mechanisms ruling the conduction and the giant magnetoresistance.

The light rare earth compounds show a metallic behaviour with a low density of states at the Fermi level in agreement with the results obtained by X-ray photoemission measurements. This behaviour might arise from a semimetallic band structure as observed in several other semi Heusler compounds. Moreover the results show important crystal field effects and suggest a Kondo influence for CeNiSb as will be proved later by inelastic neutron diffraction.

On the other hand, a transition towards narrow gap semiconductors occurs in the heavy rare earth RNiSb compounds, principally due to the transformation in the crystal structure, explained in section 2.3. Several theoretical models were employed to simulate the conduction regimes in samples with different numbers of impurity states, which finally allowed, in combination with important information provided by band structure calculations, to separate and identify the complex overlapping conduction processes. In this way, the conduction mechanism in these narrow gap semiconductors was identified to be ruled by the donor and acceptor levels within the energy gap, inducing a conduction process either within a narrow impurity band or by hopping conduction between localized states. As the resistivity is very sensitive in this regime, this method can be employed as a very sensitive technique

to determine the number and density of impurities, donor and acceptor levels in these or similar kinds of compounds.

A giant negative magnetoresistance effect was discovered, reaching a value of -50% under 8 Tesla in the heavy rare earth compounds provoked by the special properties of the internal magnetic 4f shell, which are analysed in the chapters 3 and 6. By studying and employing theoretical models, the GMR mechanism was identified to be governed by the reduction of the spin disorder scattering, which is opposite to the situation of some rare earth oxides where the GMR mechanism is dominated by the shift and the crossing of some impurity bands. However, in both cases, the GMR takes place involving impurity bands and the intensity/amplitude of the MR was found to depend on the number of available charge carriers.

Chapter 5

Crystalline Electric Field

5.1 Introduction

When a magnetic ion forms part of a crystal lattice, the energetic degeneracy of its spin-orbit levels is lifted by interactions with the surrounding electrostatic field - called *crystalline electric field* (CEF) or more simply *crystal field* -, due to neighbouring atoms, ligands and conduction electrons. As in rare earth compounds the full 5s and 5p shells screen these interactions, the crystal field can generally be considered as a small perturbation of the free ion 4f levels, in contrast to the case of 3d metals with a less localized magnetic shell. Hence, the crystalline electric field effects can be treated as a perturbation on the appropriate free-ion wave function. The CEF energy levels can then be calculated by finding the perturbing Hamiltonian operator and its matrix elements as known from standard perturbation theory. The theory of crystal fields originates from the work of Bethe in 1929 and a number of review articles have appeared which deal with the description of the crystal fields in rare earth systems e.g. [115, 116]. The CEF is the origin of several physical properties such as magnetocrystalline anisotropy, magnetostriiction and is thus of major importance for applications e.g. permanent magnets or perpendicular recording. Most often the crystal field parameters are determined with the help of inelastic neutron scattering [48, 51, 117].

5.2 Theory

On the basis of a simple point charge ionic model, the perturbing Hamiltonian operator

$$\mathcal{H}_{CEF} = -|e| \sum_i V(\vec{r}_i) \quad (5.1)$$

can be calculated by a summation over all magnetic electrons i whereas the potential V is developed in spherical harmonics $Y_n^m(\theta, \phi)$ $V(|r|) = \sum_{l,m} \gamma_{lm} r^l Y_n^m(\theta, \phi)$.

The matrix elements of the CEF Hamiltonian between the states of a given multiplet can be obtained by direct integration [118] where the free ion wave functions are expanded into products of single electron wave functions:

$$\int \Phi^*(r_i, \theta_i, \phi_i) r^n Y_n^m(r_i, \theta_i, \phi_i) \Phi(r_i, \theta_i, \phi_i) d\vec{r}_i \quad (5.2)$$

As the radial part is the same for all 4f electrons and is furthermore never accurately known, it is often taken as a parameter [119]:

$$\langle r^n \rangle = \int [R_{4f}(r_i)]^2 r_i^n r^2 dr \quad (5.3)$$

Stevens [120] has developed an *operator equivalent* method, which enables to calculate in a much more simple manner the matrix elements of the crystalline potential between coupled wave functions specified by one particular value of angular momentum J . By introducing new operators J_+, J_-, J_z, J the former summation of polynomes depending on x_i, y_i, z_i or r_i, θ_i, ϕ_i is transformed into a set of new functions $O_n^m(J, J_z, J_+, J_-)$, called operator equivalents, which possess exactly the same symmetry properties. The exact convention for this transformation is given in e.g. [115]. For instance, in the simple case of the second order, $3z^2 - r^2$ is transformed to $3J_z^2 - J(J+1)$ where the operator J corresponds to the total angular momentum [121].

This finally leads to the Hamiltonian operator describing the energy of the crystalline electric field

$$\mathcal{H}_{CEF} = \sum_{mn} A_n^m \langle r^n \rangle \theta_n O_n^m(J, J_z, J_+, J_-) \equiv \sum_{mn} B_n^m O_n^m(J, J_z, J_+, J_-) \quad (5.4)$$

where the reduced matrix elements θ_n , called Stevens coefficients, are usually labelled as α_J, β_J and γ_J for terms of the second, fourth and sixth degree respectively. The crystal field parameters $A_n^m \langle r^n \rangle$ are sometimes contracted

with the Stevens coefficients in order to obtain a shorter notation $B_n^m \equiv A_n^m \langle r^n \rangle \theta_n$; many particular functions as well as the corresponding Stevens coefficients are tabulated in [115].

The group theory has a great importance on the crystal electric field analysis, especially because it can eliminate some of the possible terms depending on the point group symmetry and on the finite value of the orbital angular momentum of the individual magnetic electrons. So, only operators up to the sixth degree need to be considered for terms composed of f-electron wave functions, while for 3d-metals ionic configurations and Ce^{3+} the terms up to the fourth degree are sufficient.

A quite simple situation occurs in high symmetry cubic crystals, where in the case of rare earth ions only the fourth and sixth order terms $O_4 \equiv (O_4^0 + 5 O_4^4)$ and $O_6 \equiv (O_6^0 + 5 O_6^4)$ contribute to the crystalline electric field. Following the transformation of Lea, Leask, Wolf (LLW) [122]

$$\begin{aligned} B_4 F_4 &= Wx \\ B_6 F_6 &= W(1 - |x|) \end{aligned} \quad (5.5)$$

where $-1 < x < 1$ and F_4, F_6 are factors common to all matrix elements, the Hamiltonian rewrites as

$$\mathcal{H}_{CEF} = W \left[x \frac{O_4}{F_4} + (1 - |x|) \frac{O_6}{F_6} \right] . \quad (5.6)$$

Hence, the crystal field is fully described by two newly introduced independent parameters, the energy scale factor W and parameter x specifying the ratio between the fourth and sixth order crystal field term. In this way, the energy levels, corresponding to the different irreducible representations Γ_i for a specific J , can be described as a function of x and may be plotted as shown in figure 5.1.

In lower symmetry systems, more independent parameters may be needed to characterize the crystal field as tabulated for example in table 5.1 [123]. In these cases, a simple two dimensional graphical representation of the crystal field splitting is no longer possible like in cubic systems using the LLW-transformation. However, the exact energy levels of the crystal field can be calculated employing the above described Stevens operator equivalent method, and the experimental inelastic neutron scattering spectra can be simulated by taking into account the intensities of a particular transition [124]. The calculated and experimental spectra are then compared in order to determine the CEF-parameters of the investigated sample. Since in some

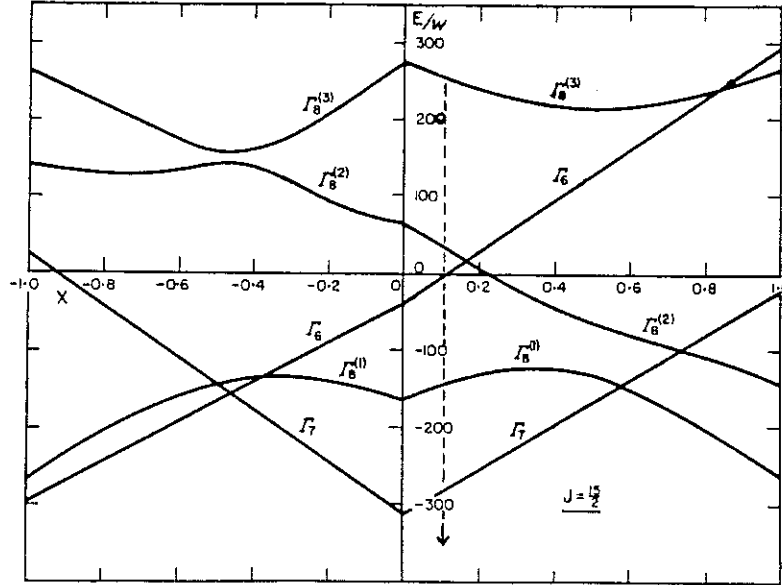


Figure 5.1: Splitting of the energy levels for $J = \frac{15}{2}$, (Er^{3+} , Dy^{3+}) in a cubic crystal field [122]. The dashed arrow assigns the CEF levels for $ErNiSb$ with $x^{Er} = 0.104$ and $W^{Er} = -0.417$ as determined later (table 5.3 on page 82) and drawn in figure 5.8 on page 83.

point group	symmetry	CEF-parameters	number of independent CEF-parameters	examples
D_{3d}	trigonal	$B_2^0, B_4^0, B_4^3, B_6^0, B_6^3, B_6^6$	6	$CeNiSb^*$, $PrNiSb$, $NdNiSb$
T_d	cubic	$[B_4^0, B_4^4], [B_6^0, B_6^4]$	2	$TbNiSb$, $DyNiSb$, $HoNiSb$, $ErNiSb$
* only 3 CEF-parameters have an influence for Ce-compounds				

Table 5.1: CEF-parameters of some points groups, extracted from [123]

low symmetry systems the number of independent CEF-parameters may exceed the information given by inelastic neutron scattering experiments, other known physical data must be taken into account in order to resolve the unique set of CEF-parameters.

The energy splitting of the crystal field levels lies usually in the order of a few meV, which is in the range of thermal excitations, compared to the spin orbit splitting situated in the range of eV. As a result, the thermal population and the transitions between the CEF levels rule many physical properties. In this way, the magnetic susceptibility, specific heat, the magnetic contribution to the resistivity and other physical properties can be calculated when the set of CEF parameters is known which characterizes a particular compound. Some of these relations will later be analysed in the discussion.

5.3 Experimental

The most straightforward method to determine experimentally the crystal electric field levels is to measure the energy transfer induced by inelastic neutron scattering. Monochromatic neutrons are scattered by the magnetic ions and thereby may induce a transition between two CEF levels $|m\rangle$ and $|n\rangle$ while losing the corresponding energy $\hbar\omega$. When limiting to transitions within a given J-multiplet and considering only small momentum transfers, the neutron scattering cross section $\frac{d^2\sigma}{d\Omega d\omega}$ simplifies for an assemblage of N non-interacting ions to [124]

$$\frac{d^2\sigma}{d\Omega d\omega} = N \left(\frac{1.91e^2}{2mc^2} g_J \right)^2 f^2(\vec{Q}) \frac{k_f}{k_i} \sum_{mn} \rho_n |\langle n | J_\perp | m \rangle|^2 \delta(E_m - E_n - \hbar\omega) \quad (5.7)$$

where ρ_n is the Boltzmann factor, J_\perp describes the component of \vec{J} perpendicular to the scattering vector \vec{Q} . $f(\vec{Q})$ represents the magnetic form factor of the ion and k_i , k_f stand for the wavevectors of the incident and scattered neutrons respectively.

These measurements were performed at the cold neutron multichopper spectrometer IN5 at the Institute Laue Langevin (ILL) in Grenoble, France [82], sketched in figure 5.2. Cold mono-energetic neutrons with an incident wavelength $\lambda_0 = 2.5\text{\AA}$, $E_0 = 13.2\text{meV}$ or $\lambda_0 = 5.0\text{\AA}$, $E_0 = 3.3\text{meV}$ were scattered inelastically in order to study low-energy transfer processes as a function of the momentum transfer at different temperatures. The resolution at full width half maximum (FWHM) was $100\mu\text{eV}$ and $900\mu\text{eV}$ at a wavelength of 5.0\AA and 2.5\AA respectively.

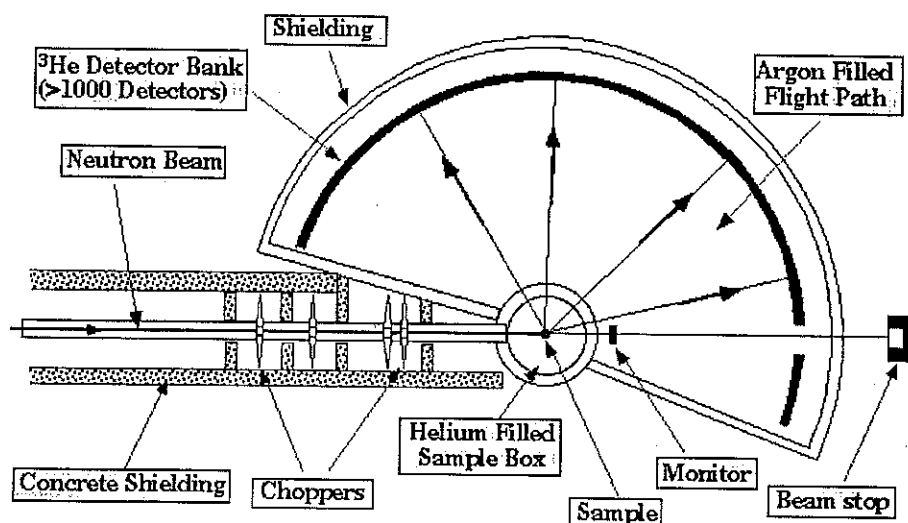


Figure 5.2: IN5 is a general purpose time of flight (TOF) spectrometer. Four accurately phased disk-choppers produce a mono-energetic cold neutron beam impinging on the sample. The energy of the scattered neutrons is then measured by time of flight, detected by the detector bank with more than 1000 individual ^3He detector tubes. The figure is reproduced from [82].

The spectral energy distribution of powdered RNiSb samples was determined by inelastic neutron scattering, summing up only the low angle detectors in order to minimize the contribution by phonon scattering which increases quadratically with the scattering angle. To extract the pure magnetic scattering of the investigated sample, the background scattering from the empty sample holder was subtracted from the measured total response.

These corrected spectra were then compared with theoretical simulations produced by a computer program using the Stevens operator equivalent method [115, 120] in order to determine the crystal electric field parameters which characterize the compounds.

5.4 Results

5.4.1 Excited levels and crystal field in heavy rare earth compounds

Inelastic neutron scattering measurements were performed on seven RNiSb compounds with $R=\{\text{Ce,Pr,Nd,Tb,Dy,Ho,Er}\}$ as well as on $\text{Y}_{0.9}\text{Er}_{0.1}\text{NiSb}$, where a small amount of the magnetic Er was diluted in paramagnetic YNiSb. Measurements were performed at temperatures below and above the magnetic ordering points, as well as at a higher temperature around 80 to 100 K, where higher crystal field levels are already thermally populated. Two different energies of the incident neutrons were used, $\lambda_N = 2.5\text{\AA}$ and at low temperatures also $\lambda_N = 5.0\text{\AA}$ to take advantage of its higher energy resolution. Some of the spectra are given in the figures 5.3 to 5.5 together with the corresponding simulations.

Figures 5.3 and 5.4 show the evolution of the ErNiSb energy transfer spectra with temperature. Since at low temperatures only the ground state is populated, only upwards transitions arising from this state may occur, yielding a less complex spectrum with a minimum number of possible transitions; for instance, ErNiSb exhibits at 4 K only two strong excitations at 7.9 and 9.3 meV (figure 5.3). The peak appearing at 2.8 meV in the 4 K spectrum is most probably a spurious peak, as it does not appear in the (Er,Y) diluted solution. The simulations were performed assuming a gaussian line shape; the linewidth taken in the fits were 0.5 and 0.35 meV for the quasielastic and inelastic lines respectively. The variation of the spectrometer resolution with the energy was not taken into account.

In contrast, at higher temperatures, higher crystal field levels become populated, leading to possible additional excitations of electrons originating from these levels. This is seen as two additional energy transfer peaks at 4.9 and 6.3 meV in the ErNiSb spectrum at a temperature of 80 K (figure 5.4). Furthermore, at these higher temperatures, the deexcitations of electrons, which already populate higher energy levels, become sufficiently intense, leading to negative energy transfer peaks, possibly enabling the detection of high energy transitions exceeding the energy of the incident neutrons.

The derived CEF parameters are listed for the heavy RNiSb compounds in table 5.3 with the corresponding energy diagrams in figure 5.8. The low temperature spectrum obtained for HoNiSb is shown in figure 5.5 together with the CEF fit. The crystal field parameters found for Ho and Er are coherent. In the case of TbNiSb (figure 5.6), the 10 K spectrum contains a low

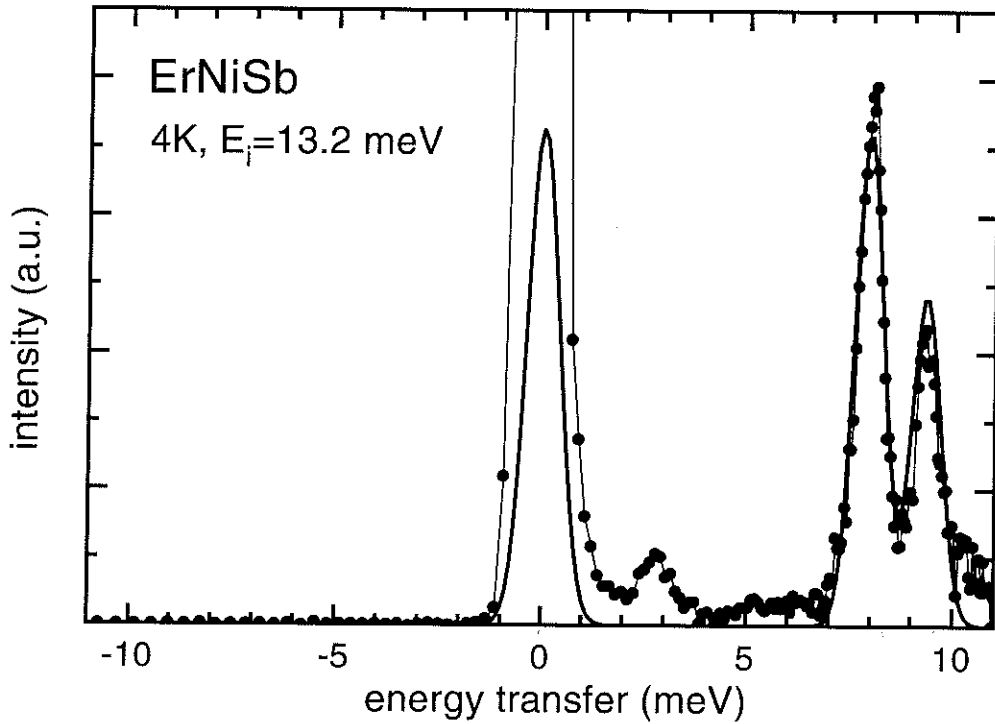


Figure 5.3: Inelastic Neutron diffraction of ErNiSb at 4 Kelvin. The comparison between the experimental curve (dotted line) and the theoretical simulation (straight line) enables to determine the CEF parameters: $W^{Er} = -0.417K$ and $x^{Er} = 0.104$.

energy excitation around 1.5 meV, an intense and composite line around 5.1 meV and a possible faint excitation near 8.5 meV. Two solutions may account for the spectra, one corresponding to $W = 0.6K$, $x = 0.38$, the second to $W = 0.44K$, $x = -0.26$. The second one gives crystal field parameters consistent with those for Ho and Er.

Due to the large incoherent scattering length and the high absorption coefficient of Dy $\sigma_a(Dy) = 535$ barns [125], only poor quality spectra with a low signal to noise ratio could be obtained for DyNiSb, preventing a reliable determination of the CEF-parameters for this compound. A tentative set, coherent with the previous ones, may be $W = -0.40 K$, $x = -0.25$.

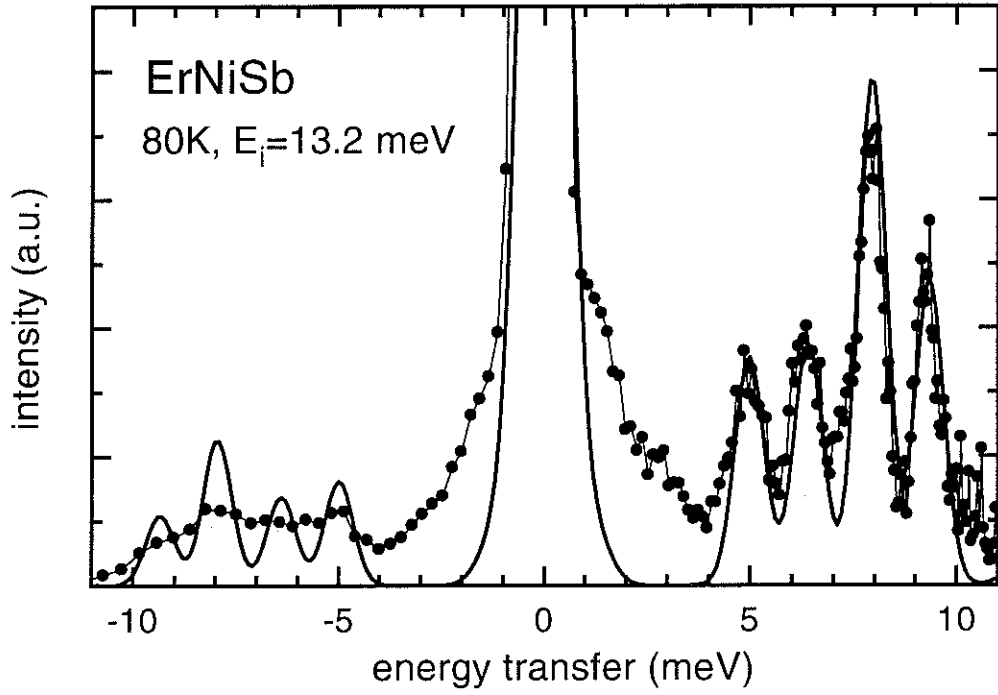


Figure 5.4: Inelastic Neutron diffraction of ErNiSb at 80 Kelvin. The comparison between the experimental curve (dotted line) and the theoretical simulation (straight line) enables to determine the CEF parameters: $W^{Er} = -0.417K$ and $x^{Er} = 0.104$.

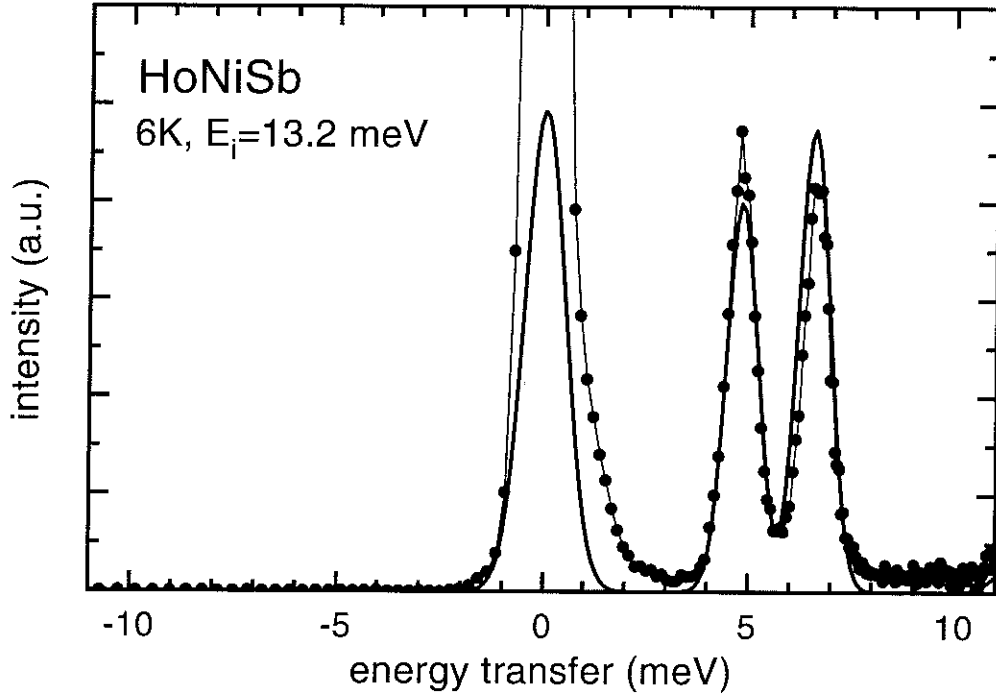


Figure 5.5: Inelastic Neutron diffraction of HoNiSb at 6 Kelvin. The comparison between the experimental data (dotted line) and the theoretical simulation (straight line) enables to determine the CEF parameters: $W^{Ho} = 0.274K$ and $x^{Ho} = 0.052$.

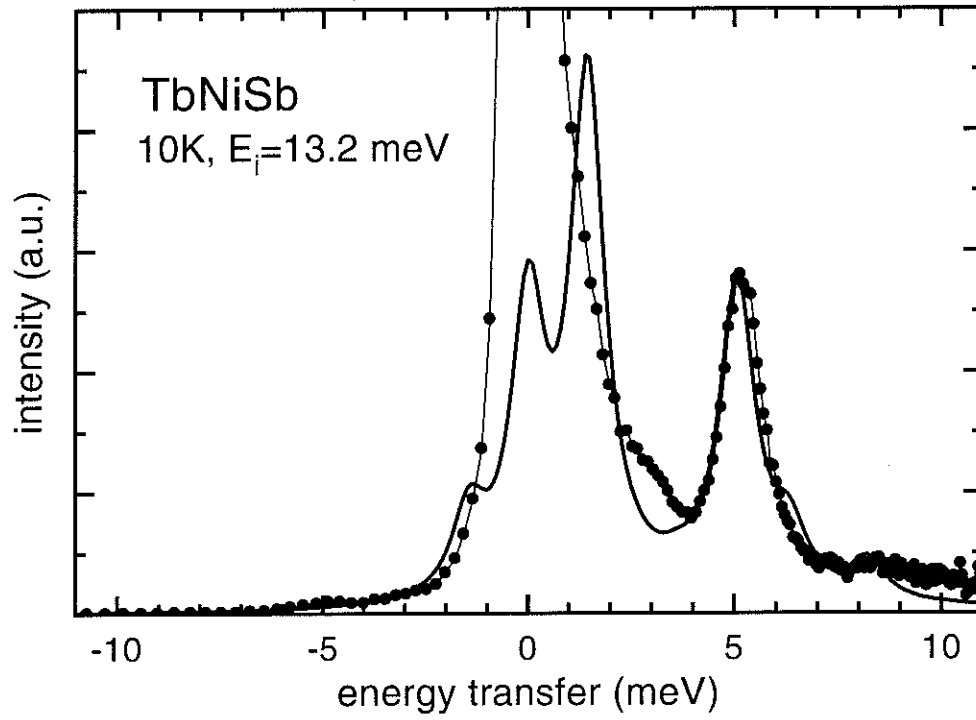


Figure 5.6: Inelastic Neutron diffraction of TbNiSb at 10 Kelvin. The comparison between the experimental curve (dotted line) and the theoretical simulation (straight line) leads to a possible set of CEF parameters $W^{Tb} = 0.44K$ and $x^{Tb} = -0.26$ as used in this fit. Another possible set of parameters could be $W^{Tb} = 0.6K$ and $x^{Tb} = 0.38$.

5.4.2 Excited levels and excitations in the ground state for light rare earth compounds

The spectra of CeNiSb taken with an incident energy of 13.2 meV ($\lambda_N = 2.5\text{\AA}$) show an inelastic excitation located at 10.2 meV, which is also seen at 100 K in the deexcitation process. Some additional intensity also appears at 100 K in the range of 5-6 meV.

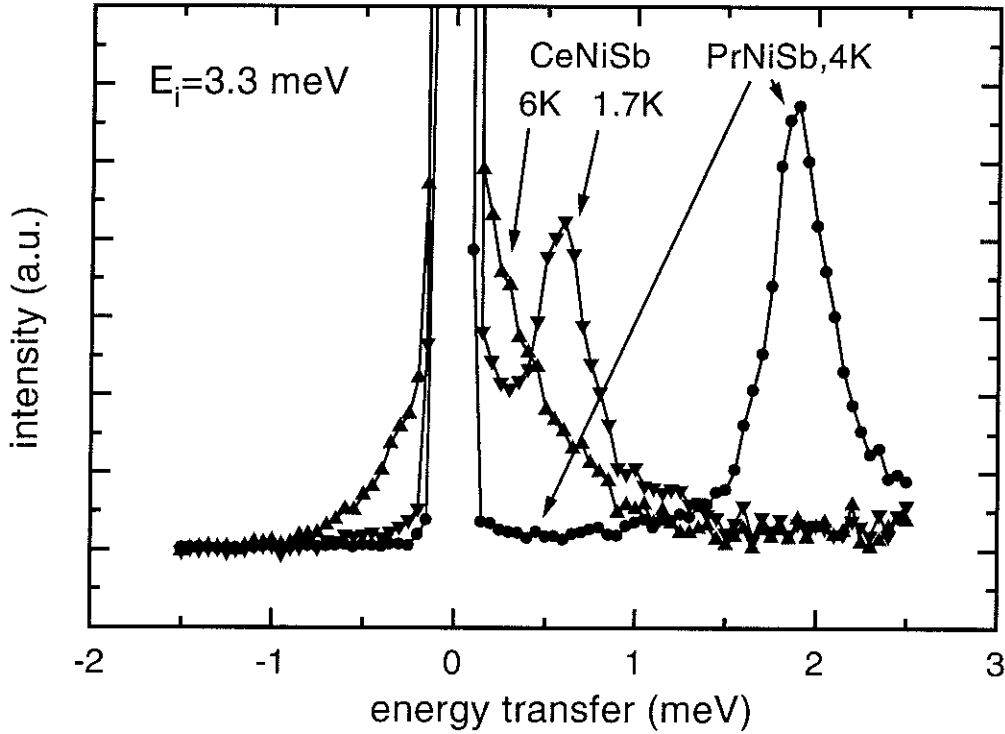


Figure 5.7: Inelastic neutron scattering spectra with $\lambda_N = 5\text{\AA}$ ($E_i = 3.3\text{ meV}$) of CeNiSb at 1.7 K (down triangle), at 6 K (up triangle) and of PrNiSb (circle) at 4 K.

The features at lower energies were examined with a higher energy resolution using an incident energy of 3.3 meV ($\lambda_N = 5.0\text{\AA}$). Figure 5.7 compares the low energy transfer region of CeNiSb and PrNiSb, showing that CeNiSb has a broad, pronounced quasielastic peak due to transitions within the degenerate ground state. The residual width at 6 K is 0.5 meV suggesting a Kondo temperature of about 8 K. Indeed another contribution to the width may arise from exchange interactions, as CeNiSb orders near 4 K with a complex magnetic structure. The quasielastic line observed in the param-

agnetic range transforms at 1.7 K into an inelastic and dispersive magnon branch. The present $|q|$ spectrum samples a part of this dispersion curve, giving a mean density of magnon states which depends on the q -range and the q -resolution.

PrNiSb does not reveal any quasielastic line at low temperatures (below 4 K). Three upwards excitations are located at 1.9, 2.9 and 10.7 meV and no change is observed down to 1.8 K, which means that there is no magnetic order down to this temperature. Thus, the ground state is not magnetic, which is confirmed by the absence of any magnetic order recorded by susceptibility or resistivity measurements. The inelastic structures are broadened at 40 K and some shoulders related to the energy differences between levels are observed. The observed data are not sufficient to solve the crystal field level scheme.

The spectrum of NdNiSb taken at 30 K in the paramagnetic range shows, in addition to a quasielastic line, two excitations located near 3.4 and 5.6 meV; the two corresponding downwards transitions are also present on the deexcitation side of the spectrum. At 100 K, the 5.6 meV line is broadened, a transition appears near 2 meV on both excitation and deexcitation sides, which is probably a transition between the two above-mentioned excited levels; a fourth transition is located at about 10.5 meV on the deexcitation side. Thus, at least four doublets are located at 0, 3.4, 5.6 and probably 10.5 meV. In the spectrum taken at 2 K, the two first transitions of the 30 K spectrum are split into four components due to the magnetic order separated by about 2 meV thus indicating a magnetic coupling strength of this order of magnitude.

As a rough summary, the experimentally determined peak positions of all compounds are given in table 5.2, where also the origin for the particular transitions is given. However, fine details are not specified here, such as peak shapes or the development of new transitions with temperature. A more detailed analysis of some interesting features is given in the following discussion.

5.5 Discussion

5.5.1 Heavy rare earth compounds

In the cubic RNiSb compounds only the fourth and sixth order CEF terms can contribute to the crystal electric field. Hence, the simulation and analysis

Compound	Peak positions in meV
ErNiSb	0.48, 4.9 ⁺ , 6.3 ⁺ , 7.9*, 9.3*
Er _{0.1} Y _{0.9} NiSb	0.48, 4.9 ⁺ , 6.3 ⁺ , 7.9*, 9.3*
HoNiSb	0.26 ^m , 4.8*, 6.6*, (9.9), 11.8*
DyNiSb	3.3
TbNiSb	1.5* , 2.8 ⁺ , 5.1*, 8.5 *
NdNiSb	2.2 ⁺ , 3.4*, 5.6*, 10.5
PrNiSb	1.9*, 2.9*, (7.0), 10.7*
CeNiSb	0.57 ^m , 6.5 ⁺ , 10.2*
^m magnon in the ordered range	
* excitations from the ground state	
+ excitations between excited states	

Table 5.2: Measured energy transfer peak positions in the paramagnetic state of RNiSb compounds; see the text for details.

allows to determine directly the two independent crystal electric field parameters, which are shown in table 5.3 following the notation of LLW [122] as given in the equations 5.5 and 5.6.

Compound	W(K)	x	$A_4\langle r^4 \rangle$ (K)	$A_6\langle r^6 \rangle$ (K)
ErNiSb	-0.417	0.104	-16	-13
Er _{0.1} Y _{0.9} NiSb	-0.417	0.104	-16	-13
HoNiSb	0.274	0.052	- 7	-14
DyNiSb	(-0.40)	(-0.25)	(-28)	(-10)
TbNiSb	0.44	-0.26	-16	-38

Table 5.3: CEF-parameter for heavy RNiSb compounds

With the set of CEF parameters and some known characteristics of the rare earth ion, the energy and wavefunction of each level can be calculated employing the Stevens operator equivalent method. This then leads to the energy level scheme as shown for ErNiSb in figure 5.8; the energy difference between these levels correspond to the neutron scattering energy transfer peaks as marked inside the graphic.

It is often useful to dilute the magnetic ion into a diamagnetic matrix to further reduce the magnetic interactions and so to obtain clear and sharp lines [126]. As a test, 10% of Er was diluted in YNiSb (Y_{0.9}Er_{0.1}NiSb) leading -as expected- to the same crystal field parameters as in ErNiSb. Since the

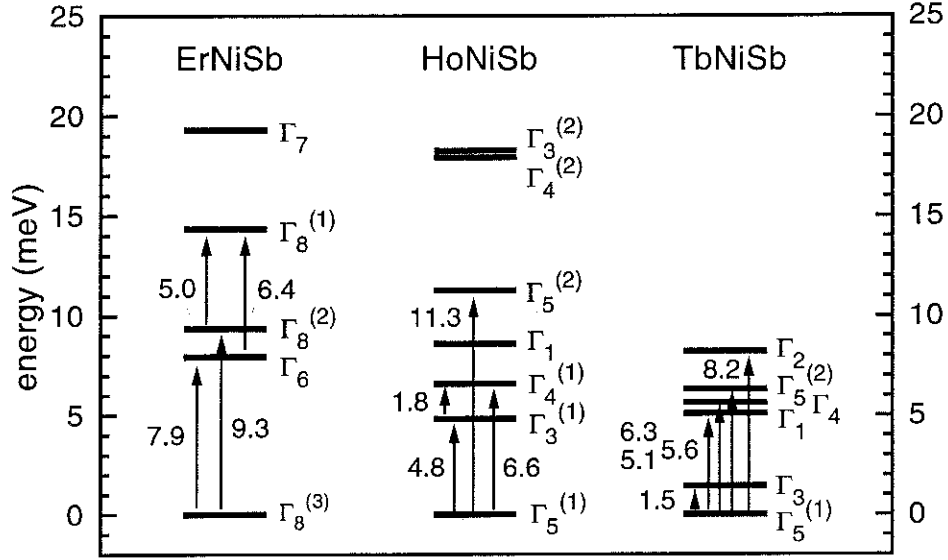


Figure 5.8: CEF energy level diagram for ErNiSb, HoNiSb and TbNiSb. The composition of the energy levels (the irreducible representations Γ) is tabulated in LLW [122]

heavy RNiSb compounds are semiconducting with weak interactions between the magnetic atoms, the peaks are relatively sharp and narrow; the observed linewidths are even weaker in the diluted $\text{Y}_{0.9}\text{Er}_{0.1}\text{NiSb}$, since the magnetic interactions are further reduced. Contrarily, the magnitude of magnetic interactions is larger for TbNiSb, where broader lines are observed.

In all these RNiSb compounds the sixth order CEF parameters are stronger than the fourth order ones; especially in Ho- and ErNiSb, the sixth order term is clearly dominating. As the size of the Tb ion is larger than those of Ho and Er, the electronic surrounding of Tb is slightly modified, thereby shifting the CEF parameters in these RNiSb compounds. The relative order of magnitude of B_4 and B_6 is opposite to the one in cubic RSb compounds, which have a similar crystal structure, constructed by omitting the Ni atom in cubic RNiSb. In the RSb compounds, the fourth order term plays the dominant role, shown as $x^{\text{HoSb}} = 0.904$ and $x^{\text{ErSb}} = 0.891$ or 0.78 [86]. This shows that the electronic charges of the nickel atoms modify the surrounding of the rare earth atoms in such a way that in RNiSb the sixth order terms dominate over the fourth order ones in the development of the crystal electric field.

On the basis of the known sets of CEF-parameters it is now possible

to analyse the direction of the magnetic moments in these antiferromagnetic structures, which were directly measured with elastic neutron diffraction (chapter 3.5). In Ho and Tb, the sixth order Stevens coefficient γ_J is negative, favouring a binary axis direction at low temperatures due to the large and negative $A_6\langle r^6 \rangle$ CEF parameter. In contrast, Er and Dy have a positive coefficient γ_J , the direction of the magnetic moments is rather ruled by the sign of the $A_4\langle r^4 \rangle$ parameter, supporting a (100) magnetization axis if this parameter is negative. Calculating the magnetic moments μ at low temperatures on the basis of the determined CEF-parameters shows that in HoNiSb and TbNiSb the magnetic moments are aligned along a binary axis $\vec{\mu} \parallel (110)$ with $|\mu^{Ho}(1.5K)| = 4.98\mu_B$ and $|\mu^{Tb}(1.5K)| = 6.19\mu_B$, while in ErNiSb and probably also DyNiSb the moments are orientated along (100) with $|\mu^{Er}(0K)| = 6.20\mu_B$ at 0 K. The calculated magnetic moments do also agree qualitatively with the elastic neutron diffraction results given earlier in table 3.1 on page 33.

Studying the orientation of the magnetic moments with temperature enables to understand more closely the origin of the macroscopic properties and it explains some features observed with other characterisation techniques. For TbNiSb, these CEF-calculations reveal that at very low temperatures the magnetic moment is oriented along a binary crystal axis in agreement with elastic neutron scattering. As the 6th order anisotropy falls more rapidly with increasing temperature than the 4th order one, a moment rotation towards a (100) axis may be expected, which should happen below the Néel temperature. This rotation of the magnetic moments may cause some variation in the magnetic scattering of conduction electrons resulting in a deviation from the ideal exponential resistivity curve of a semiconductor. A weak anomaly is observed around 3 K as shown in figure 5.9. Although hardly visible, it may correspond to such a rotation. Conversely, the anomaly at 5.5 K corresponds to the Néel temperature. Below about 3 K, the sample would be antiferromagnetic with the moments directed along a binary crystal axis ($\vec{\mu} \parallel (110)$), whereas between 3 K and 5.5 K, the moments would be aligned along a primary crystal axis ($\vec{\mu} \parallel (100)$). The two CEF solutions invoked in the paragraph 3.1 lead to very close free energy along (001) and (110) axes, allowing this moment rotation.

In these heavy rare earth compounds, the 4f shell lies relatively deep and well localized in the atom, being hence coupled more weakly with the states at the Fermi level in comparison to the light rare earth compounds where a strong 4f density of states approaches close to the Fermi level leading to a stronger hybridisation between the involved atomic shells [127]. Furthermore, the intrinsic density of charge carriers is quite low in these semiconducting

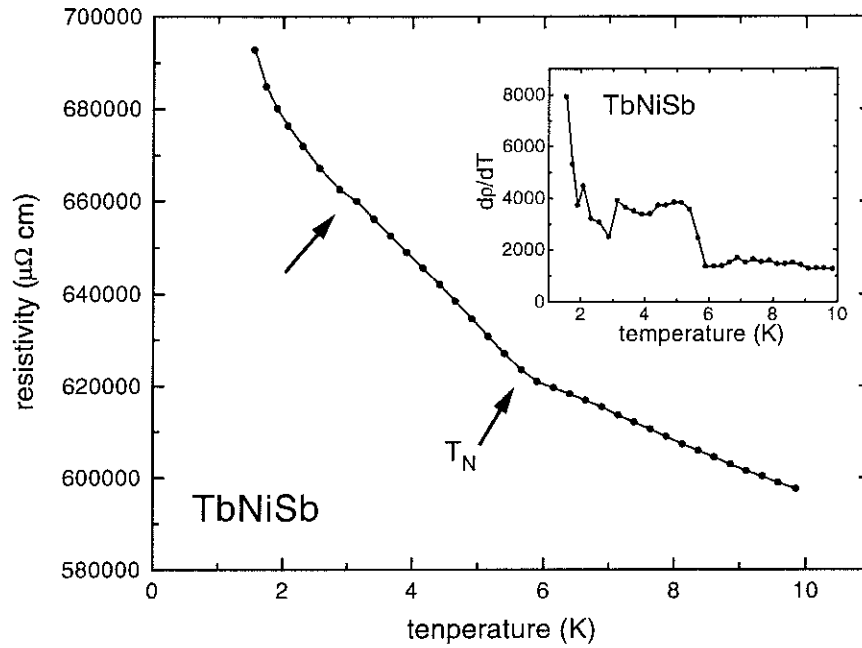


Figure 5.9: Resistivity ρ and its temperature derivative $\frac{d\rho}{dT}$ of TbNiSb , showing the changes in the magnetic ordering at about 3 and 5.5 K.

samples below room temperature, thus the conduction processes are dominated by the extrinsic semiconductor conduction. For these reasons, only weak influences of the CEF-field on the resistivity are observed in these heavy rare earth RNiSb compounds. Nevertheless, some influence may be present on the large magneto-resistance through the variation of the paramagnetic susceptibility.

The case is completely different for the light rare earth compounds, which are metallic and present a strong density of 4f states closer to the Fermi level. Hence a stronger coupling between the conduction and 4f electrons occurs, which results in an important influence of the CEF on the resistivity. This effect will be analysed in detail for the case of CeNiSb in the following paragraph.

5.5.2 Light rare earth compounds

In contrast to the cubic compounds, the crystal level schemes could not be completely resolved in the hexagonal compounds, as the high energy transfer data are not available because of the limited energy range of the cold neutron

spectrometer. The incomplete set of data complicates the analysis for the hexagonal compounds where 3 or 6 CEF parameters may contribute in the case of CeNiSb and PrNiSb / NdNiSb respectively. This requires to take other known properties of these compounds into consideration and to calculate their influence due to the CEF-scheme in order to obtain some additional information which may be used as further side conditions to determine the CEF level energy scheme.

For CeNiSb, the inelastic neutron diffraction data reveal a broad quasielastic peak at low temperatures (figure 5.7) indicating that the ground state is formed by the $|\pm 1/2\rangle$ level, because only this configuration has a significant matrix element of J_+ and J_- between the sublevels forming the ground state. Since a weak intensity at roughly 5-6 meV appears only at high temperatures, it suggests that this represents a transition to the $|\pm 5/2\rangle$ levels, which can be excited when the $|\pm 3/2\rangle$ level is already thermally populated. A direct transition from a pure $|\pm 1/2\rangle$ ground state to a pure $|\pm 5/2\rangle$ level is forbidden by the selection rules; in fact, it is not strictly forbidden in the present case as the B_4^3 term mixes $|\pm 1/2\rangle$ and $|\mp 5/2\rangle$, but the matrix element should be weak. Furthermore, the CEF-scheme must give the correct description of the observed macroscopic properties, in particular of magnetic resistivity as is discussed in the following. Taking into account these considerations, the simulations lead to the tentative set of CEF-parameters $B_2^0 = 4.1 \pm 1.5K$, $B_4^0 = -0.31 \pm 0.04K$ and $B_4^3 = 0 \pm 2K$ with a certain range of possible solutions, due to the poor statistics of neutron scattering data. Although the crystal field splittings are about two times smaller than those found in CePtSb and CePdSb, the CEF parameters B_2^0 and B_4^0 keep the same sign in all these similar compounds [51, 54].

On the basis of the determined CEF-parameters it is now possible to calculate the contribution of the magnetic scattering to the total resistivity of CeNiSb. Subtracting the resistivity of LaNiSb from that of CeNiSb, the magnetic resistivity in CeNiSb is obtained, since the resistivity of LaNiSb represents to a good approximation the phonon contribution, as discussed in chapter 4.4. In order to eliminate the temperature independent residual resistivity ρ_0 , which depends on the particular sample, the temperature derivative is taken to compare the experimental graph with the calculated curve. Figure 5.10 shows the experimental derivative of the magnetic resistivity $\frac{d}{dT}\rho_m^{CeNiSb} = \frac{d}{dT}[\rho^{CeNiSb} - \rho^{LaNiSb}]$ compared with the derivative of the theoretical resistivity curve. The latter was calculated taking into account the influence of the Kondo effect following the theory of Cornut-Coqblin [128]

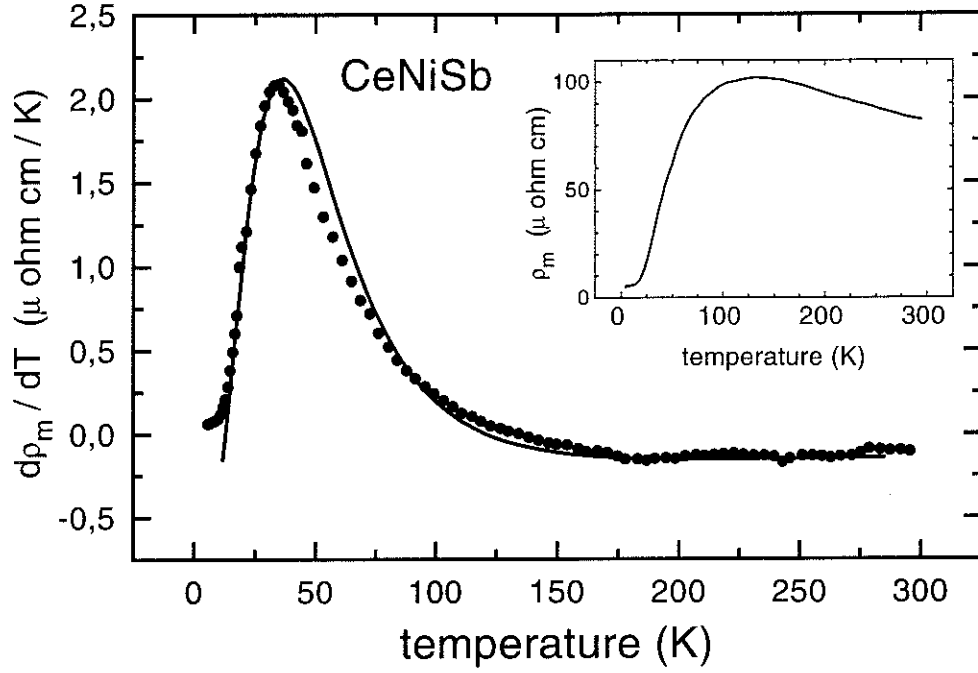


Figure 5.10: Derivative of the magnetic resistivity of CeNiSb. Experimental curve (dotted line) and calculation on the basis of the CEF-parameters $B_2^0 = 4.1K$, $B_4^0 = -0.31K$, $B_4^3 = 0K$ taking into account the Kondo effect (see text). The inset gives the magnetic resistivity of CeNiSb $\frac{d}{dT}\rho_m^{CeNiSb} = \frac{d}{dT}[\rho^{CeNiSb} - \rho^{LaNiSb}]$

using the equation

$$\rho_m = \Re \left(v^2 + \frac{\lambda_n^2 - 1}{(2j+1)\lambda_n} J^2 \right) \left[\frac{1 + 2n(E_F)\lambda_n J \ln \frac{kT}{D^{(n)}}}{\left(1 + \frac{v^2 (2j+1)\lambda_n}{J^2 (\lambda_n^2 - 1)} \right)} \right] \quad (5.8)$$

where v is the spin independent Coulomb scattering, J the s-f coupling j the quantum number and D a cut off energy related to the band width; the set of CeNiSb CEF parameters allows to calculate exactly the second order term as well as the degeneracy $\lambda_n(T)$.

It turns out that it is essential to include the influence of the Kondo effect in the calculation since a first attempt to apply the pure CEF-resistivity model without Kondo effect gave a significant discrepancy between the slopes of the experimental and calculated curves at high temperatures. The CEF + Kondo-fit gave the Kondo parameter $J n(E_F) = -0.04$. On the other hand,

the Kondo temperature (around 8 K) was determined from the broadening of the $|\pm 1/2\rangle$ ground state which is about 0.5 meV.

The good agreement indicates that the found CEF-scheme is correct, that there is an overall crystal field splitting of about 100 K, and that the Kondo effect plays an important role in CeNiSb, which has already been assumed from the shape of the resistivity curve (figure 4.6, [42]) and is also expected from spectroscopy measurements [129, 130].

The CEF also controls the macroscopic magnetic properties of the compounds. Following the theoretical approach of van Vleck, the susceptibility can be calculated according to equation 5.9 [131, 132]:

$$\chi_{CEF,\parallel} = N\mu_B^2 g_J^2 \sum_i p_i \left(\frac{|\langle i | J_{\parallel} | i \rangle|^2}{k_B T} + 2 \sum_{i \neq j} \frac{|\langle j | J_{\parallel} | i \rangle|^2}{E_j - E_i} \right) \quad (5.9)$$

where J_{\parallel} is the momentum parallel to the field. The calculated susceptibility is strongly anisotropic at low temperatures, unfortunately, no single crystals are available up to now and the susceptibility data on a polycrystal are not very selective. In agreement with the experiment, the reciprocal susceptibility calculated for a powder shows a downwards curvature below 30 K.

The resulting calculated susceptibility curve agrees quite well (negative curvature of $1/\chi$), apart from a scaling factor, with the experimental measurements described in section 3.4. Figure 5.11 compares the measured susceptibility with the calculated one $\chi = \chi_{Ce}^{CEF} + \chi_{Pauli}$ where the small constant Pauli susceptibility arises from a small temperature independent contribution from Ni 3d states. The magnitude of the ordered moment could not be determined from magnetisation or neutron diffraction for CeNiSb, but it is obviously smaller than the free ion value $g_J J = 2.14\mu_B$. One reason for this is the CEF effect, an other is the reduction of the moments by the Kondo effect.

In PrNiSb and NdNiSb, six independent parameters determine the crystal electric field. Due to the B_4^3 and B_6^3 terms, the CEF levels for PrNiSb have a composition like:

$$\begin{aligned} \alpha|3\rangle + \beta|0\rangle \pm \alpha|-3\rangle & \quad (\text{three singlets}) \\ \alpha'|\pm 4\rangle + \beta'|\pm 2\rangle + \gamma'|\mp 1\rangle & \quad (\text{three doublets}) \end{aligned} \quad (5.10)$$

All transitions between different levels are allowed, giving rise to the observed excitations at low temperature. The ground state is obviously a non magnetic

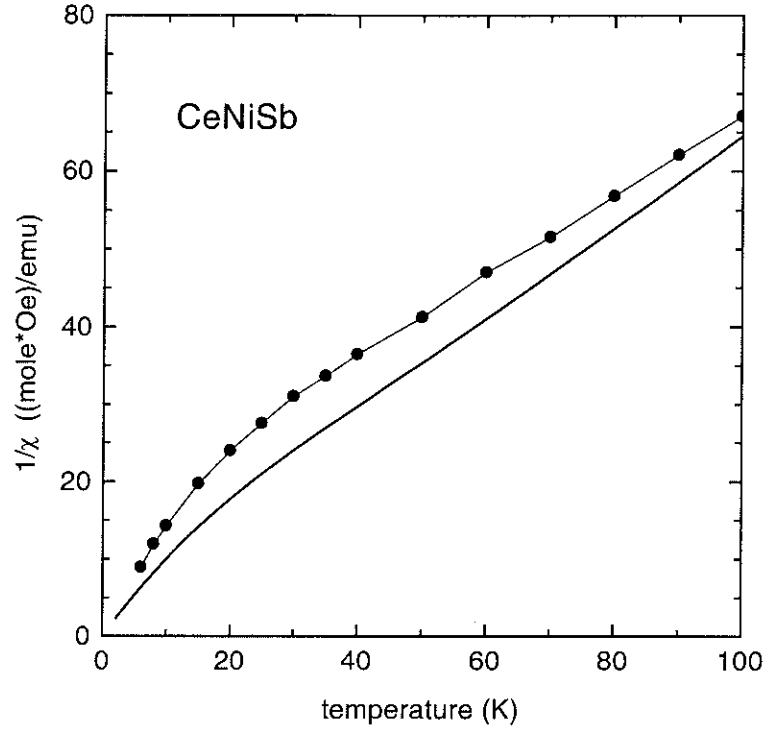


Figure 5.11: Inverse susceptibility of CeNiSb. Experimental (dotted line) and calculated (smooth line) curve which has been calculated on the basis of the CEF-parameters $B_2^0 = 4.1K$, $B_4^0 = -0.31K$, $B_4^3 = 0K$ assuming a small additional Pauli susceptibility.

singlet. However, additional data need to be considered, in order to put up further restrictions limiting the amount of possible solutions. As the magnetic resistivity ρ_m is a function of magnetic disorder, measured by the entropy S_m , its derivative $\frac{\partial \rho_m}{\partial T}$ is similar to the specific heat $C_m = \frac{\partial S}{\partial T}$ and can therefore be taken into consideration for checking the location of excited levels through the occurrence of Schottky-like anomalies.

In figure 5.12, the temperature derivative of the resistivity is shown and compared qualitatively with an energy spectra of PrNiSb, since both reflect the influence of the crystal field with increasing temperature or energy. Both, PrNiSb and NdNiSb show a pronounced Schottky anomaly visible as the broad peak around 50 K, which is related to the increasing population of crystal field levels lying around 10 meV. The feature at 10 K for PrNiSb is also a Schottky anomaly related to the population of the excited CEF levels visible through the strong neutron energy transfer peaks around 2-3 meV.

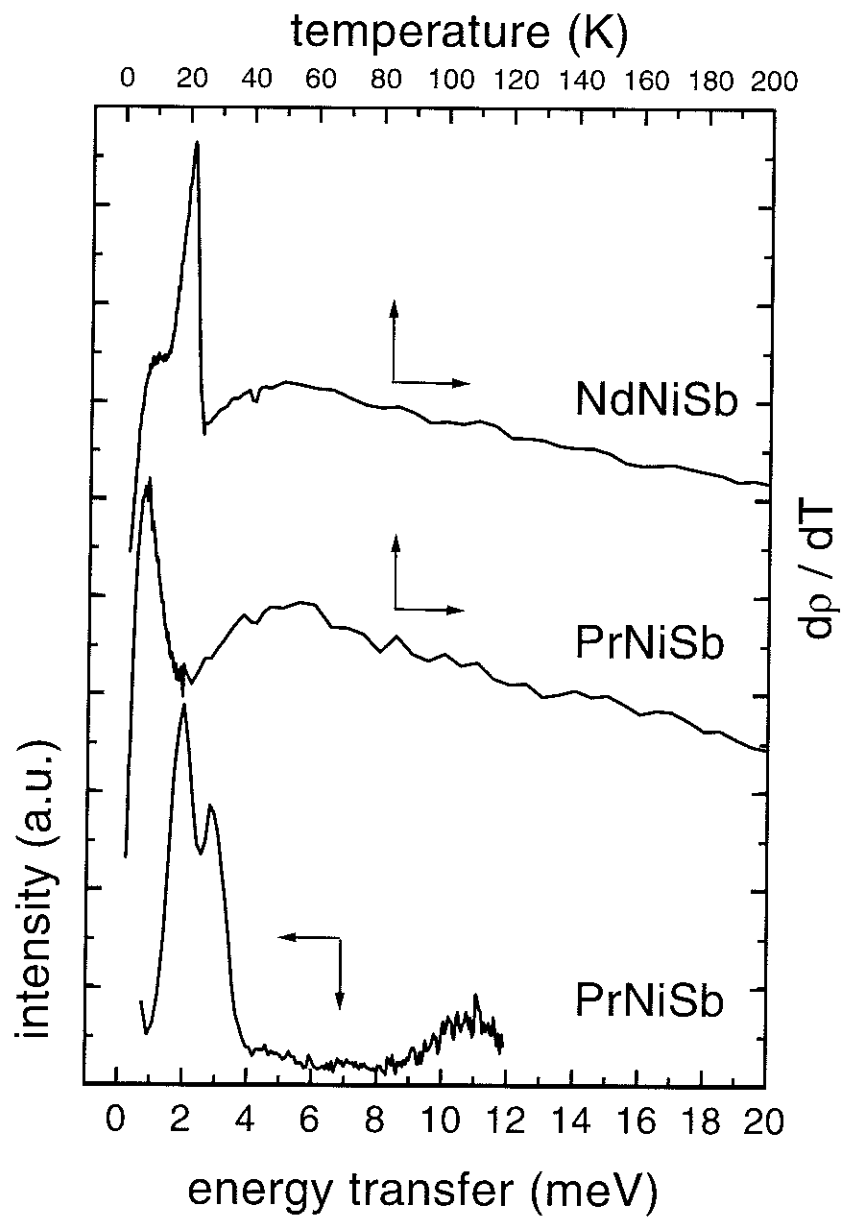


Figure 5.12: Temperature derivative of the electrical resistivity of PrNiSb and NdNiSb compared with an inelastic neutron diffraction spectra of PrNiSb at 4 Kelvin.

Conversely, the sharp and unsymmetrical peak observed at 23 K for NdNiSb is a λ -type anomaly related to the ferromagnetic order at T_C . However, the limited set of experimental data is not sufficient for determining the six independent CEF parameters in PrNiSb and NdNiSb. This might be possible with additional data, for instance from measurements of the susceptibilities $\chi_{||}$ and χ_{\perp} as well as from inelastic neutron scattering data at higher energies.

5.6 Conclusion

Inelastic neutron scattering measurements allowed to determine completely the crystal electric scheme of four compounds despite of the limited available energy range of the data. Apart from being interesting in its own right, the CEF-levels form the basis of many physical processes and thus play a crucial role in the understanding and interpretation of many macroscopically observable properties and effects. For example, the direction and the rotation of the magnetic moments could be explained, in agreement with the resistivity and magnetic measurements. Furthermore, the non magnetic behaviour of PrNiSb was explained and the Kondo temperature in CeNiSb was determined.

Chapter 6

Photoemission

6.1 Introduction

The electronic structure lies at the basis of any system, since it controls most of the physical properties and effects. Thus, extensive experimental and theoretical research is focussed on the investigation of the composition and nature of the energy levels, their wavefunctions and the electronic structure of these many electron systems. Photoelectron spectroscopy (PES) techniques enable to investigate a wide range of electronic properties, including the energy position of the electronic states, the localised or delocalised nature of the energy bands and the valence configurations close to the Fermi level which are ruling the electrical transport properties. Further, these PES characterisation methods are important as a complementary tool to provide detailed information linked to the understanding of the magnetic properties [133], such as band width, band dispersions, exchange interactions, effective intra-atomic Coulomb correlations, many body effects and the size and orientation of spin and orbital or total moments. Much of this information is only accessible by the means of electron spectroscopy, which is particularly true for surface effects, since the disruption of delicate electronic balance at the surface can lead to distinctive new properties [134, 135, 136, 137].

Starting with the discovery of the photoelectric effect [138, 139], several different photoelectron spectroscopy techniques have emerged during the last century [140, 141] leading to a large amount of research on various aspects on the electronic structure, also in the field of rare earths (RE), RE thin films, RE binary and ternary compounds, e.g. [142, 143, 136, 144].

Using tunable synchrotron radiation as an excitation source, the dramatic

enhancement of the shallow core level intensities of rare earths has been explored since the late 1970's [145], where the interferences between different excitation and decay channels leads to a (giant) resonant enhancement of the photoemission cross section. This resonant photoemission and photoabsorption has been investigated intensively in RE atoms [146, 147], RE thin films [148, 149, 150] as well as in RE compounds [151] at the $5p \rightarrow 5d$ [152, 153, 154, 155], $3d \rightarrow 4f$ [156, 157, 158] and at $4d \rightarrow 4f$ [159] photothreshold in search for a closer understanding of the details in excitation processes, to clarify the decay mechanisms and to study the interactions between the atomic shells involved. As the resonant photoemission process is specific of element and angular momentum, it has also gained practical importance as a tool to determine the nature of electronic states in rare earth systems and has helped to assign charge transfer satellites [153, 160, 161]. For the same reason, this technique can practically be applied as a very sensitive tool to detect accurately tiny amounts of impurities on surfaces, provided that the impurities in request are sensitive to a resonant enhancement of the photoemission spectrum at certain incident energies [162].

6.2 Theory

6.2.1 Photoemission

Photoelectron spectroscopy is a powerful surface sensitive characterisation technique providing information about the electronic structure of the top-most atomic layers associated with the short mean free path of the emitted photoelectron [163, 164]. The principle of photoelectron spectroscopy (PES, called UPS in the ultraviolet region ($<100\text{ eV}$) and XPS in the X-ray one ($1200\text{--}1500\text{ eV}$)) is to expose a sample to a beam of monoenergetic photons, which then interacts with the N electrons of the system, leading to a subsequent photoemission of electrons. They are then analysed in terms of kinetic energy, maybe additionally in spin and/or angle. The collected spectrum represents the probability distribution of energy gains of the system left after a particular process, carrying information on the occupied density of states (DOS). Figure 6.1 sketches - in the single particle approximation - this PES mechanisms together with three neighbouring spectroscopic techniques - XAS, XES and AES - illustrating here just the principle; a more detailed description can be found in e.g. [165, 166, 167]. In the case of angle resolved photoemission [144], the \vec{k} dependence can be measured from well ordered surfaces, allowing so to map the bandstructure [168, 169, 170, 171].

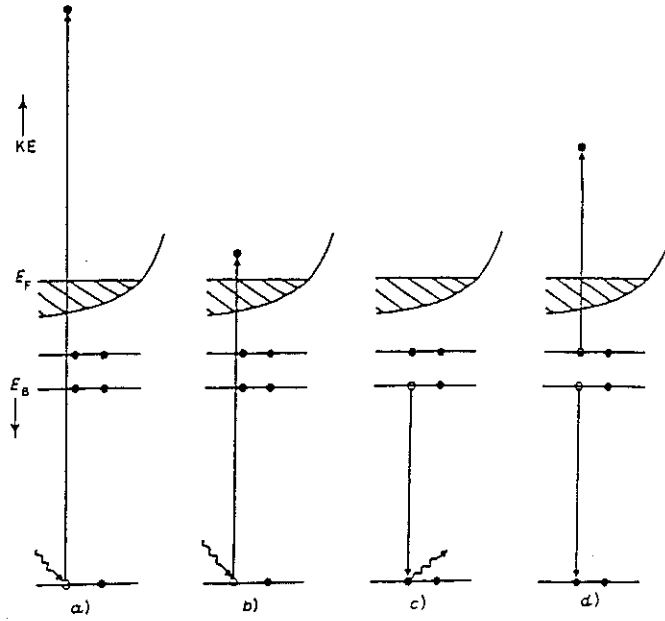


Figure 6.1: Schematic representation of the transitions involved in some spectroscopic techniques in a single particle approach. a) Photoemission spectroscopy (PES) (here: X-ray photoelectron spectroscopy (XPS)), b) X-ray absorption spectroscopy (XAS), c) X-ray emission spectroscopy (XES), d) Auger electron emission spectroscopy (AES). The figure is taken from [172]

In X-ray photoelectron spectroscopy (XPS or ESCA (electron spectroscopy for chemical analysis)), the energy conservation law gives for the kinetic energy E_{kin} of the photoemitted electrons

$$E_{kin} = h\nu - E_b - \Phi \quad (6.1)$$

where $h\nu$ represents the energy of the incident photons, E_b the binding energy and Φ specifies the work function for an electron to leave the solid. The theoretical description of the spectra is undertaken in the one step model where the photoemission cross section $\frac{d\sigma}{d\Omega}$ is approximated by [173, 174]

$$\frac{d\sigma}{d\Omega} \sim \rho(E_f) |\langle \Phi_f | \vec{A} \vec{P} | \Phi_i \rangle|^2 \delta(E_f - h\nu - E_i) \quad (6.2)$$

for the transition between the initial Φ_i and final state Φ_f with the density of states $\rho(E_f)$. Here, \vec{A} is the vector potential of the incident light, \vec{P} the momentum and the δ -function ensures the validity of the energy conservation law. The calculated δ -function peaked states need then to be convoluted with

Lorentzian, Gaussian and/or Doniach-Sunjić envelope functions, in order to account for the experimental line shape, in the present systems in particular for lifetime effects and instrumental broadening.

The experimental photoemission spectrum coincides with the excited spectrum of the hole-state left behind by the photoemitted electron, leading to complex interactions - especially in highly correlated many electron systems. Particularly in rare earths, the electrons in the unbalanced 4f shell move in a highly correlated manner, resulting in a large promotion energy $E(4f^{n-1}) - E(4f^n)$, which prevents to associate the measured position of the excitation with the location of the 4f band obtained from ground state calculations. As a result of these correlations, the lanthanide spectra are characterized by a high abundance of spectral lines and a high density of energy levels with no apparent regularity, and the appearance of extended multiplet structures. Consequently, the spectra are classified as 'very complex' and their successful interpretation has only recently been accomplished despite the still remaining problems to treat correlated many-electron shells within the available schemes for calculating the electronic structure of solids.

These multiplet structures in the XPS core level spectra arise from the interactions during the photoemission process of a core level hole with the spins and magnetic moments of the unbalanced 4f-electronic shell, which is considered to remain atomic like within the sudden approximation. Thus, the integral 4f population is not altered in this transition and the final states are expressed as a distribution of eigenstates resulting from the coupling of the core level hole with the incomplete 4f shell. This mechanism gives rise to complicated multiplet structures in the XPS core level spectra as shown at the example of the Tb 4d multiplet of TbNiSb spread over an energy range of about 30 eV (figure 6.2). The Tb 4d multiplet in TbNiSb is compared with theoretical calculations of pure Tb in the intermediate coupling scheme [176]. Note that their calculations do not take into account electron loss effects and lead to a Tb peak at 161 eV. However, this peak originates from background effects as proved by electron energy loss measurements, showing the necessity to incorporate this technique when analysing the multiplet structure. In addition the spectrum has been fitted - just for illustration purposes - with 10 peaks which would correspond to 10 electronic states in the one electron model of the Russell Saunders (LS) coupling scheme. This approach is for the Gd 4d multiplet a reasonably good approximation for the first well separated, equally spaced 4d multiplet states, as the half filled Gd 4f shell reduces the complexity of the interactions [177]. However, the very large spin orbit splitting of the total RE 4d multiplet structure, which is comparable to the exchange interaction of the 4f subshell, results in the invalidity of the

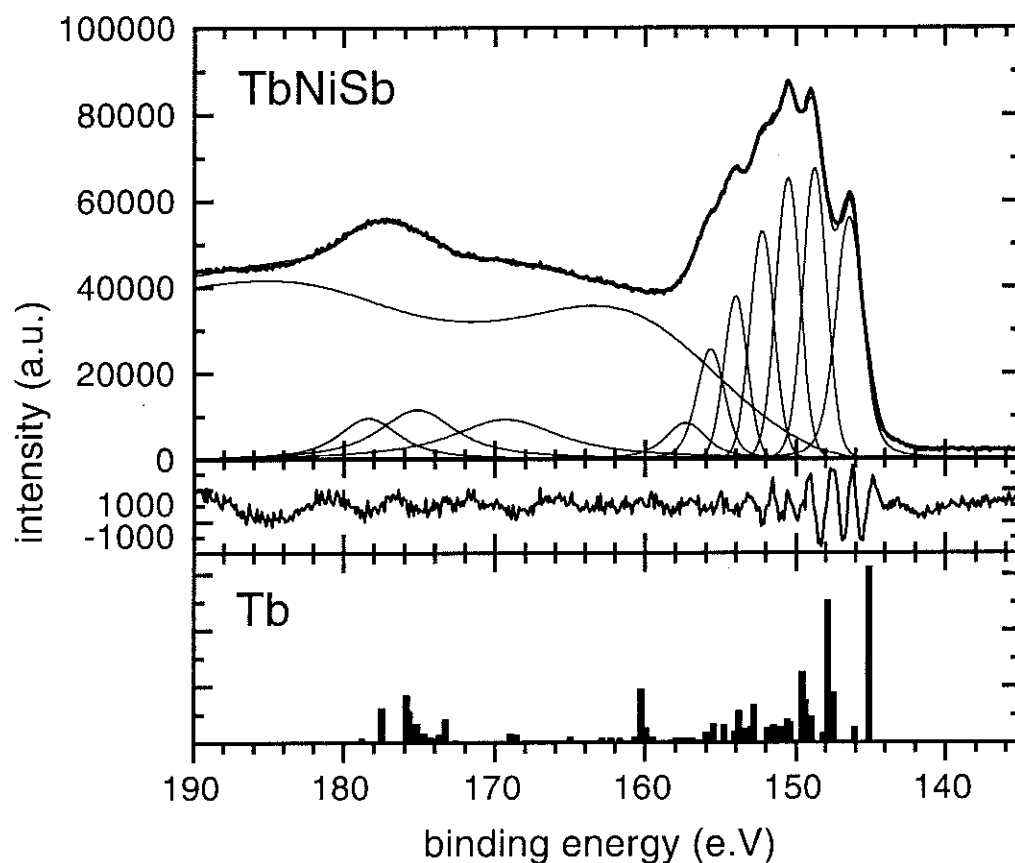


Figure 6.2: Tb 4d high resolution multiplet in TbNiSb. The experimental XPS high resolution Tb 4d multiplet structure of TbNiSb, broken in situ, (top curve) is deconvoluted mathematically with the help of the program Simpeak [175], using the background as measured by electron energy loss spectroscopy (EELS). The bar diagram displays many body calculations in the intermediate coupling scheme for Tb thin films [176]. See the text for details.

LS coupling scheme and the spin S of the $4f$ shell is no longer a good quantum number [150]. This is in particular true for those rare earths which do not possess an empty, half or fully filled $4f$ shell. Consequently, the simple one electron LS-approximation is no longer applicable, and the intermediate coupling scheme has to be employed in order to treat correctly the effects occurring in the RE $4d$ multiplet structures [176, 178]. Another theoretical approach to describe the $4d$ multiplet may calculate ab initio the $4d$ multiplet by starting with the potentials and then solving the Dirac equation as it has successfully been carried out for less complex systems [179, 180].

6.2.2 Resonances

The large spatial overlap of the $4d$ and $4f$ orbitals of rare earth atoms supports a strong resonant enhancement of the photoemission cross sections, caused by two strongly interfering distinct photoemission and decay channels in these many electron processes. In a generic picture, the indirect channel of the resonant photoemission is interpreted as due to a process where a $4d$ electron in the initial state $4d^{10} 4f^n$ is first excited to the unoccupied $4f$ level, forming a tightly coupled, bound intermediate state $4d^9 4f^{n+1}$, followed by a decay via autoionisation. The resulting final state $4d^{10} 4f^{n-1} (+e^-)$ is identical with the one reached by direct photoemission, as sketched in figure 6.3. Since

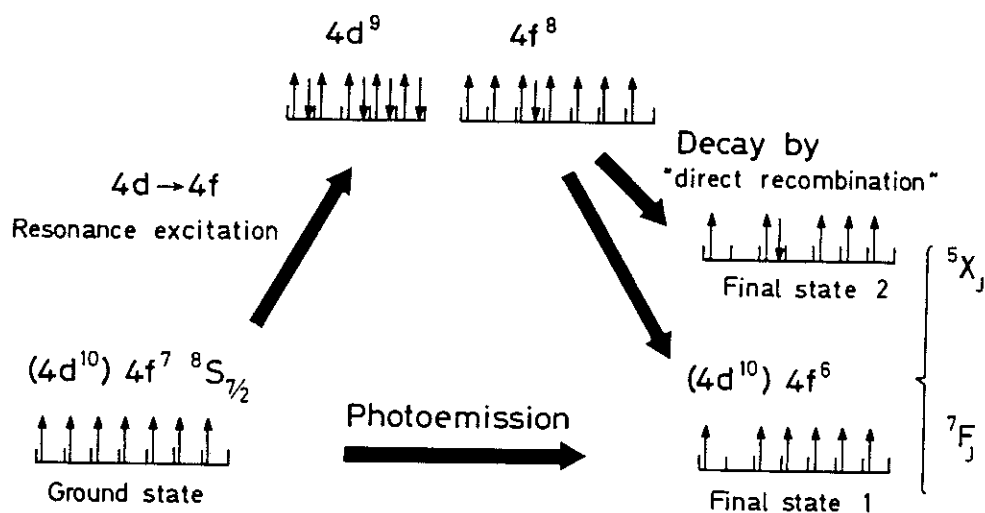


Figure 6.3: Illustration of the $4f$ photoemission process and the decay channels of the resonantly excited $4d^9 4f^8$ configuration in Gd [181, 182]

the intensities of the excitation and decay channels are of the same order of magnitude, their quantum mechanical interferences produce a dramatic enhancement of the photoemission cross section at incident photon energies above the 4d→4f photothreshold and a reduced one below.

The corresponding theoretical model for this resonance mechanism was derived by Fano [183], describing the interactions between one discrete state and one continuum which finally yields in an asymmetric line shape, usually referred to as *Fano profile* illustrated in figure 6.4 and given by:

$$\sigma = \frac{(q + \epsilon)^2}{1 + \epsilon^2} \quad (6.3)$$

Here, q is an asymmetry-parameter and the reduced energy variable $\epsilon = \frac{E - E_r}{\Gamma/2}$ depends on the the width Γ and the position of the resonance E_r .

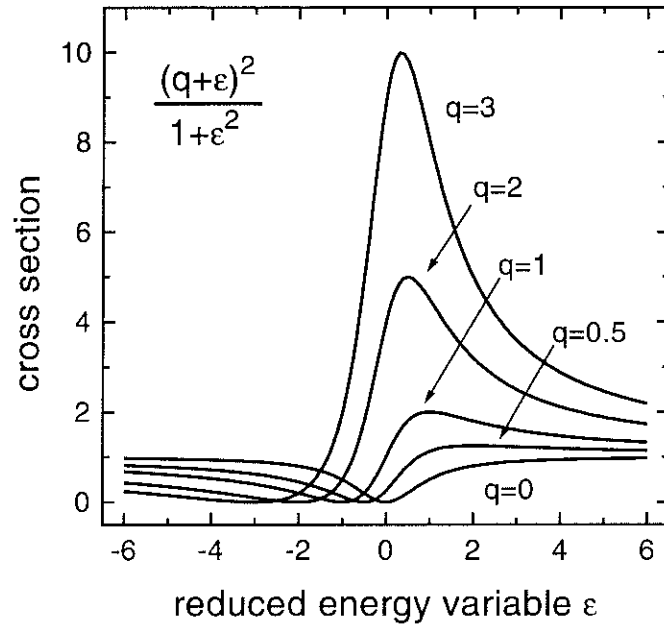


Figure 6.4: Calculated Fano profiles for a single resonance channel versus the reduced energy variable ϵ in dependence of different asymmetry parameters q

This first approach for one single resonance channel has been extended to the general case [160, 184, 185, 186], where one is confronted with the coupled interactions between many discrete states and many continua. In this situation, complicated interference effects lead to a large amount of coupled resonance channels making thus the theoretical description rather

complex and no simple parametrized expression can be used to describe the partial and total photoemission cross sections. Only in the limit of weak coupling between some (groups of) resonance channels, e.g. if each discrete state interacts with a unique set of continua, the resonance curve might be approximated by a superposition of different Fano profiles [147, 187].

6.3 Experimental

The X-ray photoemission spectroscopy (XPS) and electron energy loss spectroscopy (EELS) measurements were carried out with a commercial PHI 5600ci multitechnique spectrometer in Osnabrück, constructed by 'Physical Electronics' as sketched schematically in figure 6.5. Monochromized Al K_{α} radiation of 1486,6 eV (or an electron beam in the case of EELS) is impinging on the sample, the subsequently photoemitted electrons are then detected with a 11', 180° spherical multichannel analyser having an experimental resolution of about 300 to 400 meV.

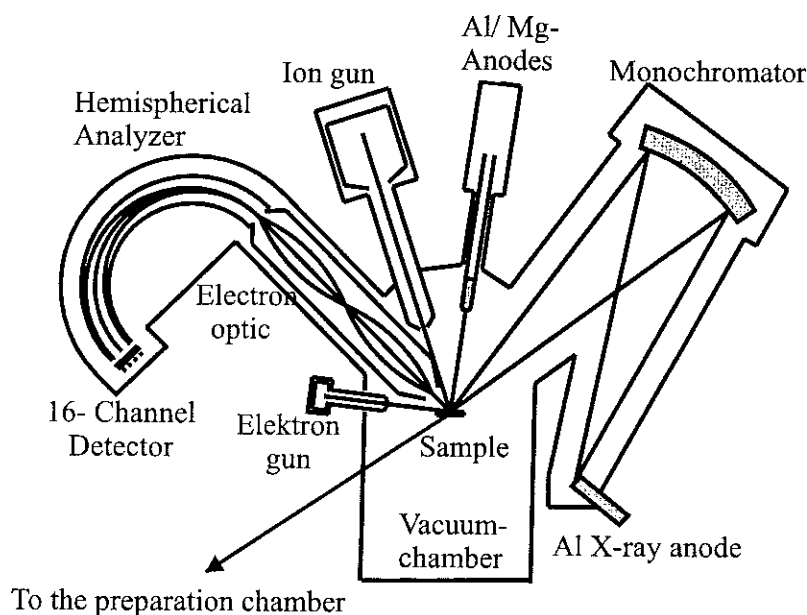


Figure 6.5: Sketch of the PHI 5600ci multitechnique spectrometer in Osnabrück employed for the XPS and EELS measurements. The figure is reproduced from [188].

Synchrotron radiation offers a high brilliance, intense, tunable light source [189, 190], which was employed for resonance measurements at the BESSY I storage ring in Berlin using the photoelectron spectroscopy system ADES 400 at the monochromator TGM 2. The latter monochromator has three switchable gratings, of which the high energy one ($90 < h\nu < 180\text{eV}$) supplies only a low photon flux which then yields to a small counting rate, especially in combination with the small acceptance angle of the single channel analyser optimized for angle resolved measurements. Despite of the resulting poor data statistics when a series of spectra needed to be taken within the limited time available after a surface cleaning and realignment process, the physical information could nevertheless be clearly extracted.

X-ray emission spectroscopy (XES) measurements were performed on a RSM-500 X-ray spectrometer in Yekaterinburg, Russia. The second order reflections were employed to register the photons emitted from the $\text{Ni}L_\alpha$ ($\text{Ni } 3d4s \rightarrow \text{Ni } 3p_{3/2}$) and the first order ones for the $\text{Sb } M_{4,5}$ ($\text{Sb } 5p \rightarrow \text{Sb } 3d_{5/2}$) transition with an energy resolution of 1.0 and 1.3 eV respectively. The energies of the XES-spectra were then calibrated to the position from known lines of the pure elements.

Fully relativistic calculations of the band structure and of the electronic density of states (DOS) were carried out using the density functional theory with local density approximation (LDA). The one electron Schrödinger equation was solved self-consistently using the linear muffin-tin orbital (LMTO) method in atomic sphere approximation (ASA) including the combined corrections [191]. The exchange potential introduced into the calculation was obtained by the 'van Barth and Hedin' method [192].

6.4 Surface preparation

As photoemission probes the topmost atomic layers, the preparation of a clean surface is essential before photoelectron spectroscopy experiments. In the present work it was carried out in situ by breaking (RNiSb) or repeated scraping with a diamond file (Gd intermetallics), preserving the exact crystal stoichiometry but the latter cleaning technique damages any single crystalline order. In particular due to the high reactivity of rare earths and their compounds, the preparation of a single crystalline or ordered surface is a quite difficult and a challenging task, which has considerably limited and hindered a lot of research in this field of surface sensitive investigations.

In order to work around these preparation difficulties, vapour deposition

is widely used to grow in situ an ordered crystalline structure on a substrate [193, 194] in general restricted to pure elements and to more or less thin films. Provided hard and brittle crystal properties, some of these single crystalline rare earth compounds may be cleaved along one of the crystal planes [195]; the mechanical properties of our Gd intermetallics inhibited this approach. In contrast to less reactive elements and compounds [196], the contaminants of bulk rare earth crystals and compounds, like O, H and C, can hardly be depleted by the usual UHV sputter-anneal cycles [197, 198] and so far no publication is known to us where such a single crystalline intermetallic rare earth compound has successfully been cleaned by these UHV sputter-anneal cycles for performing angle resolved photo emission spectroscopy measurements.

The latter approach was tried on two small (semi-) single crystals which were available in the present work, GdCu and GdCu₂ which consisted of two large grains, tilted against each other according to back reflection X-ray Laue diffraction. Various long Ar-sputtering and annealing cycles all led to the same observation that the oxygen contamination did not fall below a certain level so as if the samples were oxidised through the bulk and thus oxygen emerges continuously from the bulk to the surface. Since Gd is much more reactive than Cu, it can be supposed that the oxidation of Gd (to Gd₂O₃) dominates the present oxidation process of our Gd compounds, studied in detail on bulk Gd in the UPS energy range [199]. They have proved that - after Gd has finally oxidised to the stable Gd₂O₃ oxide - during subsequent heating, the Gd₂O₃ is decomposed, but the oxygen is not detached, instead the oxygen penetrates into the sample. This could explain why the oxygen remains on the surface of the Gd compounds and it suggests that Gd and its compounds may not be cleaned by annealing once the sample is oxidized.

Finally, we attempted without success to reduce the contaminating oxygen under a hydrogen atmosphere to H₂O, as it has successfully been applied at some non-rare-earth compounds, e.g. on CuO/Cu surfaces [200]. This attempt is principally critical for rare earths and many of their compounds, because on the one hand the rare earth atoms react easily with the hydrogen to a stable RE-hydrogen compound and hydrogen is adsorbed at the surface [137, 55], and on the other hand hydrogen diffuses quickly into the bulk; on Gd surfaces, this diffusion takes place at temperatures above 195 Kelvin [137, 201].

One further difficulty for GdCu consists in its martensitic phase transition CsCl \leftrightarrow FeB with a very low activation energy for the transition between the two stable crystal structures as explained in chapter 2.2. For this reason, any slight disturbance is sufficient to provoke a change of the crystalline structure

on a microscopic scale, preventing any long range order from remaining stable at the surface. The same result would be reached when e.g. polishing destroys the weak bondings of GdCu, thereby damaging any ordered structure.

6.5 Valence band

The valence band plays a particularly important role in understanding the physical behaviour of the compound, since it contains unfilled shells responsible for magnetic and spin moments, the states close to the Fermi-level control the chemical bondings and the electrical transport properties. When being embedded into a crystal structure, the electronic configuration of the elements may change in comparison with the one of the pure elements due to e.g. charge transfer and hybridisation effects resulting in new physical properties of the compound. As an example for a binary compound, the valence band of GdCu is briefly presented, measured at BESSY I, ADES 400, with an incident energy of 170 eV. As displayed in figure 6.6, the spectrum is dominated by two strong peaks, the Gd 4f and Cu 3d ones around 8.3 and 3.3 eV respectively, thereby hiding all photoemission features with weak intensities. Induced by the half filled Gd 4f shell with its pure spin configuration $^8S_{7/2}$ in the ground state, the 4f final states are energetically very close together, no multiplet splitting occurs (within the experimental resolution) and they form one single 4f peak within which no further details concerning the Gd 4f states can be resolved. In agreement with other Gd intermetallic compounds [202], the energy position of this peak undergoes a chemical shift from 8.1 eV in the pure Gd metal to 8.3 eV indicating a complex charge redistribution during the formation of the compound. Following the correlated charge model [203, 204], it may be calculated that a charge corresponding to about 1.6 electrons is transferred from the Gd to the Cu site. In the same way, the rare earth photoemission peaks in RNiSb suffer a positive chemical shift towards higher binding energies in comparison to the positions in the pure metals, caused by a charge transfer of rare earth electrons to the antimony site.

While binary compounds have quite systematically been investigated with different characterisation techniques including photoemission [14, 177, 205, 206, 207] the electronic interactions are more complex and thus more interesting in these ternary compounds where less data are available. In particular, the group of RNiSb compounds has not yet been investigated with PES techniques and the obtained data are completely new. Therefore, the photoemission analysis in this chapter focusses on the group of RNiSb compounds on which the electronic structure was measured by X-ray photo-

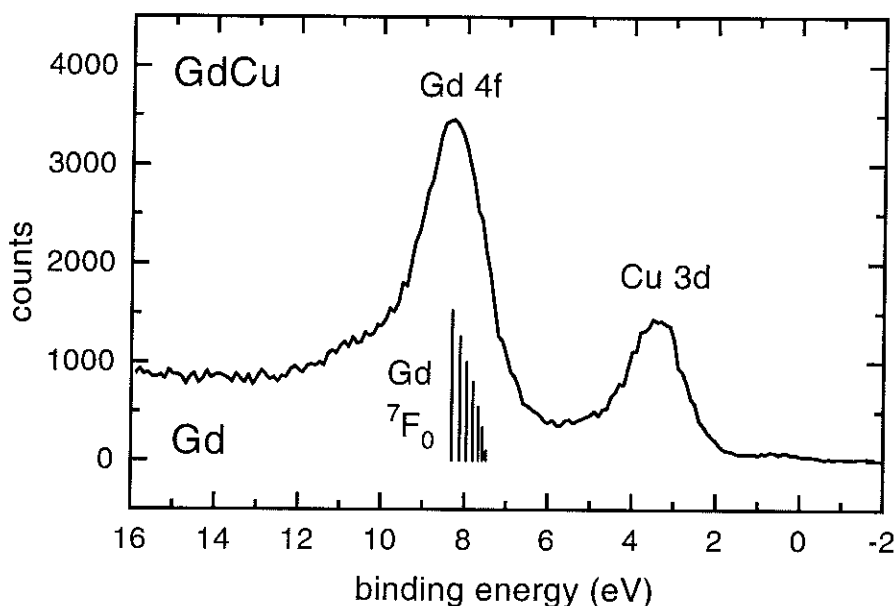


Figure 6.6: Valence band of GdCu measured at BESSY I with $h\nu = 170$ eV in comparison with calculations of Gd 4f final states for the pure Gd metal as drawn in the bar diagram. The calculations are taken from [142].

emission spectroscopy (XPS), as shown for the valence band in the figures 6.7 and 6.8. The spectra represent a superposition of the states from all three elements, they are dominated by the RE 4f states and - in the region of the Fermi level - by the Ni 3d states as discussed later.

Of particular interest are the RE 4f states with their unbalanced highly correlated electrons, since they are responsible for most of the special features observed in RE compounds. For instance, the energetic position of the 4f electrons describes the extent to which these electrons are considered as localised. Further, it indicates the ease with which the 4f electrons can be excited to states around the Fermi level which may give an estimate for the strength of coupling and hybridisation effects with the bands close to the Fermi-level.

In the light RNiSb compounds, the 4f states are situated at low binding energies approaching the Fermi level, and thus are in strong interaction with the outer valence electrons. The 4f levels in RNiSb are located around 0-2 eV for La, 0-2.5 eV for Ce, up to 3.5 eV for Pr, then further increasing steadily within this compound series, reaching 5 eV for the maximum intensity of Nd 4f in the investigated light RNiSb compounds. They all show a small chemical

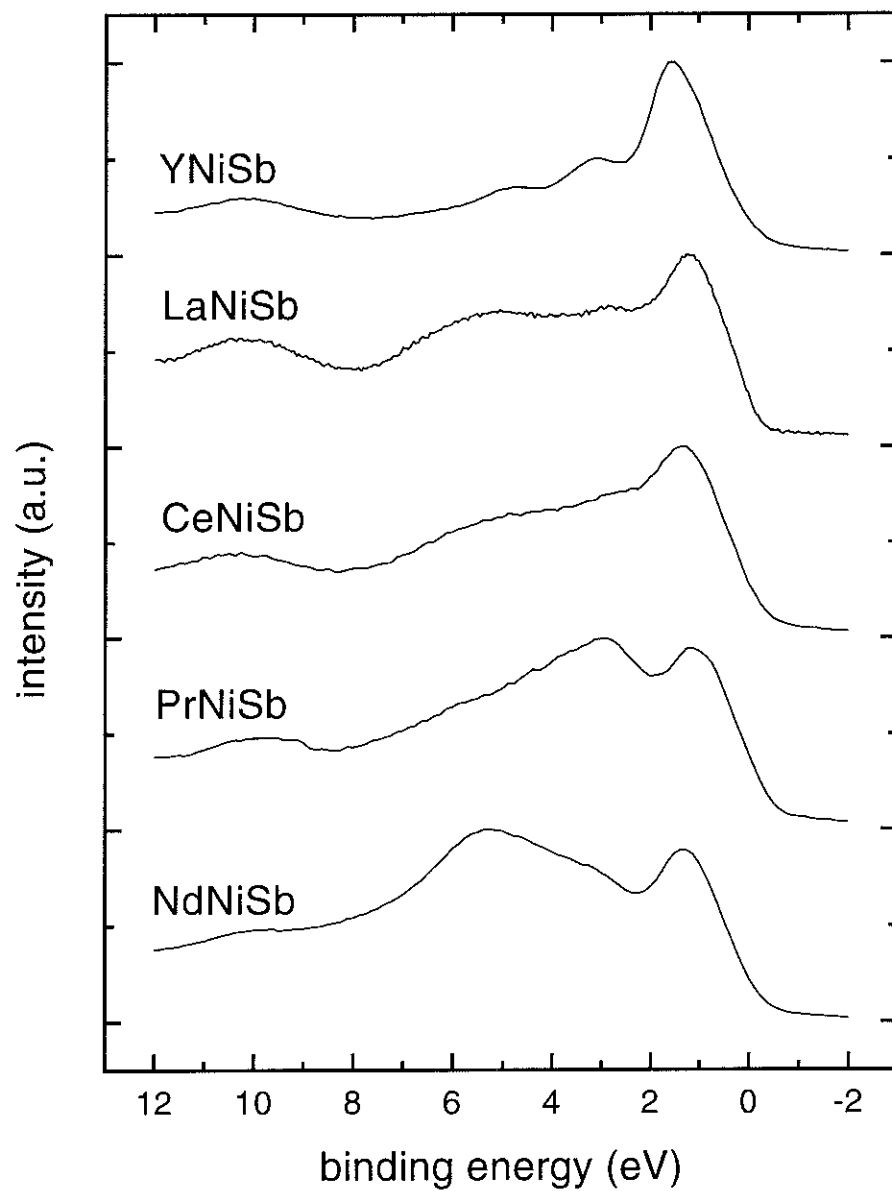


Figure 6.7: X-ray photoelectron spectroscopy of RNiSb compounds (R= light rare earth), see the text for details.

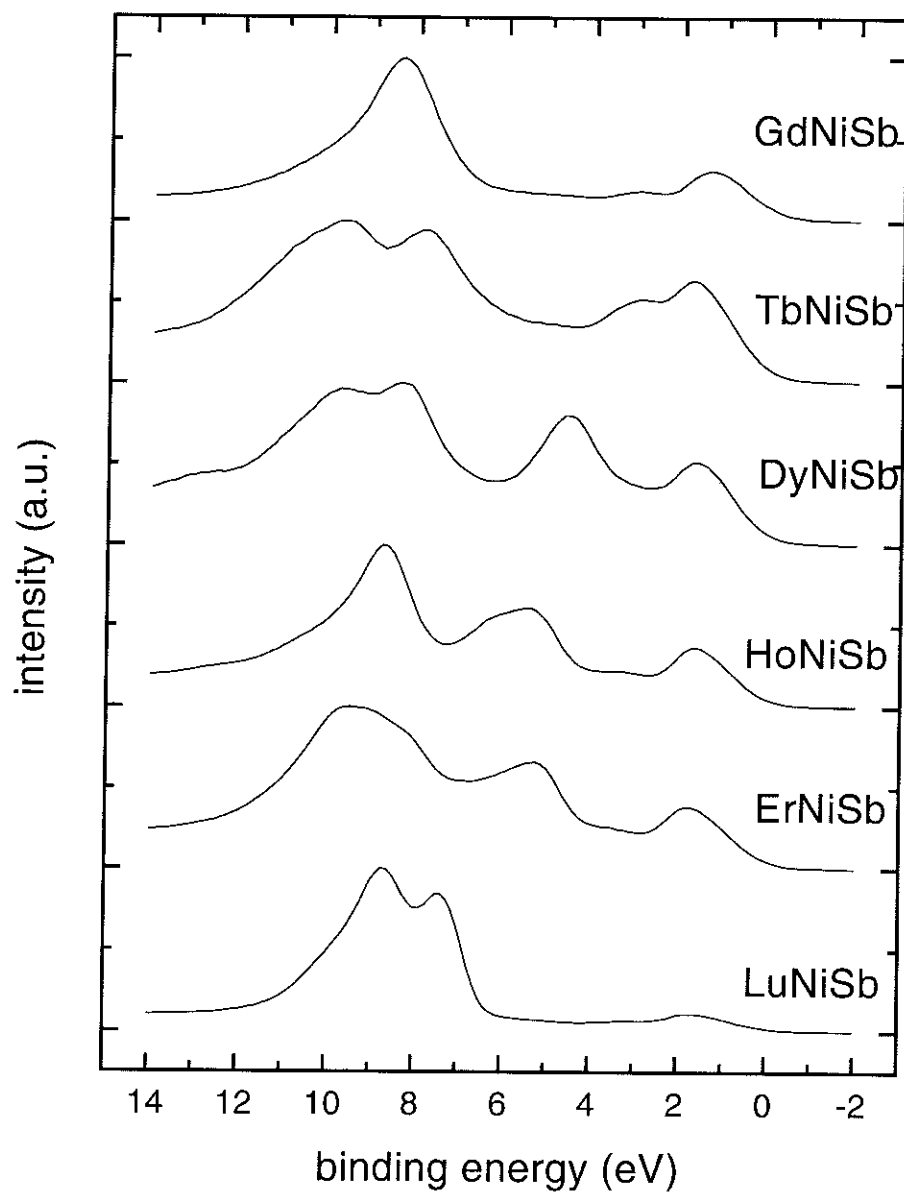


Figure 6.8: X-ray photoelectron spectroscopy of RNiSb compounds (R= heavy rare earth), see the text for details.

shift towards higher binding energies in comparison with the pure RE metals as discussed above. No fine details of the 4f states can be extracted from these data in the light RNiSb compounds, since the small spin orbit splitting causes the J-multiplets not to be resolved with XPS, especially since their 4f states are superposed by the Ni, Sb and R 5d6s² levels, present in the same energy range close to the Fermi level.

In contrast, the 4f states in the heavy RNiSb compounds are located more deeply, their most intense contributions to the 4f spectra emerge from binding energies in the range around 8 to 10 eV. Their spectra display a complex 4f final state multiplet structure, spread over a relatively wide energy range, provoked by the strong interactions, correlations, LS-coupling and exchange splitting of the 4f electrons under the influence of the hole created by photoemission.

The largest value of the exchange splitting occurs in TbNiSb of up to about 8 eV, where the seven Tb 4f electrons in the final state may align their spins to $S = \frac{7}{2}$, (⁸S) or $S = \frac{5}{2}$, (⁶X), leading to an exchange splitting which is observed to be larger than expected according to the simple coupling model, caused by various relaxation processes taking place in the excited atom [208] [209]. The principal Tb 4f peaks around 7.8 and 9.7 eV are composed of the ⁶P, ⁶I, ⁶D and ⁶G, ⁶F, ⁶H states respectively as calculated for pure Tb [143] and reproduced in figure 6.9. For a compound, the calculated energy positions of all Tb multiplet states shift slightly to higher binding energies, especially the ⁸S_{7/2} peak undergoes an appreciable shift being then located at 3.1 eV according to a calculation for TbSb [210, 211]. For Tb films on Ni(111), the Tb ⁸S_{7/2} multiplet has also been discussed as two peaks, ⁸S_{7/2}^u at 3.1 eV and ⁸S_{7/2}^s at 2.1 eV binding energy for an moderate coverage (2-4 monolayers), 2.8 eV and 2.2 eV for thick films (> 8 monolayers) [212].

Apart from a chemical shift towards higher energies and some subtle variations, the 4f multiplets of all these RNiSb compounds remain quite similar to those obtained from the pure RE metal, resulting from the localized character of the 4f core levels, which is little influenced by the chemical environment. Therefore, the RNiSb multiplet structures and their final state spin distributions can be interpreted with the help of existing data for the pure RE elements reviewed in [143, 211, 213, 214]. The XPS spectrum of GdNiSb shows one single Gd 4f peak arising from the final state ⁷F configuration situated at 8.3 eV below the Fermi level. This shows that the Gd 4f shell is quite stable. All spectra in the figures 6.7 and 6.8 are normalised to the maximum intensity, which causes the LuNiSb spectrum to be dominated by the Lu 4f peak, due to the large partial photoemission cross section of this

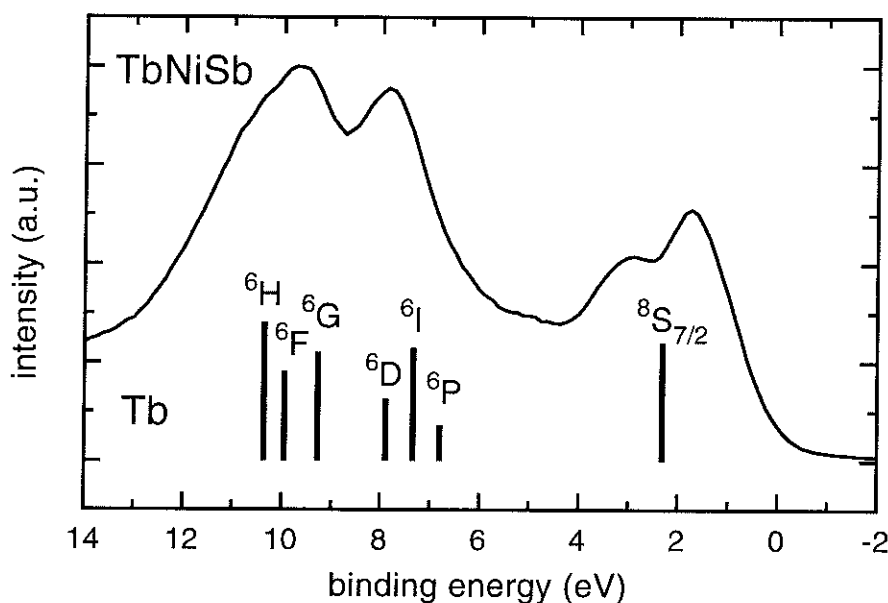


Figure 6.9: XPS spectrum of the TbNiSb valence band, compared with the calculated $^{2S+1}L_J$ configurations for pure Tb [143]. In the TbNiSb XPS spectrum, the peak at 1.7 eV is dominated by the Ni 3d states while the peaks at 3.0 eV and between 7 and 11 eV originate from Tb contributions.

completely filled shell [215].

While the photoemission peaks arising from the rare earth 4f electrons vary strongly, the Ni and Sb states do not change significantly between different compounds of this series. As the photoemission spectrum is a superposition of all elements and shells, calculations of the partial density of states (DOS) are a powerful tool to distinguish the different contributions, although the emission intensity still needs to be convoluted with the partial photoemission cross section, and the spectrum of excited states is not described. The latter causes this approach to be unsuitable for analysing the excited PE spectrum arising from highly correlated 4f electrons; however, these simple calculations generally agree sufficiently well with the spectra of non-correlated shells.

Total DOS calculations were performed on YNiSb which were found to be in good agreement with the XPS spectrum as compared in the top graph in figure 6.12; the contributions from each atomic shell are resolved by partial DOS calculations, shown in figure 6.10. They reveal that the Sb 5s states clearly dominate the peak around 10 eV, visible as a weak peak in the light

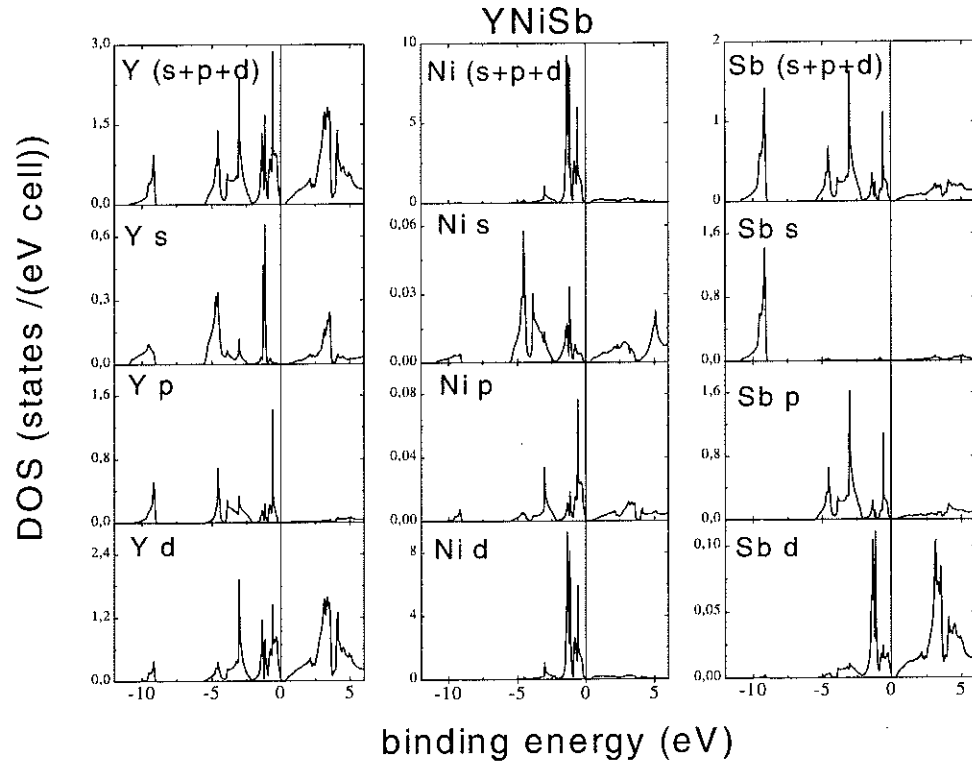


Figure 6.10: Calculated partial density of states for the Y, Ni and Sb subshells in YNiSb [111].

rare earth compounds. In the heavy rare earth compounds, these Sb 5s states lead to a broadening of the intense 4f peak(s) at the high energy side.

The valence band close to the Fermi level is constituted by the states from all elements, principally the R5d,6s, Sb5p and Ni3d ones, outlined in the partial DOS figure 6.10. Considering the relative DOS and the photoemission cross sections [215], it is obvious that in the RNiSb spectra the first peak structure between 0 and 2 eV is clearly dominated by the Ni 3d electrons superposing the Sb and RE states and thereby hiding any fine details of the contributions originating from these elements. The overlap in the wave functions becomes even clearer in the calculated band structure (figure 6.11), showing a strong hybridisation due to the bands around 1 to 1.5 eV, promoting an sp^3 hybridisation around the Sb atom. It also displays the indirect gap at the Fermi level and the existence of a second region without electronic states located between 6 and 9 eV. This lack of states in the valence band

occurs quite frequently in semi Heusler compounds and Kondo insulators [216, 130, 217], facilitated by their narrow band character and semi-covalent bonding [25, 28]. In the heavy RE compounds, this region is filled by the 4f electrons, their localized character might play an important role for the observed effects.

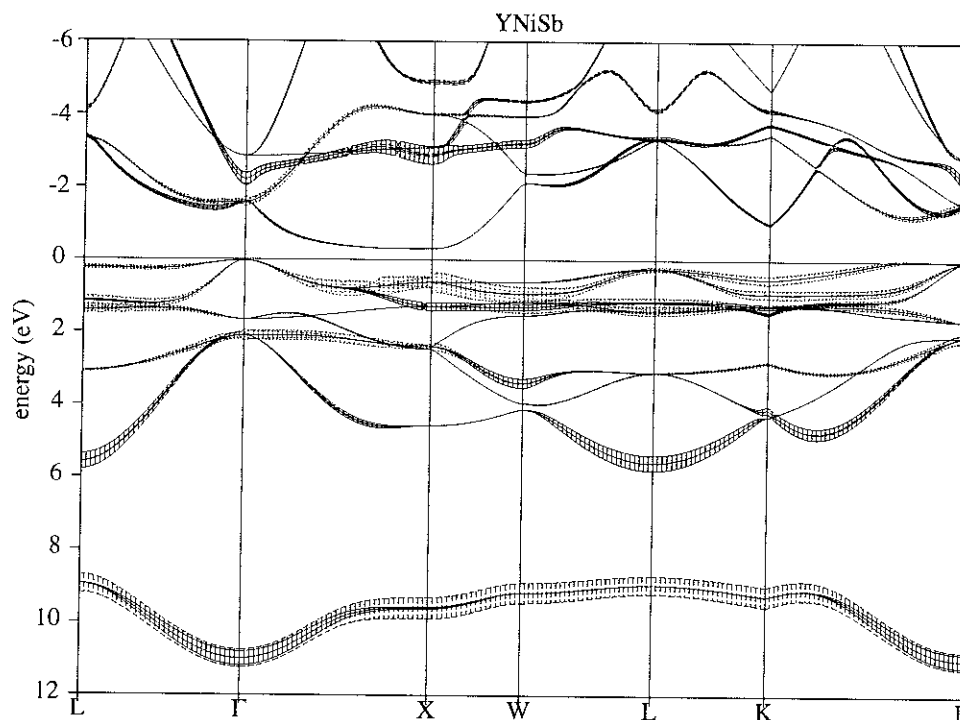


Figure 6.11: Calculated band structure of YNiSb [111]. The width of each band represents the degree of hybridisation. For instance, the lowest band represents Sb *s* states, mostly hybridized with Sb *p* ones.

Due to smaller overlap of the Ni 3d wavefunctions in RNiSb in comparison to the situation in pure Ni, the Ni states are slightly moved to higher binding energies, forming a slowly decreasing DOS towards the Fermi level. This leads to a relatively low density of states at the Fermi level, supporting the formation of either semi-metals or narrow-gap semiconductors. It depends only on slight variations of the electronic structure when changing the rare earth element within this compound series as it was observed by transport measurements (chapter 4). This slow decrease of the electronic DOS towards the Fermi level contrasts to the one of the pure Ni metal, which possesses a large DOS down to the Fermi edge, followed by a sharp cut off, hence

displaying a triangular shape of the photoemission spectra of Ni [218]. The deeper lying Ni bands also agree with the observation that Ni carries no magnetic moment (chapter 3), since a deeply lying shell is more likely to be completely filled. Thus, it can be anticipated that the Ni 3d subshell may be fully occupied in the $3d^{10}$ configuration.

X-ray emission spectroscopy (XES) measurements were performed on six RNiSb compounds at the NiL_α ($Ni\ 3d4s \rightarrow Ni\ 3p_{3/2}$) and the Sb M_{4,5} ($Sb\ 5p \rightarrow Sb\ 3d_{5/2}$) transition, probing the local density of Ni and Sb states as shown at the example of YNiSb in figure 6.12. Caused by the poor data statistics and the low energy resolution of 1.0 and 1.3 eV, only one broad Ni and Sb peak is observed integrating over all states, confirming nevertheless the partial DOS calculations that the mean position of the Ni states is located closer to the Fermi level than that of the Sb states. The large half width of the XES peaks may also suggest the presence of enlarged hybridised bands in this energy range.

6.6 Resonances

6.6.1 Gd resonance results

The resonant enhancement of the shallow core level intensities was studied on several rare earth compounds, caused by inter-shell interactions promoted by the spatial overlap of the orbitals. Among the investigated intermetallic compounds, the $4d \rightarrow 4f$ resonance of GdCu is presented as an example for a comparatively less complex situation, since Gd possesses a half filled 4f shell which limits the amount of possible electronic configurations in the excitation and decay processes involved.

As shown in the 3-dimensional overview in figure 6.13, all Gd states - the 5p, 4f and the $5d6s^2$ ones close to the Fermi level - display a pronounced resonant enhancement of the photoemission cross section with its maximum around 149 eV and a suppression of intensity directly before, proving that all these Gd states participate at a Fano-type resonance process. These resonances in the valence band are analysed closer in the following by constant initial state (CIS) spectra, showing a typical Fano lineshape of the main resonance peak (giant resonance), preceded by narrow and weak lines in the structure around 139 to 144 eV. This Fano resonance is also observed at the more tightly bound $5p_{1/2}$ and $5p_{3/2}$ peaks in the region around 20 to 30 eV [220] which has been discussed in detail on Gd thin films [148]. Contrarily,

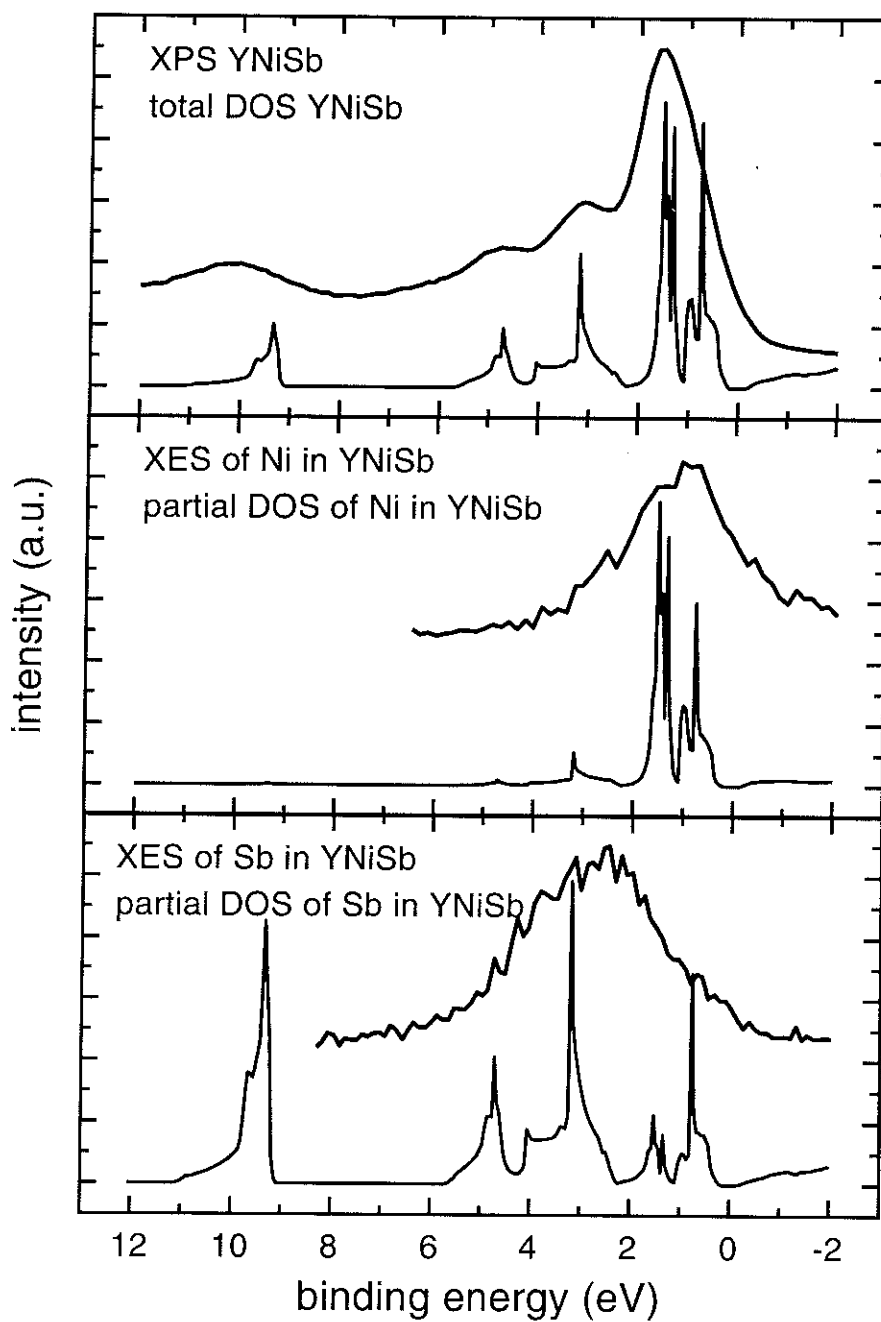


Figure 6.12: Comparisons for YNiSb of the calculated total and partial DOS [111] with X-ray photoemission spectroscopy (XPS) and X-ray emission spectroscopy (XES) [219], probing the partial DOS of Ni and Sb respectively.

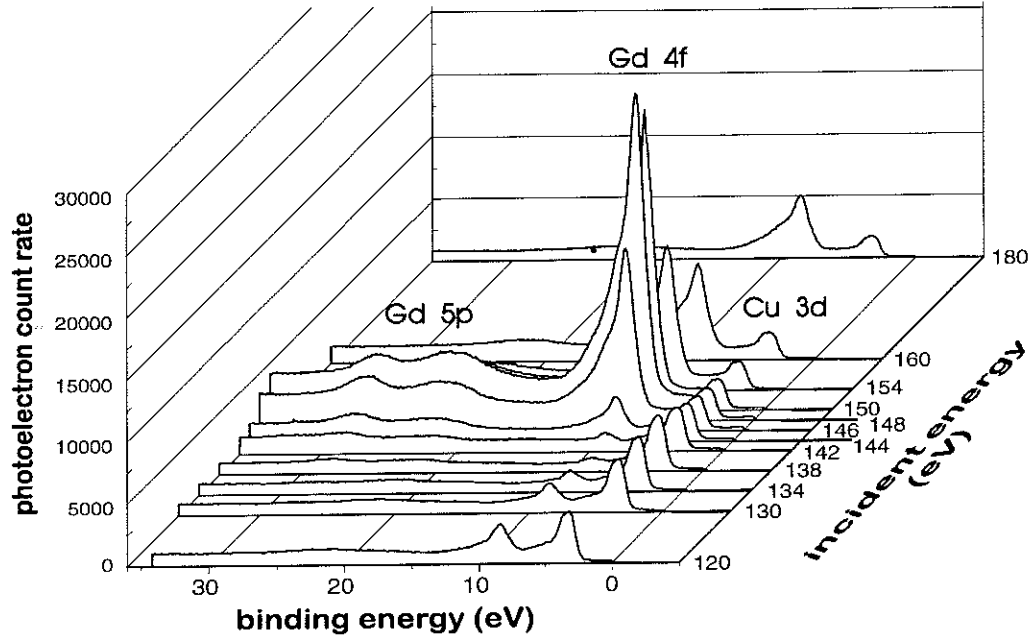


Figure 6.13: Series of photoemission spectra (EDC) of GdCu at varying incident energies in the region of the Gd $4d \rightarrow 4f$ photothreshold. This experiment was carried out at the synchrotron BESSY 1 at the High Energy PGM 1 which supplies a large photon flux in this energy range. The spectra are normalized to the incident photon flux.

the Cu 3d peak undergoes an antiresonant suppression of the photoemission intensity at those incident energies, where Gd $4d \rightarrow 4f$ resonance is centered (given by E_R in the Fano formalism).

An additional weak structure, which cannot be observed in direct photoemission, emerges at around 12-15 eV in a zoomed, high resolution EDC spectrum at incident energies around 143 eV, where the interferences strongly suppress the photoemission intensity of the main peak. It originates from excited quintet 5X_J configurations of the Gd $4d^{10} 4f^6$ final state reached by the Auger decay of the resonantly excited Gd $4d^9 f^8$ intermediate configuration [147, 181] as sketched above in figure 6.3.

6.6.2 Gd resonance discussion

The complexity of the interactions involved in the Fano mechanism is reduced for the case of the half filled Gd 4f shell, since all seven 4f electrons form one pure single spin state ($^8S_{7/2}$), being located energetically very close to each other as indicated through the single Gd 4f peak in XPS (figure 6.6). Therefore, it can be assumed, that all principal resonance channels involved lead to Fano profiles at the same energy, thus allowing the approach to fit of the main resonance peak with one single Fano lineshape, leading to $E_R=147.80$ eV, $\Gamma=5.73$ and $q=2.32$ (figure 6.14).

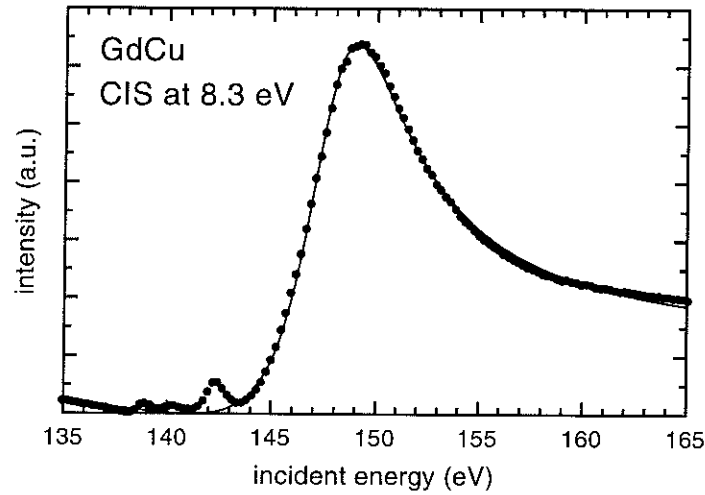


Figure 6.14: Constant initial state spectrum (CIS) of GdCu at a binding energy of 8.3 eV corresponding to the Gd 4f photoemission peak. The experimental curve (dotted line) has been fitted with a Fano profile (smooth line) leading to the Fano parameters $E_R=147.80$ eV, $\Gamma=5.73$, $q=2.32$.

In order to measure the strength of the interactions between the discrete and the continuum states in GdCu, the asymmetry parameter q can be used [160], which was reported to range typically from 2.0 to 4.0 in transition metal and rare earth atoms [146, 147] and a value of $q = 3.2$ was found for 4% Gd diluted in a II-VI semiconductor [187]. Since the the Fano parameter $q^{GdCu} = 2.32$ is smaller in GdCu compared to the latter diluted semiconductor, stronger interactions are thus measured for the investigated GdCu compound. This suggests that - despite of the atomic character of the resonance process - the resonance is nevertheless influenced by the electronic surrounding of the Gd atom. However, it cannot be excluded, that

this comparison with the values from the literature might be affected by different experimental conditions and the sample quality. In the limit of a large q , the Fano lineshape approaches a symmetric Lorentzian peak, a shape which is experimentally observed for the peaks in the prestructure, indicating weak interactions of the latter with the direct photoemission process. This becomes evident, when considering that this prestructure originates from quintet states [181, 187], which cannot be reached by the direct photoemission process as indicated above in figure 6.3. In this way, the prestructure originates from coupled resonances between different channels [221, 160]. Derived from resonant MCD calculations [149], these were interpreted as due to $^{2S+1}D_J$ configurations ($^8D_{9/2}$, $^8D_{7/2}$, $^6D_{9/2}$, $^6D_{5/2}$). As opposed to this, the main resonance peak is attributed to the 8P_J ($J = \frac{5}{2}, \frac{7}{2}, \frac{9}{2}$) configurations, dipole excited from the $^8S_{7/2}$ ground state in the limit of the vanishing spin orbit coupling. Due to the differences in the super Coster Kronig decay rates, the lifetime of the states in the prestructure is about 10 to 20 times larger than the one of the main resonance, leading to a sharper line shape for the peaks in the prestructure [222]. However, due to the low signal to noise ratio, a more detailed analysis of the prestructure cannot be undertaken on the basis of the present experimental data. For these reasons, the analysis of the Fano-profiles is concentrated on the main resonance peak.

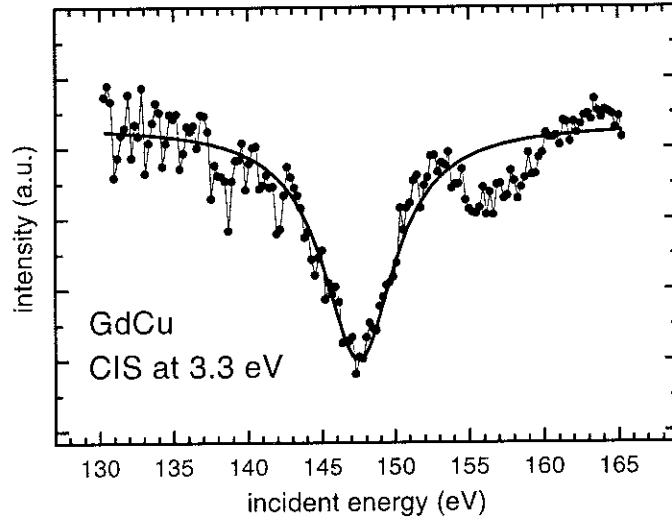


Figure 6.15: Constant initial state (CIS) spectrum of the Cu 3d peak at 3.3 eV binding energy in GdCu (dotted line). It shows a clear Fano antiresonance fitted by $E_R=147.50$ eV, $\Gamma=6.0$ and $q=0.0$ (solid line).

In contrast to the resonant enhancement of the photoemission intensity

observed on all rare earth peaks, figure 6.15 shows a clear suppression of the photoemission cross section of the Cu 3d peak at 3.3 eV, fitted by a Fano antiresonance profile with the asymmetry parameter $q = 0$. This behaviour could originate from the special form of configuration interactions, where the different excitation and decay paths mutually annihilate in such a way that a symmetric suppression of the intensity occurs [223], described in the limit $q = 0$ of the Fano theory according to equation 6.3. The drop in intensity between 155 and 160 eV resembles an inverted prestructure of a Fano profile, however the origin for this behaviour cannot surely be determined on the basis of one single spectrum. Such kind of antiresonances are sometimes observed in various 3d [224, 225, 226, 227] and rare earth compounds [228, 187], always being explained by referring to the Fano formalism.

6.6.3 Tb resonance results

While in Gd compounds all 4f photoemission spin states are situated within one single peak and only one principal resonance energy occurs, the situation becomes more complex in the case of heavy rare earth compounds which have several 4f peaks in the valence band and form a complex multiplet structure. The situation is principally similar - as far as this problem is concerned - between the different heavy rare earth compounds: Localised 4f levels, spread over a considerable energy range and showing two principal peaks, as indicated in figure 6.8. As an example for these compounds, TbNiSb has been investigated, which has two main 4f peaks containing the 6I , 6P , 6D and 6G , 6F , 6H spin distributions in addition to the well separated $^8S_{7/2}$ exchange splitting satellite (figure 6.9).

The resonant behaviour of TbNiSb was investigated at the monochromator TGM2 at BESSY I in the same way as described above for the GdCu measurements. As a result of the low photon flux at the high energy grating, combined with a limited measuring time for a complete series of spectra, the statistics of the experimental data are low, enabling nevertheless clearly the identification of the physical processes.

Photoemission spectra of TbNiSb were taken at a series of different incident photon energies revealing a pronounced Fano-resonance as presented in the 3-dimensional overview in figure 6.16. While the energetic position of the peaks varies little with photon energy, their intensity undergoes large variations in the region around the 4d \rightarrow 4f photothreshold, showing a strong resonance peak above and a reduced intensity before the threshold.

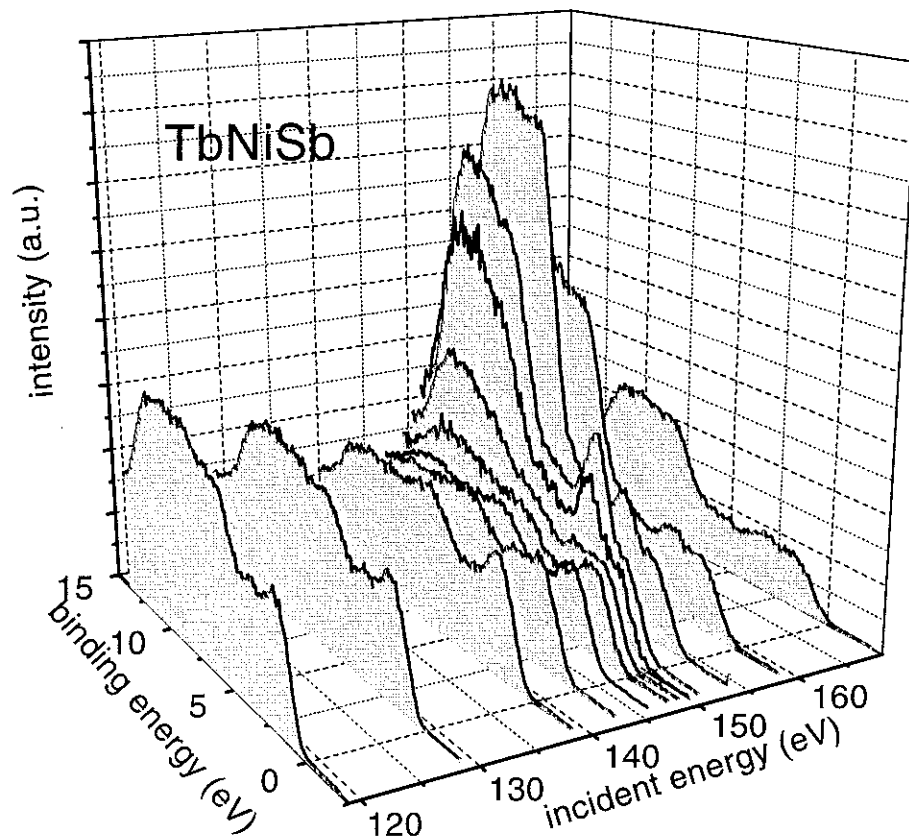


Figure 6.16: Valence band of TbNiSb at different incident photon energies. The spectra are normalised to the photon flux impinging on the sample.

To analyse this resonance in more detail, constant initial state (CIS) spectra (figure 6.17) were taken at the different Tb states in the valence band of TbNiSb, shown in figure 6.9. All spectra display an asymmetric line shape, rather similar to a Fano profile, preceded by a small prestructure around 142-143 eV, which is caused by coupled resonance channels as already discussed above. The CIS spectra have been normalized to the incident photon flux impinging on the sample showing that the absolute intensity of the prestructure remains constant within the experimental data statistics.

In contrast, a quite different behaviour is observed for the principal peak of the Fano resonance between 149 and 156 eV, depending on the 4f multiplet states of the Tb peak in the valence band on which the CIS spectra were taken. On the one hand, the CIS spectrum taken at 2 eV is sharp and narrow with its maximum intensity at 150 eV and a quick decrease of the

signal at higher energies; the shape resembles quite well with a typical Fano profile. Its absolute intensity reaches about 1/3 of the value detected at the CIS spectra taken at the principal 4f peaks at 8.3 and 9.7 eV binding energy. The latter display a broad main resonance peak with its maximum around 152-153 eV. The shape is much broader compared to the one from the pure, single Fano line shape, due to a superposition of several different resonance channels spread over a certain energy range. As some of these have different partial cross sections, some of the single resonance channels involved can be resolved from the subtle differences between the CIS spectra at 8.3 and 9.7 eV binding energy, which can best be seen in the difference plot in figure 6.17. At the very beginning of the resonance structure, there seems to be a single strong channel at 150 eV, visible in the sharp more intense difference peak at the resonance at 9.7 eV, while the broader structure at 151-153 suggests that it is composed of a few weak channels which show an increased partial cross section at the peak of 8.3 eV binding energy. The origin for this behaviour is analysed in the following paragraph.

6.6.4 Tb resonance discussion

In contrast to Gd compounds, the density of states of the Tb 4f multiplet is distributed over a wide range within the valence band, depending on the spin configuration of the final states as shown in figure 6.9. Thus, only the single $^8S_{7/2}$ final state spin configuration contributes to the resonance process of the CIS 2 eV spectra, strongly limiting the number of allowed resonance channels. It may be suggested that this resonance is clearly dominated by one single resonance channel at 150 eV directly at the beginning of the resonance processes, which in turn creates a sharp Fano line shape. The cross section of this peak measured at 2 eV is much lower than the one from the principal 4f peaks, due to the weaker $^8S_{7/2}$ density of states and the lower number of resonance channels involved.

On the other hand, the principal 4f peaks around 8.3 and 9.7 eV are composed of several multiplet configurations, $^6I, ^6P, ^6D$ and $^6G, ^6F, ^6H$ respectively, allowing the occurrence of several different resonance channels. Some of them have slightly higher resonance energies causing the maximum of the resonance intensity to appear at higher energies around 152-153 eV. This superposition of several different profiles, slightly shifted in energy, produces then a broad resonance structure, much broader than according to the pure Fano theory (equation 6.3) and broader than the profiles found for many transition and rare earths metals [146, 160].

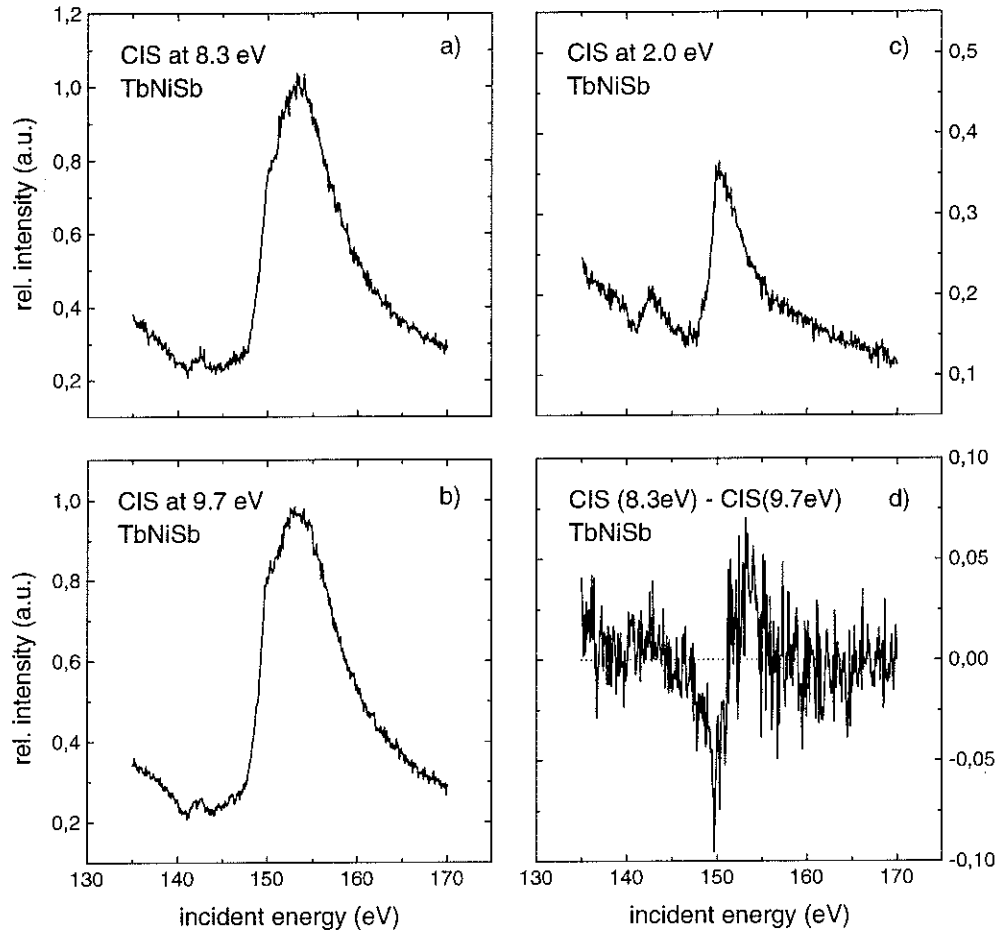


Figure 6.17: Constant initial state spectra of TbNiSb at different binding energies of 2.0, 8.3, 9.7 eV, corresponding to the Tb states $^8S_{7/2}$, ($^6I, ^6P, ^6D$), ($^6G, ^6F, ^6H$) respectively. The last graph shows the difference of the CIS spectra taken at 8.3 and 9.7 eV. The intensities of all these spectra are normalised to the same scale according to the incident photon flux.

initial state	excited state	final state	resonant threshold
$4d^{10}5s^25p^64f^85d^16s^2$	$4d^95s^25p^64f^95d^16s^2$	$4d^{10}5s^25p^64f^85d^06s^2$	152
		$4d^{10}5s^25p^64f^85d^16s^1$	152
		$4d^{10}5s^25p^64f^95d^06s^1$	152
		$4d^{10}5s^25p^64f^95d^16s^0$	152
		$4d^{10}5s^25p^64f^75d^16s^2$	152
$4d^{10}5s^25p^64f^85d^16s^2$	$4d^95s^25p^64f^85d^16s^26p^1$	$4d^{10}5s^25p^64f^85d^06s^2$	151
		$4d^{10}5s^25p^64f^85d^06s^16p^1$	151
		$4d^{10}5s^25p^64f^85d^16s^1$	151
		$4d^{10}5s^25p^64f^85d^16s^06p^1$	151
		$4d^{10}5s^25p^64f^75d^16s^2$	151
		$4d^{10}5s^25p^64f^75d^16s^16p^1$	151
		$4d^{10}5s^25p^64f^75d^06s^16p^2$	151

Table 6.1: Resonant photoemission processes for the valence bands of Tb thin films in the region of the Tb 4d→4f photothreshold taking a purely atomic model [212]. The resonant threshold depends only on the excited state and is then the same for all possible final states.

In a first approximation, the resonance mechanism could be considered as specific to the rare earth atom, allowing a comparison with the resonances observed in pure rare earth metals even if small differences in the resonance profiles may occur. Nevertheless, in a rare earth compound, the chemical bondings and hybridisations may considerably influence the rare earth states, in particular those around the Fermi level and affect thereby indirectly the resonance process as indicated in chapter 6.6.2.

However, for a qualitative result, an atomic model of Tb is applied, neglecting hybridisation and any lifting of degenerancies as a result of band symmetries, crystal field effects and spin interactions. In this way, there are a number of many electron excitations that can result in final states contributing to the photoemission valence band spectra as given in table 6.1 [212].

The remarkable aspect is that the resonant threshold of all these channels is entirely controlled by the first step in the resonance process, the excitation of a 4d electron; in particular, this resonance threshold is then independent from all possible final state configurations. In the case of Tb thin films, this threshold was determined to be 152 eV for the $4d^{10}5s^25p^64f^85d^16s^2 \rightarrow 4d^95s^25p^64f^95d^16s^2$ excitation and 151 eV for the one to the $4d^95s^25p^64f^8$

	Intensity	J	Energy (eV)	Intensity
${}^6\text{H}$	3.314	15/2	0.000	2.061
		13/2	0.430	0.849
		11/2	0.718	0.202
${}^6\text{F}$	2.000	11/2	0.953	0.919
		9/2	1.122	0.766
		7/2	1.362	0.275
${}^6\text{P}$	0.876	7/2	3.405	0.398
		5/2	3.535	0.849

Table 6.2: Final states of Tb^{3+} for the transition from $4f^8$ to $4f^9$, the initial state is ${}^7\text{F}_6$ [142]. See the text for explanations.

$5d^1 6s^2 6p^1$ intermediate state.

Since in the fully occupied Tb 4d core shell all moments and interactions vanish mutually, all ten 4d electrons are located at the same energy, which is determined as 146.25 eV from the beginning of the 4d multiplet structure (figure 6.2). As a consequence, any variation of the energetic position between different resonance channels depends only on the different Tb states in the valence band, which therefore needs to be investigated in more detail. Due to lack of TbNiSb calculations, some results obtained for Tb atoms are given as a qualitative indication only, to show how the spin and energy distribution of unoccupied Tb 4f states above the Fermi level might be composed. The intensities for the Tb $4f^9$ final states, arising from electron addition to the initial state $4f^8$ were calculated within the Russell-Saunders (LS) coupling scheme as tabulated in table 6.2 [142], where the corresponding energies were obtained from UV-absorption data [229, 230].

These calculations indicate the existence of two most intense final states, the ${}^6\text{H}_{15/2}$ and the ${}^6\text{F}_{11/2} + {}^6\text{F}_{9/2}$ ones. The relative energetic position of the latter is calculated to be roughly one eV above the initial ${}^6\text{H}_{15/2}$ configuration, exactly 0.95 and 1.12 eV; however, the states cannot be separated within the present experimental resolution and data statistics. The absolute energy for the first ${}^6\text{H}_{15/2}$ state may then be calibrated as about 2.75 eV, taken from Bremsstrahlung isochromat spectroscopy (BIS) in comparison with corresponding calculations [213].

In this way, the resonance threshold for a specific resonance channel may be calculated by the difference between these 4d and 4f states, giving a value of 149 and 150 eV, under the presumption that these states would appear in

the same way as in TbNiSb. The maximum intensity of the Fano profiles is then situated at incident energies slightly above the resonance energy of the threshold, depending on the shape of the profile, specified by its Fano parameters q and Γ . The experimentally observed values are roughly 1 eV larger than the ones calculated in this way. On the one hand, these differences originate from a large error bar resulting from mixing several different experimental and calculation methods for this estimation, depending on which data were available. On the other hand, the energy and composition of the states involved is different between TbNiSb and pure Tb, leading to shifted energies and to a different composition of the levels. Due to the high correlation in combination with a partly filled 4f shell, the situation is very complex in the case of Tb and Tb compounds, with strongly coupled parameters in the calculation procedure; slight variations, for example due to hybridisation effects, have large consequences on the resulting states. Furthermore, many body effects must be taken into account, since the 4f states alter significantly under the influence of a 4d core hole. Therefore, the simple model for Tb and free Tb³⁺ ions cannot be applied strictly and no reliable prediction about the energy and composition of the unoccupied states above the Fermi level in TbNiSb is possible without having performed the corresponding many body calculations [231]. Nevertheless, it is clear that several different unoccupied states exist a few eV above the Fermi level having a different composition, and a separation of two principal spin states by one eV is typical. As mentioned above, table 6.2 gives a typical example, but the exact situation in TbNiSb is not known.

In the next step of the resonance process, this excited electron is deexcited under transferring its energy to a bound 4f electron which is subsequently emitted. It interacts with the spins and moments of the occupied 4f electrons and the quantum mechanical interferences with the direct photoemission process leads then to the Fano resonance. These interactions depend on the nature of excited states above the Fermi level as well as on the composition of the occupied Tb 4f in the valence band, thus favoring certain resonance channels at specific incident energies. As a result, some resonance channels show different partial cross sections depending on the final state configuration, ⁶I, ⁶P, ⁶D for the Tb 4f peak at 8.3 eV and ⁶G, ⁶F, ⁶H for the one at 9.7 eV. The key role might be attributed to the ⁶I configuration with the highest angular moment ($L = 6$), since only this final state shows a large magnetic circular dichroism (MCD) signal on remanently magnetized Tb(0001)/W(110) thin films, while the other states in the main 4f multiplet structure show hardly any variations in MCD [176, 232]. This then leads to a different relative weight of the channels involved and some of them show en-

hanced or decreased intensities while passing by different intermediate states. As shown clearly in figure 6.17, the partial cross section of one channel at 150 eV is more intense at the CIS profile taken at binding energies of 8.3 eV in comparison to the one taken at 9.7 eV. This observation would be consistent with an explanation that there is a strong excited 4f state at the beginning of the set of unoccupied 4f states, like for example a ${}^6\text{H}_{15/2}$ one. It could then favour at least one of the resonance channels originating from the ${}^6\text{I}$, ${}^6\text{P}$, ${}^6\text{D}$ states around 8.3 eV binding energy, possibly the ${}^6\text{I}$ configuration. In contrast, the resonances being emitted from the 9.7 eV states are favoured by the higher lying intermediate states, like for example the ${}^6\text{F}_{11/2}$, ${}^6\text{F}_{9/2}$ calculated for Tb-ions. These are situated at energies roughly one eV above the first, say ${}^6\text{H}_{15/2}$, state and thus their resonance threshold is increased by this value of roughly one eV. As there are several weak levels spread over a small energy range, their resonance channels are spread over a certain energy range, giving a broad distribution of resonances (≈ 151 -152 eV). Contrarily, a sharp strong resonance channel, probably a single one, occurs at the beginning of the resonance profile (≈ 150 eV), as clearly visible in the difference plot of figure 6.17.

Summarising this part, it can be identified that the resonance profile is a superposition of several different resonance channels, the resonance threshold of which is determined by the first step of the resonance mechanism, by the excitation of a 4d electron to excited intermediate states above the Fermi level. Some of the resonance channels have different partial cross sections, depending on the final state configuration of the peaks in the valence band, possibly dominated by the high angular momentum state ${}^6\text{I}$. This then leads to a configuration of unoccupied states above the Fermi edge, which might be principally similar to the one in Tb^{3+} ions. This interpretation is consistent with magnetic circular dichroism (MCD) results, where spectral changes are explained by the angular momentum dependence of the $4d^9 4f^{m+1}$ intermediate state [149]. However, no clear identification of the exact states and resonance channels can be done on the basis of the present data. For performing this task, many body calculations need to be carried out, specially adapted to this resonance problem in TbNiSb . In addition, spin resolved resonance measurements would provide valuable experimental data in order to investigate more closely this complex resonance mechanism [150, 233].

6.7 Conclusion

The analysis of the electronic structure with photoemission techniques, in connection with some theoretical simulations, allowed to gain further insight into the spectroscopic transitions and the mechanisms involved. Further, they provided crucial information necessary to interpret macroscopic results obtained by other characterisation techniques.

The electronic composition of the 4f wave functions was found to be similar to the one of rare earths metals with only small differences in the spectra which are attributed to chemical shifts, screening and hybridisation effects. As the principal spin and magnetic moment structure of the 4f shell varies little between different compounds with the same rare earth atom, existing data from the literature can be employed for the present rare earth compounds in order to support the analysis of physical effects, which are influenced by the special properties of the 4f shell. This similarity confirms the results obtained from elastic neutron scattering.

Band structure calculations resolved the convolution of the overlapping states at the Fermi level, revealing a clear hybridisation of the RE 5d 6s, Ni 3d and Sb 5p 5d states in the bands about 0.5 - 2 eV below the Fermi edge. The analysis supports that the crystal structure is stabilized by a sp^3 hybridisation around Sb as found earlier by the structure determination in chapter 2.3 and 2.4.

The slow decrease of the XPS intensity towards the Fermi level supports the observation from resistivity of narrow gap semiconductors, even if the energy gap cannot be determined experimentally by the XPS technique alone with its comparatively low experimental resolution. In turn, corresponding theoretical calculations of the electronic structure allow then to deconvolute the spectra and to resolve fine details, supplying so crucial information on the width of the gap, helping to identify the electrical transport mechanisms.

When the splitting Δ_{CEF} between the two lowest crystal field levels exceeds the experimental resolution, these levels become apparent in sufficiently well-resolved spectra [234], opening the possibility to use ultra high resolution photoemission [190] as a complementary tool to inelastic neutron scattering in the study of CEF levels. However, the experimental resolution of the photoemission data in the present work, did not allow to observe the CEF levels, identified by inelastic neutron scattering, from the electron spectroscopic point of view.

While some characterisation techniques probe the ground state proper-

ties, photoemission studies enabled to obtain further insight into the excited configurations, having so allowed to study the transitions occurring between the correlated unbalanced atomic shells. With the help of resonant photoemission, the strong interaction between the 4d and 4f subshell was reconfirmed. Some new details of the correlated many body processes could be resolved, leading to the qualitative identification of some resonance channels involved. The initial excitation step was found to govern the energy of the resonant threshold depending on the intermediate excited state above the Fermi edge. Further, the partial cross section of the resonance channels is influenced by the spin configuration of the final state reached in the valence band. Therefore, the variations in the CIS spectra could have been identified as due to passing by different intermediate $4d^9 4f^{(n+1)}$ states in the resonance mechanisms, which is consistent with magnetic circular dichroism (MCD) results, where the spectral changes were explained by the angular momentum dependence of the $4d^9 4f^{n+1}$ intermediate state [149].

However, despite of ongoing research and improving computation power, the existing theoretical models are not yet sufficient to describe completely the complexity of the many body processes occurring in the highly correlated 4f shell [235]. To date it is not yet possible to treat all fine details of the photoemission and resonance processes of rare earth compounds within the existing computation models [231], resulting in a sometimes poor matching of the experimental data with the theoretical simulations. As the photoemission and resonance spectra of compounds generally represent a complex convolution of many overlapping peaks, the lack of corresponding theoretical calculations, especially adapted to the present experimental problem, restricts then often the evaluation and interpretation of the experimental spectra to qualitative results, deduced by considering and analysing neighbouring existing data from the literature. For a closer understanding it would be useful to obtain additional experimental information, especially spin and/or angle (\vec{k}) resolved data, in order to gain further insight into the nature of these complex coupled processes which then in turn might lead to improved theoretical models.

Chapter 7

Conclusion and perspectives

In this thesis, rare earth compounds, especially the series of RNiSb (R=rare earth) compounds were investigated from various points of view in order to reveal the different energy scales involved in their physical properties.

The electronic structure of the atomic shells was investigated by the means of photoelectron spectroscopy, showing extended final state multiplets, split by around 30 eV for the 4d and up to 8 eV for the 4f final state multiplet provoked by the strong correlations between the created core level hole with the incomplete 4f shell. The valence band features were interpreted with the help of calculations of the partial density of states identifying so the contributions of R 4f 5d 6s, Ni 3d and Sb 5s 5p states. The energetic position of the 4f peaks suffers a small chemical shift around 0.2 eV in comparison with the pure RE metals towards higher binding energies due to the bonding with Sb. Through variations in the shape of the Fano-resonance profiles, taken at the $^8S_{7/2}$, ($^6I, ^6P, ^6D$) and ($^6G, ^6F, ^6H$) Tb peaks, different excitation and deexcitation channels were resolved and qualitatively identified related to unoccupied 4f states above the Fermi-level roughly one eV apart.

The DOS calculations revealed an intrinsic energy gap of around 200 meV in the heavy RNiSb semiconductors. However, resistivity measurements at temperatures between 200 and 300 K gave a gap of 20 to 80 meV related to donor/acceptor levels within the gap. Negative thermopower measurements at room temperature show that electrons are the dominant charge carriers in the investigated samples. By theoretical simulations, the conduction process was identified to be controlled by activation of these donor/acceptor states within the intrinsic gap. At low T, ρ is ruled by variable range hopping or conduction in an impurity band according to the density of impurity states. In these magnetic semiconductors, a giant magnetoresistance (GMR) was

discovered, reaching -50% under magnetic fields of 8 Tesla. The ruling mechanism was identified to be dominated by spin disorder scattering and described successfully by the polarization of impurity states by the 4f shell.

The series of RNiSb compounds reveals a wide range of magnetic properties ranging from paramagnets, ferromagnets, modulated structures to antiferromagnets where the magnetic couplings are in the order of up to 2 meV. In the light RNiSb compounds, the magnetic coupling takes place indirectly via the RKKY mechanism where the small wavevector k_F at the Fermi-level favours the observed ferromagnetic or modulated order. Contrarily, the heavy rare earth compounds order antiferromagnetically with a propagation vector $\vec{Q} = (\frac{1}{2}, \frac{1}{2}, \frac{1}{2})$ controlled by superexchange interactions, which are likely to be of short range, dominated by nearest neighbour interactions.

Neutron spectroscopy allowed to investigate the ground state of these systems arising from the splitting of the LSJ ground multiplet through magnetic interactions and the crystalline electric field (CEF) in the range from 0.1 to 10 meV. Calculations on the basis on the resolved crystalline electric field (CEF) scheme provided then the explanation for the observed direction and rotation of the magnetic moments between the fourfold and twofold crystal axes and the absence of magnetic order in certain configurations. Further, the simulation of the magnetic resistivity incorporating the CEF proved the Kondo effect to be present in CeNiSb. Finally, as the smallest investigated energy scale, the Kondo coupling in CeNiSb was determined to be about 0.5 meV from the inelastic neutron scattering experiments.

Further research could involve the following: As related compounds (e.g. CeSb, NiMnSb, PtMnSb) show a large magneto-optical Kerr effect [236], it would be interesting to investigate this behaviour also in RNiSb compounds. The Hall effect and thermoelectric power would give the sign of the charge carriers and specific heat measurements could provide the density of states at the Fermi level $n(E_F)$. The presented approach to identify the conduction mechanism and the amount of impurity states is not restricted to the presently investigated system. It may also be employed as a characterization method to analyse similar compounds and narrow gap magnetic semiconductors. Spin resolved resonant photoelectron spectroscopy measurements with high resolution could provide important additional information helping to describe more closely the resonance channels in these correlated compounds. In the case that single crystals of these compounds become available, it would be quite interesting to study anisotropy effects, and to perform angle resolved photoemission experiments in order to map their band structure.

Bibliography

- [1] Recommendation of the international union for pure and applied chemistry, 1968.
- [2] E. A. Nesbitt and J. H. Wernick. *Rare Earth Permanent Magnets*. Academic Press, New York, 1973.
- [3] A. E. Clark. High-field magnetization and coercivity of amorphous rare-earth-Fe₂ alloys. *Appl. Phys. Lett.*, 23(11):642–644, 1974.
- [4] T. Sakai, M. Matsuoka, and C. Iwakura. Rare earth intermetallics for metal-hydrogen batteries. In K. A. Gschneider Jr. and L. Eyring, editors, *Handbook on the Physics and Chemistry of Rare Earths*, volume 21, chapter 142, pages 133–178. North Holland Publishing Company, Amsterdam, 1995.
- [5] N. Imanaka G. Adachi. Chemical sensors. In K. A. Gschneider Jr. and L. Eyring, editors, *Handbook on the Physics and Chemistry of Rare Earths*, volume 21, chapter 143, pages 179–262. North Holland Publishing Company, Amsterdam, 1995.
- [6] M. J. Weber. Rare earth lasers. In K. A. Gschneider Jr. and L. Eyring, editors, *Handbook on the Physics and Chemistry of Rare Earths*, volume 4, chapter 35, pages 275–315. North Holland Publishing Company, Amsterdam, 1979.
- [7] K. A. Gschneider Jr. and L. Eyring. *Handbook on the Physics and Chemistry of Rare Earths (series)*, volume 1-22. North Holland Publishing Company, Amsterdam, 1978-1996.
- [8] K. N. R. Taylor. Intermetallic rare-earth compounds. *Advan. Phys.*, 20:551–660, 1971.
- [9] W. E. Wallace and E. Segal. *Rare Earth Intermetallics*. Academic Press, New York, 1973.

- [10] H. R. Kirchmayr and C. A. Poldy. Magnetic properties of intermetallic compounds of rare earth metals. In K. A. Gschneider Jr. and L. Eyring, editors, *Handbook on the Physics and Chemistry of Rare Earths*, volume 2, chapter 14, pages 55–230. North Holland Publishing Company, Amsterdam, 1979.
- [11] K. H. J. Buschow. Intermetallic compounds of rare earth and 3d-transition metals. *Rep. Prog. Phys.*, 40:1179–1256, 1977.
- [12] K. H. J. Buschow. Intermetallic compounds of rare earth and non-magnetic metals. *Rep. Prog. Phys.*, 42:1373–1477, 1979.
- [13] T. Kaneko. Magnetic properties of metals - compounds of rare earth elements with main group elements. In H. P. J. Wijn, editor, *Landolt-Börnstein - Numerical Data and Functional Relationships in Science and Technology - New Series*, volume III/19e1, chapter 2.6.2. Springer Verlag, Berlin, 1990. and references therein.
- [14] A. V. Postnikov, V. P. Antropov, and O. Jepsen. Electronic and magnetic structure of GdCu and GdZn. *J. Phys.: Condens. Matter*, 4:2475–2486, 1992.
- [15] R. E. Walline and W. E. Wallace. Magnetic and structural characteristics of lanthanide-copper compounds. *J. Chem. Phys.*, 42(2):604–607, 1962.
- [16] H. Yoshida, S. Abe, T. Kaneko, and K. Kamigaki. Pressure effect on the Néel temperature of GdCu, GdAg, and TbAg. *J. Magn. Magn. Mat.*, 70:275–276, 1987.
- [17] Y. Gefen and M. Rosen. Anomalous elasticity and anelasticity of GdCu at low temperatures. *J. Phys. Chem. Solids*, 42(9):857–860, 1981.
- [18] C. S. Garde, J. Ray, and G. Chandra. Electrical resistivity, thermopower and thermal conductivity studies of $(\text{Sm}_{1-x}\text{Y}_x)\text{Cu}_2$ and RCu_2 ($\text{R} \equiv \text{Gd}, \text{Pr}, \text{or Tb}$) systems. *J. Phys.: Condens. Matter*, 5:6737–6744, 1993.
- [19] H. Nakamura, Y. Kitaoka, H. Yamada, and K. Asayama. Discovery of antiferromagnetic ordering above upper critical field in the heavy fermion superconductor CeCu_2Si_2 . *J. Magn. Magn. Mat.*, 76-77:517–519, 1988.

- [20] J. J. Croat. Manufacture of Nd-Fe-B permanent magnets by rapid solidification. *J. Less Common Met.*, 148:7–15, 1989.
- [21] F. Heusler. *Verh. Dtsch. Ges.*, 5:219, 1903.
- [22] J. Pierre, P. Haen, C. Vettier, and S. Pujol. CeInCu₂ short range correlations or imperfect magnetic order? *Physica B*, 163(1-3):463–466, 1990.
- [23] A. M. Umarji, S. K. Malik, and G. K. Shenoy. Structural transformation studies on the rare earth containing Heusler alloys Pd₂RESn. *Solid State Communications*, 53(11):1029–1032, 1985.
- [24] J. L. Jorda, M. Ishikawa, and J. Muller. Phase equilibria and superconductivity in the Pd-Y-Sn system. *J. Less Common Met.*, 107:321–330, 1985.
- [25] J. Toboła, J. Pierre, S. Kaprzyk, R. V. Skolozdra, and M. A. Kouacou. Onset of weak itinerant ferromagnetism by doping a semiconducting Heusler phase. *J. Magn. Magn. Mat.*, 159:192, 1996.
- [26] J. Pierre, R. V. Skolozdra, S. Kaprzyk, C. Hordequin, M. A. Kouacou, I. Karla, R. Currat, and E. Lelièvre-Berna. Properties in request on semi-Heusler phases. *J. All. Comp.*, 262-263:101–107, 1997.
- [27] M. Kouacou. *Apparition du Ferromagnetisme itinerant dans des composés de type Heusler. Relation avec des transitions isolant-metal*. PhD thesis, Université Joseph Fourier, Grenoble 1, 1996.
- [28] J. Toboła, J. Pierre, S. Kaprzyk, R. V. Skolozdra, and M. A. Kouacou. Crossover from semiconductor to magnetic metal in semi-Heusler phases as a function of valence electron concentration. *J. Phys.: Condens. Matter*, 10:1013–1032, 1998.
- [29] R. A. de Groot and K. H. J. Buschow. Recent developments in half-metallic magnetism. *J. Magn. Magn. Mat.*, 54-57:1377–1380, 1986.
- [30] S. J. Youn and B. I. Min. Effects of the spin-orbit interaction in Heusler compounds: Electronic structures and Fermi surfaces of NiMnSb and PtMnSb. *Phys. Rev. B*, 51(16):10436–10422, 1995.
- [31] E. Kisker, C. Carbone, C. F. Flipse, and E. F. Wassermann. Photo-emission of intermetallics. *J. Magn. Magn. Mat.*, 70:21–27, 1987.

- [32] Ch. Hordequin. *Le demi-métal NiMnSb: Etude des propriétés magnétiques et de transport et réalisation de vannes de spin*. PhD thesis, Institut National Polytechnique de Grenoble, Grenoble, 1997.
- [33] Ch. Hordequin, J. Pierre, and R. Currat. Magnetic excitations in the half-metallic NiMnSb ferromagnet: from Heisenberg-type to itinerant behaviour. *J. Magn. Magn. Mat.*, 162:75–84, 1996.
- [34] Ch. Hordequin, E. Lelièvre-Berna, and J. Pierre. Magnetization density in the half-metallic ferromagnet NiMnSb. *Physica B*, 234-236:602–604, 1997.
- [35] V. K. Pecharski, Yu. V. Pankevich, and O. I. Bodak. Crystal structures of the compounds RNiSb with various rare earth elements. *Sov. Phys. Crystallogr.*, 28(1):97–98, 1983.
- [36] R. V. Skolozdra, Ja. F. Mikalski, K. Kaczmarek, and J. Pierre. CeCuSb₂ and CeNiSb: new exotic Kondo systems. *J. All. Comp.*, 206:141–146, 1994.
- [37] L. Menon and S. K. Malik. Ferromagnetic Kondo lattice behaviour in CeNiSb. *Phys. Rev. B*, 52(1):35–52, 1995.
- [38] L. Menon, S. K. Dhar, S. K. Malik, and W. B. Yelon. Search for hybridization gap in the electronic density of states in CeNiSb. *J. Appl. Phys.*, 79(8):6367–6369, 1996.
- [39] S. K. Dhar, S. Ramakrishnan, R. Vijayaraghavan, G. Chandra, K. Satoh, J. Itoh, Y. Onuki, and K. A. Gschneidner Jr. Magnetic behaviour of YbNiSb. *Phys. Rev. B*, 49(1):641–643, 1994.
- [40] G. LeBras, P. Bonville, J. A. Hodges, J. Hammann, M. J. Besnus, G. Schmerber, S. K. Dhar, F. G. Aliev, and G. Anfré. Local symmetry lowering in the cubic intermetallics YbPdBi and YbNiSb. *J. Phys.: Condens. Matter*, 7:5665–5680, 1995.
- [41] K. Hartjes and W. Jeitschko. Crystal structures and magnetic properties of lanthanoid nickel antimonides LaNiSb (Ln=La-Nd,Sm,Gd-Tm,Lu). *J. All. Comp.*, 226:81–86, 1995.
- [42] R. V. Skolozdra, A. Guzik, A. M. Goryn, and J. Pierre. Magnetic and transport properties of RNiSb compounds (R=Gd,Tb,Dy,Yb,Lu). *Acta Phys. Pol. A*, 92(2):343–6, 1997.

- [43] I. Karla, J. Pierre, and R. V. Skolozdra. Physical properties and giant magnetoresistance in RNiSb compounds. *J. All. Comp.*, 265:42–48, 1998.
- [44] I. Karla, J. Pierre, and B. Ouladdiaf. Magnetic structures of RNiSb compounds (R=rare earth) investigated by neutron diffraction. *Physica B*, 253:215–221, 1998.
- [45] I. Karla, J. Pierre, A. P. Murani, and M. Neumann. Crystalline electric field in RNiSb compounds investigated by inelastic neutron scattering. *Physica B*, in print, 1999.
- [46] J. Pierre, I. Karla, and K. Kaczmarek. Giant magnetoresistance in Heusler-type rare earth and 3d semiconductors. *Physica B*, 259–261:845–846, 1999.
- [47] D. X. Li, Y. Haga, Y. S. Kwon, H. Shida, T. Suzuki, S. Nimori, and G. Kido. Resistivity and hall effect of Gd and TmSb. *J. Magn. Magn. Mat.*, 140–144:1165–1166, 1995.
- [48] A. J. Neville, B. D. Rainford, D. T. Adroja, and H. Schober. Anomalous spin dynamics of CePdSb. *Physica B*, 223&224:271–274, 1996.
- [49] A. K. Solanki, A. Kashyap, S. Auluck, and M. S. S. Brooks. Band structure calculations of heavy fermion YbSbPd and YbSbNi. *J. Appl. Phys.*, 75(10):6301–6302, 1994.
- [50] D. T. Adroja, B. D. Rainford, A. J. Neville, P. Mandal, and A. G. M. Jansen. A comparative study of suppression of the energy gap with La substitution in the Kondo insulators: CeNiSn and CeNiSb. *J. Magn. Magn. Mat.*, 161:157–168, 1996.
- [51] B. D. Rainford, D. T. Adroja, A. Neville, and D. Fort. Spin dynamics and crystal fields of CePdSb. *Physica B*, 206&207:209–211, 1995.
- [52] Y. Bando, T. Takabatake, H. Fujii, and G. Kido. Suppression of the energy gap in CeRhSb by partial substitution of Pd for Rh. *Physica B*, 206&207:822–824, 1995.
- [53] T. Hiraoka, N. Kitaguchi, Y. Okayama, Y. Bando, and H. Jujii T. Takabatake. Suppression of the Hall effect and electrical resistivity in the CeRh_{1-x}Pd_xSb system. *Physica B*, 239:101–103, 1997.
- [54] B. D. Rainford and D. T. Adroja. Structural and magnetic properties of hexagonal CePtSb. *Physica B*, 194–196:365–366, 1994.

- [55] K. H. J. Buschow. Hydrogen absorption in intermetallic compounds. In K. A. Gschneider Jr. and L. Eyring, editors, *Handbook on the Physics and Chemistry of Rare Earths*, volume 6, chapter 47, pages 1–112. North Holland Publishing Company, Amsterdam, 1984.
- [56] M. A. Rudermann and C. Kittel. *Phys. Ref.*, 96:99, 1954.
- [57] T. Kasuya. A theory of metallic ferro and antiferromagnetism on Zener's model. *Progr. Theor. Phys. (Kyoto)*, 16(1):45–57, 1956.
- [58] K. Yosida. Magnetic properties of Cu-Mn alloys. *Phys. Rev.*, 106(5):893–898, 1957.
- [59] A. V. Postnikov. private communication, 1999.
- [60] D. A. Liberman, D. T. Cromer, and J. T. Waber. *Comp. Phys. Commun.*, 2:107, 1971.
- [61] H. Kadomatsu, M. Kurisu, and H. Fujiwara. Structural phase transitions in CsCl-type RM compounds ($R=\text{La, Ce, Pr, Nd}$; $M=\text{Ag, Cd, Ti}$). *J. Phys. F: Met. Phys.*, 17:L305–L309, 1987.
- [62] Y. Gefen and M. Rosen. On the nature of the hysteretic behaviour in GdCu compound. *Scripta Metallurgica*, 14:645–648, 1980.
- [63] J. C. M. van Dongen, T. T. M. Palstra, A. F. J. Morgowink, J. A. Mydosh, B. M. Geerken, and K. H. J. Buschow. Crystal-structure transformation and magnetic-ordering phenomena in $\text{GdCu}_{1-x}\text{Ga}_x$. *Phys. Rev. B*, 27(3):1887–1902, 1993.
- [64] A. Chelkowski, E. Talik, J. Heimann, and J. Szade. Magnetic susceptibility of RCu and $\text{R}_{0.5}\text{Gd}_{0.5}\text{Cu}$ ($R = \text{Tb, Dy, Ho, Er and Gd}$). *Physica B*, 130:231–232, 1985.
- [65] W. G. Moffatt. *The Handbook of Binary Phase Diagrams*. Genium Publishing Corporation, Schenectady, 1992.
- [66] J. S. Abell. Preparation and crystal growth of rare earth elements and intermetallic compounds. In K. A. Gschneider Jr. and L. Eyring, editors, *Handbook on the Physics and Chemistry of Rare Earths*, volume 12, chapter 80, pages 1–52. North Holland Publishing Company, Amsterdam, 1989.

- [67] A. E. Dwight. Alloying behaviour of zirconium, hafnium and the actinides in several series of isostructural compounds. *J. Less Common Met.*, 34(2):279–284, 1974.
- [68] A. R. Storm and K. B. Benson. Lanthanide-copper intermetallic compounds having the CeCu_2 and AlB_2 structures. *Acta Cryst.*, 16:701–702, 1963.
- [69] J. I. Langford and D. Louer. Powder diffraction. *Rep. Prog. Phys.*, 59(2):131–234, 1996.
- [70] L. V. Azaroff and M. J. Buerger. *The powder method in X-ray crystallography*. McGraw-Hill Book Co., New York, 1958.
- [71] G. Bacon. *Neutron Diffraction*. Clarendon Press, Oxford, 1975.
- [72] D. Gignoux and D. Schmitt. Magnetism of compounds of rare earths with non-magnetic metals. In K. H. J. Buschow, editor, *Handbook of Magnetic Materials*, volume 10, chapter 2, pages 239–413. Elsevier Science, Amsterdam, 1997.
- [73] J. Pierre. Magnetism of rare earth metals and intermetallic compounds. In M. Cyrot, editor, *Magnetism in Metals and Alloys*, pages 245–293. North Holland, Amsterdam, 1982.
- [74] Aimé Magre. *Magnétisme - fondements, matériaux et applications*. Grenoble Sciences, Grenoble, 1998.
- [75] K. Kaczmarek, J. Pierre, and A. Guzik. Magnetic and resistivity studies of GdNi_2Sn_2 , GdCu_2Sn_2 and GdNi_2Sb_2 compounds. *J. All. Comp.*, 219:208–210, 1995.
- [76] S. Baran, J. Leciejewicz, N. Stüsser, A. Szytula, A. Zygmunt, and V. Ivanov. Magnetic properties of PrPdSb and NdPdSb compounds. *J. Phys.: Condens. Matter*, 8:8397–8405, 1996.
- [77] G. André, F. Bourée, A. Olés, W. Sikora, S. Baran, and A. Szytula. Magnetic structures of HoPdSb compound. *Solid State Communications*, 104(9):531–4, 1997.
- [78] A. Szytula, B. Penc, and E. Ressouche. Magnetic structures of DyNiSn and TbRhSn . *J. All. Comp.*, 244:94–98, 1996.
- [79] R. M. White. *Quantum Theory of Magnetism*. Mc. Graw - Hill Book Company, New York, 1970.

- [80] A. Herpin. *Théorie du Magnétisme*. Presses Universitaires de France, Paris, 1968.
- [81] Laboratoire Louis Néel CNRS UJF. Magnétisme pratique et magnétométrie. Grenoble, 1998.
- [82] H. G. Büttner, E. Lelievre-Berna, and F. Pinet. *Guide to Neutron Research Facilities at the ILL*. Institute Laue Langevin, Grenoble, 1997.
- [83] J. Rodríguez-Carvajal. Recent advances in magnetic structure determination by neutron powder diffraction. *Physica B*, 192:55–69, 1993.
- [84] N. F. M. Henry and K. Lonsdale. *International tables for X-ray crystallography*. The Kynoch Press, Birmingham, 1969.
- [85] G. André, F. Bourée, A. Olés, W. Sikora, A. Szytuła, and A. Zygmunt. Magnetic ordering of RNiSb_2 ($\text{R}=\text{Pr}$, Nd and Tb) compounds studied by neutron diffraction and magnetic measurements. *J. All. Comp.*, 255:31–42, 1997.
- [86] F. Hulliger. Rare earth pnictides. In K. A. Gschneider Jr. and L. Eyring, editors, *Handbook on the Physics and Chemistry of Rare Earths*, volume 4, chapter 33, pages 153–236. North Holland Publishing Company, Amsterdam, 1979.
- [87] P. Morin, J. Pierre, and J. Chaussy. Specific heat in TbZn and HoZn compounds. *Phys. Stat. Sol. A*, 24(2):425–432, 1974.
- [88] P. Morin and D. Schmitt. Quadrupolar interactions and magneto-elastic effects in rare earth intermetallic compounds. In K. H. Buschow and E. P. Wohlfarth, editors, *Ferromagnetic materials*, volume 5, pages 1–132. Elsevier Science, Amsterdam, 1990. and references therein.
- [89] P. L. Rossiter. *The electrical resistivity of metals and alloys*. Cambridge University Press, Cambridge, 1987.
- [90] P. Leroux-Hugon. Session 6: Transport properties and semiconductor-metal transitions; transport properties of magnetic semiconductors: The weak coupling situation. *J. Magn. Magn. Mat.*, 3:165–175, 1976.
- [91] E. Gratz and M. J. Zuckermann. Transport properties (electrical resistivity, thermoelectric power and thermal conductivity) of rare earth

- intermetallic compounds. In K. A. Gschneider Jr. and L. Eyring, editors, *Handbook on the Physics and Chemistry of Rare Earths*, volume 5, chapter 42, pages 117–216. North Holland Publishing Company, Amsterdam, 1982.
- [92] S. von Molnar and S. Methfessel. Giant negative magnetoresistance in ferromagnetic $\text{Eu}_{1-x}\text{Gd}_x\text{Se}$. *J. Appl. Phys.*, 38(3):959–964, 1967.
- [93] Y. Shapira, S. Foner, and T. B. Reed. EuO. I. resistivity and Hall effect in fields up to 150 kOe. *Phys. Rev. B*, 8(5):2299–2315, 1973.
- [94] Y. Shapira, S. Foner, R. L. Aggarwal, and T. B. Reed. EuO. II. dependence of the insulator-metal transition on magnetic order. *Phys. Rev. B*, 8(5):2316–2326, 1973.
- [95] M. R. Oliver, J. A. Kafalas, J. O. Dimmock, and T. B. Reed. Pressure dependence of the electrical resistivity of EuO. *Phys. Rev. Lett*, 24(9):1064–1067, 1970.
- [96] M. R. Oliver, J. O. Dimmock, A. L. Mc Whorter, and T. B. Reed. Conductivity studies in europium oxide. *Phys. Rev. B*, 5(3):1078–1098, 1972.
- [97] Y. Shapira and R. L. Kautz. Effect of spin splitting of the conduction band on the resistivity and Hall coefficient: Model for the positive magnetoresistance in EuSe. *Phys. Rev. B*, 10(11):4781–4794, 1974.
- [98] J. Stankiewicz, S. von Molnar, and F. Holtzberg. Magneto-transport and the insulator-metal transition in the magnetic semiconductor EuTe. *J. Magn. Magn. Mat.*, 54-57:1217–1218, 1986.
- [99] S. Jin, T. H. Tiefel, M. McCormack, R. A. Fastnacht, R. Ramesh, and L. H. Chen. Thousandfold change in resistivity in magnetoresistive La-Ca-Mn-O films. *Science*, 264:413–415, 1994.
- [100] H. Kuwahra, Y. Tomioka, Y. Moritomo, A. Asamitsu, and Y. Tokura. M. Kasai, R. Kumai. Striction-coupled magnetoresistance in perovskite-type manganese oxides. *Science*, 272:80–82, 1996.
- [101] A. J. Dekker. *Solid State Physics*. Prentice-Hall Inc., Englewood-Cliffs, 1957.
- [102] E. Grüneisen. *Ann. Phys.*, 16:530, 1933.

- [103] E. H. Putley. *The Hall effect and related phenomena*. Butterworths, London, 1960.
- [104] T. G. Castner. Hopping conduction in the crytical regime approaching the metal-insulator transition. In M. Pollak and B. Shklovskii, editors, *Hopping transport in solids*, chapter 1, pages 1–47. North-Holland, Amsterdam, 1991.
- [105] N. F. Mott. *Metal-insulator transitions*. Taylor & Francis, London, 1990.
- [106] P. W. Anderson. Absence of diffusion in certain random lattices. *Phys. Rev*, 109(5):1492–1505, 1958.
- [107] N. F. Mott. The electrical properties of liquid mercury. *Phil. Mag.*, 13:989–1014, 1966.
- [108] P. G. de Gennes and J. Friedel. Anomalies de résistivité dans certains métaux magnétiques. *J. Phys. Chem. Solids*, 4:71–77, 1958.
- [109] O. Redon. *Comportements magnétiques dans les systèmes multicouches et granulaires Ag/FeNi et Ag/FeCo pour le développement de capteurs magnétoresistifs*. PhD thesis, Université Joseph Fourier, Grenoble 1, 1984.
- [110] N. Sato, H. Mori, H. Yashima, T. Satoh, and H. Takei. Anisotropic Fermi-liquid behaviour of the Ce-Si system. *Solid State Communications*, 51(3):139–142, 1984.
- [111] L. Chioncel. private communication, 1999.
- [112] M. Kohler. *Ann. Phys.*, 6(18):107, 1949.
- [113] P. Majumdar and P. Littlewood. Magnetoresistance in Mn pyrochlore: Electrical transport in low carrier density ferromagnet. *Phys. Rev. Lett*, 81(6):1314–1317, 1998.
- [114] T. Kasuya and A. Yanase. Anomalous transport phenomena in Eu-clalcogenide alloys. *Rev. Mod. Phys.*, 40(4):684–696, 1968.
- [115] M. T. Hutchings. Point-charge calculation of energy levels of magnetic ions in crystalline electric fields. *Sol. Stat. Phys.*, 16:227–273, 1964.

- [116] P. Fulde. Crystal fields. In K. A. Gschneider Jr. and L. Eyring, editors, *Handbook on the Physics and Chemistry of Rare Earths*, volume 2, chapter 17, pages 295–386. North Holland Publishing Company, Amsterdam, 1979.
- [117] A. Furrer. *Crystal Field Effects in Metals and Alloys*. Plenum Press, New York, 1977.
- [118] B. Bleaney and K. W. H. Stevens. Paramagnetic resonance. *Rept. Progr. Phys.*, 16:108–159, 1953.
- [119] A. J. Freeman and R. E. Watson. Theoretical investigation of some magnetic and spectroscopic properties of rare-earth ions. *Phys. Rev.*, 127(6):2058–2075, 1962.
- [120] K. W. H. Stevens. *Proc. Phys. Soc. A*, 65:209, 1952.
- [121] C. Cohen-Tannoudji, B. Diu, and F. Laloë. *Mécanique Quantique*. Hermann, Paris, 1977.
- [122] K. R. Lea, M. J. M. Leask, and W. P. Wolf. The raising of angular momentum degeneracy of f-electron terms by cubic crystal fields. *J. Phys. Chem. Solids*, 23:1381–1405, 1962.
- [123] U. Walter. Treating crystal field parameters in lower than cubic symmetries. *J. Phys. Chem. Solids*, 45(4):401–408, 1984.
- [124] R. J. Birgeneau. Transition probabilities for f-electron J-multiplets in cubic crystal fields. *J. Phys. Chem. Solids*, 33:59–68, 1972.
- [125] R. Scherm. Fundamentals of neutron scattering by condensed matter. *Ann. Phys.*, 7(5):349–370, 1972.
- [126] U. Walter and E. Holland-Moritz. Crystal field parameters and crystal field linewidths in the REYPd₃ and REYAl₂ alloys. *Z. Phys. B*, 45:107–112, 1981.
- [127] A. Ślebarski, A. Jezierski, and A. Zygmunt. Effect of alloying the electronic structure in CeNiSn. *Phys. Rev. B*, 54:13551–13557, 1996.
- [128] B. Cornut and B. Coqblin. Influence of the crystalline field on the Kondo effect of alloys and compounds with cerium impurities. *Phys. Rev. B*, 5(11):4541–4561, 1972.

- [129] M. Garnier, D. Purdie, K. Breuer, M. Hengsberger, and Y. Baer. Momentum-resolved photoemission of the Kondo peak in an ordered Ce-containing alloy. *Phys. Rev. B*, 56(18):R11399–R11402, 1997.
- [130] A. Ślebarski, A. Jezierski, S. Mähl, M. Neumann, and G. Borstel. Influence of the Kondo-hole impurities on the electronic structure of CeNiSn and CeRhSb. *Phys. Rev. B*, 58(8):4367–4371, 1998.
- [131] M. Cyrot. *Magnetism in Metals and Alloys*. North Holland, Amsterdam, 1982.
- [132] J. H. van Vleck. *The Theory of Electric and Magnetic Susceptibilities*. Oxford University Press, Oxford, 1932.
- [133] R. J. Kappert, H. R. Borsje, and J. C. Fugge. High energy spectroscopies and magnetism. *J. Magn. Magn. Mat.*, 100:363–393, 1991.
- [134] F. Gerken, A.S.Flodström, J. Barth, L. I. Johansson, and C. Kunz. Surface core level shifts of the lanthanide metals Ce⁵⁸ – Lu⁷¹: A comprehensive experimental study. *Physica Scripta*, 32:43–57, 1985.
- [135] E. Weschke, C. Laubschat, A. Höhr, K. Starke, E. Navas, L. Baumgarten, A. V. Fedorov, and G. Kaindl. Electronic and magnetic structure of rare-earth materials studied by high-resolution photoemission. *J. Electron Spectrosc. Relat. Phenom.*, 68:515–524, 1994.
- [136] F. P. Netzer and J. A. D. Matthew. Surfaces on rare earth metals. *Rep. Prog. Rhys.*, 49:621–681, 1986.
- [137] D. Li, J. Zhang, P. A. Dowben, and M. Onellion. Altering the Gd(0001) surface electronic structure with hydrogen adsorption,. *Phys. Rev. B*, 48(8):5612–5620, 1993.
- [138] H. Hertz. Über den Einfluß des ultravioletten Lichtes auf die elektrische Entladung. *Wiedemannsche Ann.*, 31:983–1000, 1888.
- [139] A. Einstein. Über einen die Erzeugung und Verwandlung des Lichtes betreffenden heuristischen Gesichtspunkt. *Ann. Phys.*, 17:132–148, 1905.
- [140] M. F. Ebel. Röntgenphotoelektronenspektrometrie. In F. H. W. Heuck and E. Macherauch, editors, *Forschung mit Röntgenstrahlung, Bilanz eines Jahrhunderts (1895-1995)*. Springer Verlag, Berlin, 1995.

- [141] H. P. Bonzel and Ch. Klient. On the history of photoemission. *Progress in Surface Science*, 49(2):107–153, 1995.
- [142] Y. Baer and W.-D. Schneider. High-energy spectroscopy of lanthanide materials - an overview. In K. A. Gschneider Jr. and L. Eyring, editors, *Handbook on the Physics and Chemistry of Rare Earths*, volume 10, chapter 62, pages 1–73. North Holland Publishing Company, Amsterdam, 1987.
- [143] S. H. Liu. Electronic structure of rare earth metals. In K. A. Gschneider Jr. and L. Eyring, editors, *Handbook on the Physics and Chemistry of Rare Earths*, volume 1, chapter 3, pages 233–335. North Holland Publishing Company, Amsterdam, 1978.
- [144] S. D. Barrett. Angle-resolved photoemission and LEED from rare-earth metals. *Surface Science Reports*, 14:271–354, 1992.
- [145] W. Lenth, F. Lutz, J. Barth, and G. Kalkoffen. Giant resonance enhancement of the 4f, 5p, and 5s states in the photoemission spectra of rare-earth compounds. *Phys. Rev. Lett*, 41(17):1185–1188, 1978.
- [146] M. Meyer, Th. Prescher, E. von Raven, M. Richter, E. Schmidt, B. Sonntag, and H. E. Wetzel. Decay channels of core excitation resonances in 3d and 4f metal atoms. *Z. Phys. D - Atoms, Molecules and Clusters*, 2:347–362, 1986.
- [147] M. Richter, M. Meyer, M. Pahler, T. Prescher, E. v. Raven, B. Sonntag, and H. E. Wetzel. Experimental study of atomic 4d giant resonances by photoabsorption and photoelectron spectroscopy: Sm, Eu, and Gd. *Phys. Rev. A*, 40(12):7007–7019, 1989.
- [148] J. A. Scarfe, A. R. Law, H. P. Hughes, J. A. C. Bland, G. M. Roe, and A. P. Walker. Resonant photoemission from Gd on Cu(100). *Phys. stat. sol. (b)*, 17:377–392, 1992.
- [149] K. Starke, E. Navas, E. Arenholz, Z. Hu, L. Baumgarten, G. van der Laan, and C. T. Chen. Magnetic circular dichroism in 4d→4f resonant photoemission and photoabsorption of Gd metal. *Phys. Rev. B*, 55(4):2672–2675, 1997.
- [150] T. Kachel, R. Rochow, W. Gudat, R. Jungblut, O. Rader, and C. Carbone. Spin-resolved-photoemission-spectroscopy study of the giant resonance in Gd overlayers on Fe(100). *Phys. Rev. B*, 45(13):7267–7271, 1992.

- [151] S. Kimura, F. Arai, Y. Tezuka, S. Shin, S. Kunii, T. Suzuki, and M. Ikezawa. Resonant photoelectron spectra of Gd compounds. *Physica B*, 186-188:89–91, 1993.
- [152] V. Murgai, Young-Sea Huang, M. L. denBoer, and S. Horn. 5p-5d resonance in Gd. *Solid State Communications*, 66(4):329–332, 1988.
- [153] P. A. Dowben, Dongqi Li, Jiandi Zhang, and M. Onellion. Resonant photoemission studies of the thickness dependence of the unoccupied Gd 5d bands. *J. Vac. Sci. Technol. A*, 13(3):1549–1552, 1995.
- [154] F. Friedman, C. Carbone, K. A. Bertness, and I. Lindau. Resonant photoemission at the 5p threshold in La, Pr, Sm and Tb. *J. Electron Spectrosc. Relat. Phenom.*, 41:59–66, 1986.
- [155] P. A. Dowben, D. La Graffe, and M. Onellion. Final state symmetry effects in photoemission of thin Gd overlayers. *J. Phys.: Condens. Matter*, 1:6571–6587, 1989.
- [156] C. Laubschat, E. Weschke, G. Kalkowski, and G. Kaindl. 3d→4f resonant photoemission in rare earth systems. *Physica Scripta*, 41:124–129, 1990.
- [157] M. Kai, A. Tanaka, and T. Jo. Selection rules in resonant 4f photoemission for rare earth. *J. Phys. Soc. Jpn.*, 64(7):2356–2359, 1995.
- [158] M. F. López and G. Gutiérrez. Spectator states in 3d→4f resonant photoemission of Eu and Gd metal. *J. Phys.: Condens. Matter*, 9:6113–6118, 1997.
- [159] J. Sugar. Potential-barrier effects in photoabsorption. II. interpretation of photoabsorption resonances in lanthanide metals at the 4d-electron threshold. *Phys. Rev. B*, 5(5):1785–1792, 1972.
- [160] L. C. Davis. Photoemission from transition metals and their compounds. *J. Appl. Phys.*, 59(6):R25–R63, 1986.
- [161] A. Tanaka and T. Jo. Resonant 3d, 3p and 3s photoemission in transition metal oxides predicted at the 2p threshold. *J. Phys. Soc. Jpn.*, 63:2788–2807, 1994.
- [162] D. W. Schneider, F. Patthey, M. H. Schaffner, and B. Delley. Fano Resonanz in der Photoemission. *Deutsche Physikalische Gesellschaft, Frühjahrstagung, Münster*, 1999.

- [163] J. C. Ashley. Interaction of low-energy electrons with condensed matter: Stopping powers and inelastic mean free paths from optical data. *J. Electron Spectrosc. Relat. Phenom.*, 46:199–214, 1988.
- [164] M. Inokuti. Inelastic collisions of fast particles with atomic and molecules - the Bethe theory revisited. *Rev. Mod. Phys.*, 43(3):297–347, 1971.
- [165] G. Krill. X-ray and ultraviolet photoemission spectroscopy. Theory and applications. In J. Bruchel J. L. Hodeau M. S. Lehmann J. R. Regnard C. S. Schlenker, editor, *HERCULES - Neutron and Synchrotron Radiation for Condensed Matter Studies*, volume 1, chapter 16, pages 373–398. Les Editions de Physique, Les Ulis, 1993.
- [166] L. Ley and M. Cardona, editors. *Photoemission in Solids II*. Springer Verlag, Heidelberg, 1979.
- [167] S. Hüfner. *Photoelectron Spectroscopy, Principles and Applications*. Springer Verlag, Berlin, 1995.
- [168] S. D. Kevan. *Angle-Resolved Photoemission, Theory and Current Applications*. Elsevier Science, Amsterdam, 1992.
- [169] M. Wöhlecke, A. Baalmann, and M. Neumann. Zero-slope points and energy bandmapping. *Solid State Communications*, 49(3):217–221, 1984.
- [170] A. Baalmann, M. Neumann, W. Braun, and W. Radlik. Direct experimental determination of the dispersion of a final state energy band. *Solid State Communications*, 54(7):583–586, 1985.
- [171] Y. Petroff and P. Thiry. Angle resolved photoemission in solids. *Applied Optics*, 19(23):3957–3963, 1980.
- [172] J. C. Fuggle. Photoemission and absorption spectroscopy of solids and interfaces with synchrotron radiation. In R. Rosei, editor, *Proc. Intern. School of Physics 'Enrico Fermi'*, Amsterdam, 1990. North Holland.
- [173] R. L. Martin and D. A. Shirley. *Electron Spectroscopy: Theory Techniques and Applications*, volume 1. Academic Press, 1977.
- [174] G. Borstel. Theoretical aspects of photoemission. *Appl. Phys. A*, 38:193–204, 1985.
- [175] J. Lachnitt. Program simpeak. Universität Osnabrück, 1996.

- [176] E. Arenholz. *Magnetic Dichroism in Photoemission from Lanthanide Materials: Basic Concepts and Applications*. Wissenschaft und Technik Verlag, Berlin, 1996.
- [177] J. Szade, J. Lachnitt, and M. Neumann. High-resolution Gd 4f photoemission from different intermetallic compounds. *Phys. Rev. B*, 55(3):1430–1434, 1997.
- [178] G. van der Laan, E. Arenholz, E. Navas, A. Bauer, and G. Kaindl. Magnetic circular dichroism and orbital momentum coupling in 4d photoemission from Gd(0001). *Phys. Rev. B, Rapid Comm.*, 53(10):R5998–R6001, 1996.
- [179] H. Ebert. Fully relativistic treatment of core states for spin dependent potential. *J. Phys.: Condens. Matter*, 1(46):9111–9116, 1989.
- [180] Yu. M. Yarmoshenko, M. I. Katsnelson, E. I. Shreder, E. Z. Kurmaev, A. Ślebarski, S. Plogmann, T. Schlathölter, J. Braun, and M. Neumann. Observation of magnetic splitting in XPS MnL-spectra of Co₂MnSn and Pd₂MnSn Heusler alloys. *Eur. Phys. J. B*, 2:1–3, 1998.
- [181] F. Gerken, J. Barth, and C. Kunz. Exited multiplet lines in resonant photoemission spectra of Gd. *Phys. Rev. Lett*, 47:993–997, 1981.
- [182] F. Gerken. *Photoemission an den Seltenen Erdmetallen Cer bis Lutetium im Energiebereich von 20 bis 200 eV*. PhD thesis, Universität Hamburg, 1982.
- [183] U. Fano. Effects of configuration interaction on intensities and phase shifts. *Phys. Rev.*, 124(6):1866–1878, 1961.
- [184] L. C. Davis and L. A. Feldkamp. Interaction of many discrete states with many continua. *Phys. Rev. B*, 15(6):2961–2969, 1977.
- [185] A. F. Starace. Behavior of partial cross sections and branching ratios in the neighborhood of a resonance. *Phys. Rev. A*, 16(1):231–242, 1977.
- [186] F. Combet-Farnoux. Multichannel scattering theory of the resonant auger effect in photoelectron spectroscopy. *Phys. Rev. A*, 25(1):287–303, 1982.
- [187] N. Orlowski, C. Janowitz, A. Müller, R. Manzke, B. J. Kowalski, and B. A. Orlowski. Resonant photoemission study of Sn_{0.96}Gd_{0.04}Te. *Acta Phys. Pol. A*, 91(5):847–850, 1997.

- [188] T. Albers. *Untersuchung ionenstoßinduzierter Effekte bei der Tiefenprofilanalyse an oxidischen Multischichtsystemen mittels der Röntgenphotoelektronenspektroskopie*. Verlag Shaker, Aachen, 1994.
- [189] D. Raoux. Introduction to synchrotron radiation and the physics of storage rings. In J. Bruchel, J. L. Hodeau, M. S. Lehmann, J. R. Regnard, and C. S. Schlenker, editors, *HERCULES, Neutron and Synchrotron Radiation for Condensed Matter Studies*, volume 1, chapter II, pages 37–78. Les Editions de Physique, Les Ulis, 1993.
- [190] G. Kaindl, K. Schulz, P. A. Heimann, J. D. Bozek, and A. S. Schlachter. Ultra-high resolution in the soft X-ray region at beamline 9.0.1 at the ALS. *Synchrotron Radiation News*, 8(5):29–32, 1995.
- [191] R. W. Tank, O. Jepsen, A. Burkhardt, and O. K. Andersen. *The Stuttgart TB-LMTO-ASA program, Version 47*. Max-Planck-Institut für Festkörperforschung, Stuttgart, Germany, 1998.
- [192] U. von Barth and L. Hedin. A local exchange-correlation potential for the spin polarized case: I. *J. Phys. C: Solid State Phys.*, 5:1629–1642, 1972.
- [193] E. Weschke, C. Schüssler-Langeheine, R. Meier, A. V. Fedorov, K. Starke, F. Hübinger, and G. Kaindl. Temperature dependence of the exchange splitting of the surface state on Gd(0001): Evidence against spin mixing behaviour. *Phys. Rev. Lett*, 77(16):3415–3418, 1996.
- [194] W. Schneider, Th. Gantz, M. Richter, S. L. Molodtsov, J. Boysen, P. Engelmann, P. Segovia-Cabrero, and C. Laubschat. Angle-resolved photoemission study of Dy/Pd(111) and Ce/Pd(111) surface compounds. *Surface Science*, 377-379:275–278, 1997.
- [195] H. Kumigashira, S. H. Yang, T. Yokoya, A. Chainani, T. Takahashi, A. Uesawa, T. Suzuki, O. Saki, and Y. Kaneta. High-resolution angle-resolved photoemission spectroscopy of CeBi. *Phys. Rev. B*, 54(13):9341–9345, 1996.
- [196] A. Baalmann. *Experimentelle Bestimmung der Bandstruktur von Kupfer mittels anregungsenergieabhängiger Photoemission*. PhD thesis, University of Osnabrück, 1986.
- [197] E. Arenholz, E. Navas, K. Baumgarten, and G. Kaindl. Magnetic circular dichroism in core-level photoemission from Gd, Tb and Dy in ferromagnetic materials. *Phys. Rev. B*, 51(10):8211–8220, 1995.

- [198] B. J. Beaudry and K. A. Gschneider. Preparation and basic properties of the rare earth metals. In K. A. Gschneider Jr. and L. Eyring, editors, *Handbook on the Physics and Chemistry of Rare Earths*, volume 1, chapter 2, pages 173–232. North Holland Publishing Company, Amsterdam, 1978.
- [199] W. Junrong and R. T. Simonoson. The ultraviolet photoemission spectroscopic study of the reaction of rare-earth-metal gadolinium Gd(0001) with oxygen and water. *Vacuum Science and Technology*, 12(5):397–402, 1992.
- [200] S. Poulston, P. M. Parlett, P. Stone, and M. Bowker. Surface oxidation and reduction of CuO and Cu₂O studied using XPS and XAES. *Surface & interface analysis*, 24(12):811–820, 1996.
- [201] G. Atkinson, S. Coldrick, J. P. Murphy, and N. Taylor. Hydrogen and deuterium adsorption and absorption by rare earth metals. *J. Less Common Met.*, 49:439–450, 1976.
- [202] J. Szade, G. Skorek, and M. Neumann. Electronic structure and magnetism of Gd intermetallics. *Graduiertenkolleg, University of Osnabrück*, 24.11.1998.
- [203] R. Magri, S.-H. Wei, and A. Zunger. Ground-state structures and the random-state energy of the madelung lattice. *Phys. Rev. B*, 42(17):11388–11391, 1990.
- [204] R. J. Cole, N. J. Brooks, and P. Weightman. Determination of charge transfer in the Cu_xPd_{1-x} alloy system. *Phys. Rev. B*, 56(19):12178–12181, 1997.
- [205] D. Raiser and J. P. Deville. Study of XPS photoemission of some gadolinium compounds. *J. Electron Spectrosc. Relat. Phenom.*, 57:91–97, 1991.
- [206] J. Lachnitt, H. Ufer, and I. Karla. Photoemission investigations of GdCu. *Surface Science*, 377-379:238–241, 1997.
- [207] J. Szade, I. Karla, D. Gravel, and M. Neumann. Photoemission investigation of Gd-Cu compounds. *J. All. Comp.*, 1999. in print.
- [208] D. A. Shirley. The effect of atomic and extra-atomic relaxation on atomic binding energies. *Chem. Phys. Lett.*, 16(2):220–225, 1972.

- [209] C. K. Jørgensen. Photoelectron spectra showing relaxation effects in the continuum and electrostatic and chemical influences of the surrounding atoms,. In Löwdin, editor, *Advances in Quantum Chemistry*, volume 8, pages 137–186. Academic Press, New York, 1974.
- [210] M. Campagna, E. Bucher, D. N. E. Buchanan G. K. Wertheim, and L. D. Longinotti. *Proc. 11th Rare Earth Res. Conf., Traverse City, Mich., US AECTIC, Oak Ridge, Tenn., 1974.*
- [211] M. Campagna, G. K. Wertheim, and Y. Baer. Unfilled inner shells: Rare earths and their compounds. In L. Ley and M. Cardona, editors, *Photoemission in Solids II*, chapter 4, pages 217–260. Springer Verlag, Heidelberg, 1979.
- [212] P. A. Dowben, D. LaGrafte, Dongqi Li, L. Döttl, C. Hwang, Y. Ufuktepe, and M. Onellion. Final state effects in photoemission of the 4f levels of terbium and dysprosium. *J. Phys.: Condens. Matter*, 2:8801–8812, 1990.
- [213] J. K. Lang, Y. Baer, and P. A. Cox. Study of the 4f and valence band density of states in rare-earth metals: II. Experiment and results. *J. Phys. F: Metal Phys.*, 11:21–38, 1981.
- [214] Y. Baer and J. K. Lang. High-energy spectroscopy of f^{n+1} and f^{n-1} states in rare earth metals. *J. Appl. Phys.*, 50(11):7485–7488, 1979.
- [215] J. J. Yeh and I. Lindau. Atomic subshell photoionisation cross sections and asymmetry parameters: $1 \leq z \leq 103$. *Atomic Data and Nuclear Data Tables*, 32(1):1–155, 1985.
- [216] A. Ślebarski, A. Jezierski, A. Zygmunt, S. Mähl, and M. Neumann. Band gap stability in CeRhSb. *Phys. Rev. B*, 58(20):13498–13505, 1998.
- [217] A. Ślebarski, A. Jezierski, S. Mähl, M. Neumann, and G. Borstel. Electronic structure of $\text{CeNi}_{1-x}\text{Pd}_x\text{Sn}$ and LaMSn ($M=\text{Ni,Cu,Pd}$). *Phys. Rev. B*, 56(12):7245–7254, 1997.
- [218] D. A. Papaconstantopoulos. *Handbook of the band structure of elemental solids*. Plenum Press, New York, 1986.
- [219] Yu. M. Yarmoshenko and E. Z. Kurmaev. private communication, 1998.

- [220] B. T. Thole, X. D. Wang, B. N. Harmon, Dongqi Li, and P. A. Dowben. Multiplet fine structure in the photoemission of the gadolinium and terbium 5p levels. *Phys. Rev. B*, 47(14):9098–9101, 1993.
- [221] F. H. Mies. Configuration interaction theory. Effects of overlapping resonances. *Phys. Rev.*, 175(1):164–175, 1968.
- [222] S. R. Mishra, T. R. Cummins, G. D. Waddill, W. J. Gammon, G. van der Laan, K. W. Goodman, and J. G. Tobin. Nature of resonant photoemission in Gd. *Phys. Rev. Lett*, 81(6):1306–1309, 1998.
- [223] J. Igarashi and T. Nakano. A theory of resonant photoemission in copper halides. *J. Phys. Soc. Jpn.*, 55(4):1384–1391, 1986.
- [224] Z. X. Shen, R. S. List, D. S. Dessau, F. Parmigiani, A. J. Arko, R. Bartlett, B. O. Wells, I. Lindau, and W. E. Spicer. Photoemission study of CuO and Cu₂O single crystals. *Phys. Rev. B*, 42(13):8081–8085, 1990.
- [225] S. Shin, S. Suga, M. Taniguchi, M. Fujisawa, H. Kanzaki, A. Fujimori, H. Daimon, Y. Ueda, K. Kosuge, and S. Kachi. Vacuum-ultraviolet reflectance and photoemission study of the metal-insulator phase transitions in VO₂, V₆O₁₃, and V₂O₃. *Phys. Rev. B*, 41(8):4993–5009, 1990.
- [226] A. Wall, A. Franciosi, D. W. Niles, R. Reifenberger, C. Quaresima, M. Capozzi, and P. Perfetti. Electronic structure of Cd_{1-x}Mn_xS ternary semimagnetic alloys. *Phys. Rev. B*, 41(9):5969–5978, 1990.
- [227] Ya. O. Dovgyi and I. V. Kityk. Antiresonances in the fundamental spectra of CdI₂-4H and CdBr₂-6R crystals. *Phys. Stat. Sol. B*, 157(1):473–479, 1990.
- [228] P. Weibel, M. Grioni, D. Malterre, O. Manzardo, Y. Baer, and G. L. Olcese. Resonance and anti-resonance in inverse photoemission: discriminating localized and extended states in cerium systems. *Europhys. Lett.*, 29(8):629–34, 1995.
- [229] W. T. Carnall, P. R. Fields, and K. Rajnak. Electronic energy levels in the trivalent lanthanide aquo ions. I. Pr³⁺, Nd³⁺, Pm³⁺, Sm³⁺, Dy³⁺, Ho³⁺, Er³⁺ and Tm³⁺. *J. Chem. Phys.*, 49(10):4424–4442, 1968.
- [230] H. M. Crosswhite, R. L. Schwiesow, and W. T. Carnall. Energy-level structure of Gd³⁺ in CaF₂. *J. Chem. Phys.*, 50(11):5032–5033, 1969.

- [231] G. van der Laan. private communication, 12.2.1999.
- [232] G. van der Laan and B. T. Thole. Spin polarization and magnetic dichroism in photoemission from core and valence band states in localized magnetic systems. II. Emission from open shells. *Phys. Rev. B*, 48(1):210–213, 1993.
- [233] E. Vescovo, O. Rader, G. van der Laan, and C. Carbone. Spin-polarized photoemission from shallow core levels in localized materials. *Phys. Rev. B Rapid Comm.*, 56(18):R11403–R11406, 1997.
- [234] F. Patthey, W. D. Schneider, Y. Baer, and B. Dely. High temperature collapse of the Kondo resonance in CeSi_2 observed by photoemission. *Phys. Rev. Lett*, 58(26):2810–2813, 1987.
- [235] M. Donath, P. A. Dowben, and W. Nolting. *Magnetism and electronic correlations in local-moment systems: Rare-earth elements and compounds*. World Scientific, Singapore, 1998.
- [236] V. N. Antonov, P. A. Oppeneer, A. N. Yaresko A. Ya. Perlov, and T. Kraft. Computationally based explanation of the peculiar magneto-optical properties of PtMnSb and related ternary compounds. *Phys. Rev. B*, 56(20):13012–13025, 1997.

Chapitre 1

Introduction

Les terres rares et leurs composés sont de haut intérêt technique et plusieurs nouveaux domaines d'applications arrivent car ils ont une large gamme de propriétés physiques et chimiques. En prenant avantage des caractéristiques de tous les éléments et en considérant les interactions entre eux, on peut souvent créer un composé de terre rare qui a exactement les propriétés désirées, qui sont adaptées spécialement pour l'application prévue ou pour mieux remplacer d'autres matériaux existants.

Ce comportement vient principalement de la couche 4f des éléments terres rares, qui est partiellement remplie. Cette couche est située près du noyau atomique avec des moments fortement localisés. En même temps, leurs états d'énergie sont situés dans la bande de valence (élargie); ils se trouvent proches du niveau du Fermi pour les terres rares légères et quelques eV au dessous pour les terres rares lourdes. Tandis que le multiplet d'état fondamental de la couche 4f peut être décrit en général complètement par la mécanique quantique et le couplage Russell-Saunders, la situation est très complexe pour les configurations excitées, à cause des corrélations fortes des électrons 4f. Par conséquent, une grande partie de la description théorique des spectres optiques n'est pas encore comprise complètement, particulièrement quand il y a des processus à N-corps. Donc, il reste encore beaucoup de travail pour analyser le comportement des atomes de terre rare en interaction avec les autres atomes du système.

La thèse présentée est consacrée à la caractérisation de quelques composés de terres rares pour mieux comprendre les effets qui contrôlent le comportement physique dans les composés fortement corrélés et l'interaction entre plusieurs échelles d'énergie. Particulièrement, un centre d'intérêt est la série des $RNiSb$ (R = différentes terres rares) parce qu'ils combinent les propriétés causées par l'élément de terre rare avec la structure électronique à bandes

étroites dans ces composés hexagonaux ou demi-Heusler. Ceci aboutit à des propriétés qui varient fortement, particulièrement entre ces composés avec des éléments de terre rare légers et lourds. Elles varient par exemple de paramagnétiques ou ferromagnétiques à des structures antiferromagnétiques. Les composés avec une terre rare légère sont métalliques, tandis que ceux avec une terre rare lourde sont des semiconducteurs magnétiques où nous avons découvert une magnétorésistance géante.

Pour exécuter ces études, le groupe de composés a été étudié de différents points de vue en utilisant un grand nombre de méthodes de caractérisation, à savoir mesures magnétiques, de transport, de diffusion neutronique et de photoémission. Comme on va le montrer dans le corps de la thèse, ces techniques sont complémentaires dans le sens que chacune donne des informations sur des niveaux d'énergie dans leur propre gamme et les résultats d'une technique sont souvent nécessaires pour analyser les données obtenues par une autre méthode.

Par exemple, les moments magnétiques de la couche 4f diffusent les électrons de conduction. Donc, ils influencent la résistivité électrique et la magnétorésistance. Ces mécanismes de transport dépendent des états électroniques autour de niveau du Fermi; particulièrement, le couplage des spins des électrons 4f entre eux et avec l'environnement explique les moments magnétiques. Le champ cristallin électrique (CEF) est déterminé par les liaisons avec le réseau. Il influe sur beaucoup de propriétés observées macroscopiquement (aimantation de l'état fondamental, magnétorésistance) qui sont contrôlées par la population, la structure et symétrie des niveaux CEF.

Une partie importante de ce travail concerne l'utilisation de modèles théoriques, qui forment une indispensable contribution pour interpréter les données expérimentales. Pour chaque technique utilisée, les spectres ont été soit simulés ou les données expérimentales ont été comparées et déconvoluées avec les valeurs obtenues théoriquement. La description théorique a permis de calculer des propriétés macroscopiques, mesurées directement. Par exemple, la nature de la résistivité et le mécanisme de magnétorésistance ont pu être identifiés par la modélisation des différents processus de conduction, basée sur des calculs de la structure électronique. Ces calculs ont été aussi nécessaires pour analyser les spectres de photoémission et les spectres de résonance. Des simulations des spectres de diffraction élastique et diffusion inélastique des neutrons ont permis de déterminer la structure magnétique et les niveaux du champ cristallin. En retour, ceux-ci ont permis de calculer la résistivité et la susceptibilité magnétique.

La structure générale de la thèse est la suivante: Après cette introduc-

tion, le chapitre (2) présente le groupe étudié des composés de terres rares, et leurs structures cristallines déterminées par diffraction des rayons-X. Après, les diverses propriétés magnétiques sont étudiées avec l'aide de l'aimantation, la susceptibilité et de mesures de diffraction élastique des neutrons (chapitre 3). Le chapitre suivant (4) est consacré aux propriétés de transport électrique ainsi que leur modification sous un champ magnétique. Il est suivi par l'analyse du champ cristallin déterminé par diffusion inélastique des neutrons (chapitre 5). Puis, la structure électronique est examinée dans le chapitre (6). Le centre d'intérêt est mis sur les états dans la bande de valence qui est responsable de beaucoup de propriétés. Ils sont déterminés par une analyse par spectroscopie des photoélectrons et par des techniques de résonance. Le chapitre final contient les conclusions de l'étude et des directions possibles pour un travail futur. Au début de chaque chapitre, des informations théoriques sont présentées brièvement.

Chapitre 7

Conclusion et perspectives

Dans cette thèse, des composés de terre rare, particulièrement la série des RNiSb (R= terre rare) ont été étudiés de plusieurs points de vue pour révéler les différentes échelles d'énergie impliquées dans leurs propriétés physiques.

La structure électronique des couches atomiques a été étudiée par la spectroscopie des photoélectrons. En raison des corrélations entre la couche 4f incomplète et le trou créé dans les couches internes, nous avons observé un éclatement des spectres de multiplets, d'environ 30 eV pour les états 4d et de 8 eV pour les multiplets 4f. Les caractéristiques de la bande de valence ont été interprétées avec l'aide des calculs de la densité partielle d'états, qui permettent de séparer les contributions des états R 4f 5d 6s, Ni 3d et Sb 5s 5p. La position de l'énergie des pics 4f a un petit décalage chimique autour de 0.2 eV vers une énergie de plus forte liaison, comparée avec la position des terres rares pures, à cause de la liaison avec Sb. Par les variations de la forme des profils de la résonance-Fano, obtenus sur les pics $^8S_{7/2}$, (6I , 6P , 6D) et (6G , 6F , 6H) de Tb, on a pu résoudre et identifier qualitativement des canaux différents d'excitation et de deexcitation reliés aux états 4f inoccupés au dessus de niveau de Fermi qui sont séparés par environ un eV.

Les calculs de densité d'états ont révélé un gap d'énergie autour de 200 meV dans les composés semiconducteurs des terres rares lourdes. Cependant, les mesures de la résistivité entre 200 et 300 K ont donné un gap de 20 à 80 meV relié aux niveaux donneurs/accepteurs dans le gap. Des mesures du pouvoir thermo-électrique négatif ont montré, que à température ambiante, les porteurs principaux sont des électrons dans les échantillons étudiés. Par des simulations théoriques nous avons montré que le processus de conduction est contrôlé par l'activation de ces états donneurs/accepteurs dans le gap intrinsèque. A basse T, ρ est gouvernée par les sauts à distance variable ou par conduction dans une bande d'impuretés selon la densité de défauts.

Dans ces semiconducteurs magnétiques, une résistance magnétique géante a été découverte, atteignant -50% sous des champs magnétiques de 8 Tesla. Le mécanisme a été identifié comme la diffusion par le désordre de spin et a été décrit avec succès par la polarisation des états d'impuretés par la couche 4f.

La série des composés RNiSb montre une large gamme de propriétés paramagnétiques (Y,La,Pr,Lu), ferromagnétiques (Nd), antiferro (Tb,Dy,Ho,Er). Le couplage magnétique atteint 2 meV. Dans les composés de terres rares légères RNiSb, le couplage magnétique se constitue indirectement par le mécanisme RKKY, où un petit vecteur k_F au niveau de Fermi favorise l'ordre ferromagnétique ou modulé qui est observé. Par contre, les composés de terres rares lourdes RNiSb ont un ordre antiferromagnétique avec un vecteur de propagation $\vec{Q} = (\frac{1}{2}, \frac{1}{2}, \frac{1}{2})$ contrôlé par les interactions de superéchange, qui sont probablement à courte distance, dominées par les interactions entre les atomes voisins les plus proches.

La spectroscopie neutronique a permis d'étudier l'état fondamental de ces systèmes, venant de la séparation du multiplet LSJ d'état fondamental par le champ électrique cristallin (CEF) dans la gamme d'énergie de 0.1 eV à 10 meV. Des calculs sur la base de l'arrangement des niveaux de champ cristallin électrique (CEF) ont donné une explication de la direction et la rotation observées des moments magnétiques entre les axes d'ordre 2 et 4 du réseau (Tb,Ho) et l'absence de l'ordre magnétique dans certaines configurations (Pr). En plus, la simulation de la résistivité magnétique, en utilisant une théorie de Cornut-Coqblin incorporant le champ cristallin, a prouvé l'existence de l'effet Kondo dans CeNiSb. Finalement, l'échelle d'énergie la plus petite observée, est le couplage Kondo dans CeNiSb qui est environ 0.5 meV d'après les mesures de diffusion inélastique des neutrons.

Les perspectives de recherches pourraient être les suivantes: Puisque des composés proches (p.e. CeSb, NiMnSb, PtMnSb) montrent un grand effet Kerr magnéto-optique, il serait intéressant d'étudier ce comportement aussi dans les composés RNiSb. L'effet Hall et le pouvoir thermoélectrique donneraient le signe des porteurs de charge et des mesures de la chaleur spécifique pourraient apporter la densité d'états $n(E_F)$ au niveau de Fermi. L'approche présentée pour identifier le mécanisme de conduction et la nature des défauts n'est pas limitée au système présent. Elle pourrait aussi être utilisée comme méthode de caractérisation pour des composés similaires et pour les semiconducteurs magnétique de faible gap. Des mesures de la photoémission résonante résolue en spin pourraient apporter des informations supplémentaires nécessaires, qui aideraient à décrire plus précisément les canaux de résonance dans ces composés corrélés. Au cas où des mono-

cristaux de ces composés deviendraient disponibles, il sera très intéressant d'étudier les effets d'anisotropie et d'exécuter des mesures de photoémission résolues en angle pour déterminer la structure de bandes.

1. The first part of the document is a list of the names of the members of the committee who have been appointed to the various sub-committees. The names are listed in alphabetical order of the last name.

Abstract

The properties of RNiSb compounds were studied from various points of view: Magnetism, transport, electronic structure. The compounds with a light rare earth are metallic, while the cubic phases with a heavy rare earth element have the semi-Heusler structure and are narrow gap semiconductors. A giant magnetoresistance effect was found at low temperatures, the larger as the density of charge carriers is weak. It was explained by the polarisation of the impurity levels situated within the band gap of the semiconductor under the field of the magnetic moment of the 4f shell.

The crystal field, as well as the magnetic order at low temperatures, were studied by neutron scattering and diffraction. Particular magnetic properties (absence of magnetic order in the Pr compound, antiferromagnetic structure in the second group, orientation of the moments) have been explained, at least qualitatively. CeNiSb is a Kondo-type compound with a Kondo temperature of about 8 K.

Photoemission measurements have allowed to analyse the electronic structure in the valence band of these compounds, in agreement with band structure calculations. By resonant photoemission of TbNiSb and GdCu, different resonance channels have been resolved, which depend on the spin configuration of the excited states.

Résumé

Les propriétés des composés RNiSb sont étudiées sous plusieurs aspects: magnétisme, transport, structure électronique. Les composés hexagonaux avec une terre rare légère sont métalliques, les phases cubiques du type semi-Heusler avec les terres rares lourdes sont des semiconducteurs à faible gap. Des phénomènes de magnétorésistance géante sont observés à basse température, d'autant plus importants que la densité de porteurs est plus faible. Ils sont expliqués par la polarisation par le moment de la couche 4f des niveaux d'impuretés situés dans le gap du semiconducteur.

Le champ cristallin, ainsi que l'ordre magnétique à basse température, ont été étudiés par diffusion (diffraction) de neutrons. Certaines propriétés magnétiques (absence d'ordre magnétique avec le Pr, structures AF dans le second groupe, orientation des moments) ont pu être expliquées au moins qualitativement. CeNiSb est un composé de type Kondo avec une température de Kondo de l'ordre de 8 K.

Des mesures de photoémission ont permis de préciser la structure des bandes de valence de ces composés, en accord avec des calculs de structure électronique. Par photoémission résonante dans TbNiSb et GdCu, différents canaux de résonance ont été résolus en fonction de l'énergie, qui dépendent de la structure des multiplets et de la configuration des niveaux excités.

